

ELECTRORHEOLOGY FOR ENERGY PRODUCTION AND CONSERVATION

A Dissertation
Submitted
to the Temple University Graduate Board

In Partial Fulfillment
of the Requirements for the Degree of
Doctor of Philosophy

By
Ke Huang
January, 2010

ABSTRACT

ELECTRORHEOLOGY AND MAGNETORHEOLOGY FOR ENERGY PRODUCTION AND CONSERVATION

Ke Huang

Doctor of Philosophy

Temple University, 2009

Doctoral Advisory Committee Chair: Dr. Rongjia Tao

Recently, based on the physics of viscosity, we developed a new technology, which utilizes electric or magnetic fields to change the rheology of complex fluids to reduce the viscosity, while keeping the temperature unchanged. The method is universal and applicable to all complex fluids with suspended particles of nano-meter, sub-micrometer, or micrometer size. Completely different from the traditional viscosity reduction method, raising the temperature, this technology is energy-efficient, as it only requires small amount of energy to aggregate the suspended particles.

In this thesis, we will first discuss this new technology in detail, both in theory and practice. Then, we will report applications of our technology to energy science research.

Presently, 80% of all energy sources are liquid fuels. The viscosity of liquid fuels plays an important role in energy production and energy conservation. With an electric

field, we can reduce the viscosity of asphalt-based crude oil. This is important and useful for heavy crude oil and off-shore crude oil production and transportation. Especially, since there is no practical way to raise the temperature of crude oil inside the deepwater pipelines, our technology may play a key role in future off-shore crude oil production.

Electroreology can also be used to reduce the viscosity of refinery fuels, such as diesel fuel and gasoline. When we apply this technology to fuel injection, the fuel droplets in the fuel atomization become smaller, leading to faster combustion in the engine chambers. As the fuel efficiency of internal combustion engines depends on the combustion speed and timing, the fast combustion produces much higher fuel efficiency. Therefore, adding our technology on existing engines improves the engine efficiency significantly. A theoretical model for the engine combustion, which explains how fast combustion improves the engine efficiency, is also presented in the thesis.

As energy is the key to our national security, we believe that our technology is important and will have a strong impact on energy production and conversation in the future.

ACKNOWLEDGMENTS

This thesis would not have been possible without the support of many people. I would like to take this opportunity to show my gratitude to those who made this work possible.

First of all, I would like to express my deepest appreciate to my supervisor, Dr. Rongjia Tao, who has consistently supported me throughout my entire research work in the Physics Department and offered me guidance on my thesis with his patience and knowledge, while giving me enough space to develop myself. He is a brilliant physicist from whom I can always get inspiration and knowledge, as well as a friend on whom I can count to overcome difficulties.

I would like to thank my committee members, Dr. Theodore W. Burkhardt, Dr. Zameer Hasan, and Dr. Seong G. Kong, for their advice and kind support of my study and research work during my years in Temple University, as well as their efforts in reviewing the thesis for me.

I also thank Dr. Lin, Dr. Yuen, Dr. Riseborough, Dr. Kheli, Dr. Intemann, and all other professors in the department who have taught me and provided me with their cherishable advice.

It was an unforgettable experience working with Dr. Xu and Dr. Tang in our group, from whom I learned a lot of priceless experimental knowledge. I would also like to thank Deepika, Enpeng, and other coworkers in our group. It was great pleasure working with them.

Thanks to all of the people in the physics department, especially, Ed, Richard, and Andrew for their technical support, as well as Evelyn and Janis for their help in administrative related issues.

This work was partially supported by RAND and STWA. Thanks to Douglas Bell for his special support and for doing experiments with us and installing our experimental device on his car.

Thanks to my friends Xiaodong, Jianmei, Huan, Zhengle and Yafei for their supports in my study, research, and daily life.

Finally, I would also thank my parents and my fiancée Rui, without whose supports, this work would never have been accomplished.

TABLE OF CONTENTS

	PAGE
ABSTRACT.....	iii
ACKNOWLEDGMENTS	v
TABLE OF CONTENTS.....	vii
LIST OF TABLES.....	xii
LIST OF FIGURES	xiv
1. INTRODUCTION	1
1.1 Viscosity Reduction for Energy Production, Transportation, and Conservation.....	1
1.2 Transport Off-Shore Crude Oil Via Deepwater Pipelines	2
1.3 New Fuel Injection Technology.....	4
1.4 Organization of this Thesis	6
2. PHYSICAL MECHANISM FOR REDUCING VISCOSITY OF LIQUID SUSPENSIONS WITH EM FIELDS.....	7
2.1 Viscosity	7
2.1.1 Dynamic Viscosity.....	7
2.1.2 Kinematic Viscosity.....	9
2.2 Newtonian and Non-Newtonian Fluids	10
2.3 Viscosity and Volume Fraction of Liquid Suspension	12
2.4 Viscosity and Particle Size Distribution	16

2.5	Polarization of Particles in External Field	27
2.5.1	Polarization of Dielectrics in Electric Field.....	27
2.5.2	Dipole Moment of Dielectric Spheres in Electric Field	29
2.5.3	Electric Dipole Field, Dipolar Interaction and Forces between Dipoles	35
2.5.4	Magnetic Dipole, the Field, Interaction and Forces between Dipoles	37
2.6	Brownian Motion, Langevin's Theory and Diffusion Coefficient	39
2.6.1	Brownian Motion	39
2.6.2	Langevin's Theory	39
2.6.3	Diffusion Coefficient	40
2.7	Reducing the Viscosity of Liquid Suspension by Electric or Magnetic Field.....	43
2.7.1	Reducing the Viscosity by Electric Field.....	43
2.7.2	Critical Electric Field.....	44
2.7.3	Minimal Field Pulse Duration.....	45
2.7.4	Critical Field and Minimal Pulse Duration in the Presence of Magnetic Field.....	46
2.7.5	Field Application Duration, Direction and System Relaxation Time	46
2.8	Experimental Verification and Applications with MR Fluid.....	49
3.	EQUIPMENT AND DEVICES USED IN FIELD TREATMENT AND DIESEL AUTOMIZATION AND SPRAY EXPERIMENT	53
3.1	Electric Magnet and Power Supply.....	53
3.2	High Voltage Power Supply	55
3.3	Rotational Viscometers.....	56
3.3.1	Brookfield Rotational Viscometer	56

3.3.2	Brookfield HA/HB and LV Spindle Sets.....	58
3.3.3	Spindle Range Coefficient.....	60
3.4	Capillary Viscometers.....	62
3.5	Devices Used in Electric Field Treatment.....	65
3.5.1	Solid Plate Capacitor Sample Treatment Container.....	65
3.5.2	Mesh Capacitor Sample Treatment Container and Tube.....	67
3.6	Devices Used in Fuel Treatment, Atomization, and Spray Experiments.....	70
3.6.1	Field Application Device.....	70
3.6.2	Pressurized Fuel Container and Fuel Injector.....	71
3.7	Other Devices.....	73
4.	REDUCING THE VISCOSITY OF CRUDE OIL.....	77
4.1	Crude Oils.....	77
4.1.1	Composition of Crude Oils.....	77
4.1.2	API Gravity of Crude Oils.....	79
4.2	Experimental Methods and Setup.....	80
4.2.1	Experimental Methods.....	80
4.2.2	Experimental Setup.....	80
4.3	Crude Oils from JGC.....	84
4.3.1	Temperature Effects of JGC Crude Oils.....	86
4.3.2	Repeatability of Measurement.....	86
4.3.3	Reducing Viscosity of JGC Crude Oils by Electric Field.....	88
4.3.4	Reducing Viscosity of JGC Crude Oils by Magnetic Field.....	94

4.4	Crude Oils from Shell	96
4.4.1	Temperature Effects of Shell Crude Oils.....	97
4.4.2	Reducing Viscosity of Maya Crude Oil by Electric Field.....	97
4.4.3	Reducing Viscosity of Maya Crude Oil by Magnetic Field	102
4.5	Electric Field Treatment Device and Cost Estimate for Commercial Pipeline.....	103
5.	VISCOSITY REDUCTION OF FUELS FOR IMPROVED COMBUSTION EFFICIENCY	105
5.1	Viscosity Reduction and Droplet Formation	105
5.1.1	Viscosity Reduction Leads to Finer Droplets in Spray	105
5.1.2	Fuel Efficiencies in Fast and Slow Combustion Processes.....	107
5.1.3	Viscosity Reduction Increases Fuel Efficiency	114
5.2	Diesel, Gasoline and Ethanol Fuels	117
5.3	Reducing Viscosities of Fuels.....	117
5.3.1	Temperature Effect on Fuels.....	117
5.3.2	Reducing Viscosity of Fuels by Magnetic Field.....	117
5.3.3	Reducing Viscosity of Fuels by Electric Field	122
5.4	Flow Experiments with Diesel.....	127
5.4.1	Experiment Setup in Flow Experiments	127
5.4.2	Varying Field Strength with Constant Duration Time	129
5.4.3	Varying Duration Time with Constant Field Strength.....	130
5.5	Spray Experiment and Results	132
5.5.1	Method and Experimental Setup.....	132

5.5.2	Image Processing and Data Analysis.....	134
5.5.3	Experimental Results for Diesel, E20 and E85.....	136
5.6	Improving Fuel Efficiency by Electric Field Treatment.....	140
5.6.1	Engine Test at Cornaglia Iveco.....	140
5.6.2	Engine Test on Mercedes-Benz 300D	143
5.7	Conclusion	146
	REFERENCES CITED.....	147

LIST OF TABLES

Table	Page
2.1. First Three Legendre Polynomials	32
3.1. Main Specifications for DV-III and DV-II+ Pro	57
3.2. Spring Sets with Different Torques Provided by Brookfield	57
3.3. Spindle Range Coefficient (<i>SRC</i>) for Different Brookfield Spring Sets and Spindle Models	61
3.4. Kinematic Viscosity Range of Cannon Capillary Viscometers	64
4.1. Composition of Elements in Crude Oil by Weight Percentage	78
4.2. Weight Percentage of Four Types of Hydrocarbon Molecules in Crude Oil	78
4.3. Viscosities of JGC Crude Oils with API Gravity of 11 °, 15 ° and 21 ° at 21 °C	84
4.4. Viscosity Reduction Results for JGC API 11 ° Crude Oil by Electric Field	93
4.5. Viscosity Reduction Results for JGC API 21 ° Crude Oil by Electric Field	93
4.6. Viscosity Reduction Results for JGC API 15 ° Crude Oil by Electric Field	94
4.7. Viscosity Reduction Results for JGC Crude Oils by Magnetic Field Treatment	95
4.8. Viscosity Reduction of Shell Maya Crude Oil by Electric Field	99
4.9. Viscosity Reduction of Shell Maya Crude Oil by Magnetic Field	102

5.1. Flow Experiments for Diesel Fuel with Different Field Strength and Constant Application Time 4 s	129
5.2. Flow Experiments for Diesel Fuel with Different Duration Time and Constant Field Strength at 1000 V/mm.....	130
5.3. Diesel Engine Test Results with and without Field Treatment	142
5.4. Diesel Engine Test Results with Different Field Direction.....	142

LIST OF FIGURES

Figure	Page
2.1. Illustration of Viscosity with Fluid between Two Parallel Plates	8
2.2. Newtonian Fluid and Non-Newtonian Fluid (Pseudoplastic)	11
2.3. Dependence of Viscosity on Particle Size at Same Volume Percentage (Small Particle Diameters)	20
2.4. Dependence of Viscosity on Particle Size at Same Volume Percentage (Slightly Larger Particle Diameters)	21
2.5. Dependence of Viscosity on Particle Size at Same Volume Percentage (Much Larger Particle Diameters).....	22
2.6. Dependence of Viscosity on Particle Distribution at Same Volume Percentage (Submicron Particles).....	24
2.7. Dependence of Viscosity on Particle Distribution at Same Volume Percentage (Micron Particles)	25
2.8. Polarization of Dielectric Atom in Electric Field.....	28
2.9. Polarization of Dielectric Slab and Sphere.....	28
2.10. Polarization of Dielectric Particle in Liquid Base.....	29
2.11. Relationship among Unit Vectors \hat{r} , $\hat{\theta}$, and \hat{z}	36
2.12. Magnetic Pulse Field Reduces Viscosity of MR Fluid	50
2.13. Viscosity Drop of MR Fluid Depends on Field Duration	50
2.14. Average Size of Particle Clusters vs. Magnetic Field Duration.....	51
2.15. Picture of Aggregated Particle Cluster	52
3.1. Magnion Power Supply and Magnet	53

3.2. Magnetic Field Strength vs. Power Supply Current	54
3.3. High Voltage Power Supplies and DC Power Input	55
3.4. Rotational Viscometers	56
3.5. Spindles Used in Viscosity Measurements I	58
3.6. Spindles Used in Viscosity Measurements II	59
3.7. Capillary Viscometer	62
3.8. Solid Plate Capacitor Sample Treatment Container I	65
3.9. Solid Plate Capacitor Sample Treatment Container II	66
3.10. Mesh Capacitor Sample Treatment Container	68
3.11. Mesh Capacitor Sample Treatment Tube	68
3.12. Field Treatment Device and the Schematic	70
3.13. Pressurized Fuel Container and the Schematic	71
3.14. Fuel Injector and the Adapter	72
3.15. Glass Tubes and Needles	73
3.16. Micro Balance	74
3.17. Experimental Stand with Capillary Viscometer	74
3.18. Container with Water Jacket	75
4.1. Schematic of Setup for Static Field Treatment	81
4.2. Schematic of Setup for Continuous Field Treatment	83
4.3. JGC Crude Oil Samples	85
4.4. Reproducibility of Measurement	87
4.5. Viscosity Reduction after Field Treatment	88
4.6. Viscosity Drop vs. Field Duration	89

4.7. Viscosity Drop vs. Field Strength	91
4.8. System Relaxation after Field Treatment	92
4.9. Shell Crude Oils from Maya and Quo Iboe.....	96
4.10. Temperature Effect of Maya Crude Oil.....	98
4.11. Temperature Effect of Qua Iboe Crude Oil.....	98
4.12. Dripping Flow Device Used in Continuous Field Treatment for Maya Crude Oil	100
4.13. Design of Electric Field Treatment Device on Oil Transportation Pipelines	103
4.14. Design of Connections for Electric Field Treatment Devices to Oil Transportation Pipelines.....	104
5.1. Four-stroke Engine Cycles of an Internal Combustion Engine.....	107
5.2. Pressure-Volume (P-V) Diagram for Fast and Slow Combustion Process.....	108
5.3. Temperature Effect on Viscosity of Pure Diesel.....	118
5.4. Viscosities of Gasoline with 10% MTBE before and after Magnetic Field Treatment	119
5.5. Viscosities of E20 before and after Magnetic Field Treatment.....	120
5.6. Pure Diesel from Sunoco in Special Container	121
5.7. Viscosities of Pure Diesel before and after Magnetic Field Treatment.....	122
5.8. Viscosities of Pure Diesel before and after Electric Field Treatment	123
5.9. Viscosities of Gas Station Diesel before and after Electric Field Treatment.....	124
5.10. Viscosities of E20 before and after Electric Field Treatment	125
5.11. Viscosities of E85 before and after Electric Field Treatment	126
5.12. Experiment Setup in Diesel Flow Experiment	127
5.13. Home Made Labview Program Used in Diesel Flow Experiment.....	128

5.14. Photograph and Schematic of Spray Experiment Setup.....	133
5.15. Original Scan and Processed Image of Plate in Spray Experiment.....	135
5.16. Particle Distribution before and after Field Treatment in Diesel Spray Experiment	136
5.17. Particle Distribution before and after Field Treatment for E20 Spray Experiment	137
5.18. Special Setup for E85 Spray Experiment	138
5.19. Particle Distribution before and after Field Treatment for E85 Spray Experiment	139
5.20. Test of Field Application Device on Diesel Engine	141
5.21. Field Application Device on Mercedes-Benz 300D.....	144
5.22. Laboratory Test on Mercedes-Benz 300D with Field Application Device	144

CHAPTER 1

INTRODUCTION

1.1 Viscosity Reduction for Energy Production, Transportation, and Conservation

Presently, liquid fuels are the leading energy source. The viscosity of liquid fuels plays an important role in energy production, transportation, and conservation. For example, reducing the viscosity of crude oil is the key to extracting crude oil from oil fields, oil sands, and oil shale. In addition, reducing the viscosity of crude oil can speed up the transportation of crude oil via pipelines. Currently, the dominant method for reducing the viscosity of complex fluids is to raise the temperature. This not only requires a large amount of energy, but also raises concerns of the greenhouse effect.

Recently, based on the basic physics of viscosity, we have developed a new technology, which utilizes electric or magnetic field to change the rheology of complex fluids and reduce the viscosity without changing the temperature unchanged. The method is universal and applicable to all complex fluids with suspended particles of nano-meter, sub-micrometer, or micrometer size. This technology is energy-efficient since it only requires small amount of energy to aggregate the suspended particles.

In this thesis, I will review the theory of this viscosity reduction technology and discuss the applications of the technology to crude oil transportation and fuel injection.

1.2 Transport Off-Shore Crude Oil Via Deepwater Pipelines

Reducing viscosity of crude oil is of great importance to oil industry, in extracting and transporting of crude oil. While heating crude oil is the most common way to reduce its viscosity, it is not applicable to the transportation of offshore crude oil through pipelines deep under water.

Today, more than 90% of the global crude oil production is from crude oils of light and medium grades. The exploitation, transportation and refining of these crude oils on land is relatively easy and inexpensive. However, most of these low-cost oils have been exploited for decades. The main remaining reserves of the crude oil are located in remote environments such as ultra-deep formations or deep sea, as well as places that are partially or completely closed to exploitation by international oil companies. As a result of economic global development, the demand for crude oils keeps increasing even with oil prices at a historically high level.

As a solution, heavy crude oil, extra-heavy oil and bitumen resources that previously were uneconomic to exploit are now needed to meet the global demand for fuels (Atkins, 2009). This is the current situation happening not only in regions that are major heavy oil producers but also in those countries or regions that traditionally are light or medium oil producers, such as California, Canada, Mexico, Venezuela, Brazil, the Middle East, and the North Sea. As more and more heavy grade crude oils from remote environments are extracted, a reliable technology for reducing the viscosity of crude oil becomes increasingly important, since, as viscosity of crude oil goes down, the cost for transportation and production also decreases.

So far heating is the most common method to reduce the viscosity of crude oil in the industry. However, the temperature of crude oil in deepwater pipelines is quite low due to the low water temperature at sea bed (Solberg, 2006), creating serious problems in transportation of crude oil in pipelines. Heating crude oil in deep water, if not impossible, is at least much more difficult than on the ground. Solving the problem requires a new technology that reduces the viscosity of crude oil without heating.

In this thesis, a novel technology which uses magnetorheology and electrorheology to reduce the viscosity of crude oil is described in detail (Tao & Xu, 2005, 2006). We have designed devices that apply the technology and carried out experiment on crude oil.

The application of a suitable pulsed magnetic or electric field to crude oil leads to the viscosity reduction that does not depend on change of the oil temperature. Instead, the pulsed fields cause paraffin particles or asphaltene particles in the crude oil to aggregate into larger ones. Specifically, a pulse pulsed magnetic field is applied to paraffin-base crude oil for the viscosity reduction, whereas for asphalt-base crude oil or mixed-base crude oil, an electric field pulse is used to reduce their viscosity.

As the particles in crude oil become larger, the rheological properties of the crude oil change accordingly, which leads to viscosity reduction. The viscosity reduction is not permanent. It lasts for several hours and after that the viscosity returns to its original value. The process is repeated if the field is applied again. The technology has many important applications. In particular, it provides a solution to deepwater pipeline transportation of crude oil, a crucial issue the oil industry faces now and in the future.

1.3 New Fuel Injection Technology

Reducing the viscosity of engine fuels also leads to better engine efficiency and reduces pollutant emissions.

Some progress has been made with the development of fuel injection technology. However, internal combustion engines are still far from being clean and efficient.

Combustion begins at the interface between the fuel droplet and the air. If burning is incomplete, harmful emissions are released. In addition, if the combustion inside the engine is slow, the engine efficiency is low because the heat released by the slow combustion does not have time to do the work for the engine. By reducing the size of the fuel droplets, the total surface between the fuel droplets and the air, where the burning occurs, increases, leading to a cleaner and more efficient engine. The goal of a research on more efficient and cleaner combustion is to produce much finer mist of fuel for combustion of ultra-dilute mixtures at extremely high pressure (Aoyagi, Osada, Misawa, Goto, & Ishii, 2006; Hiroshi, Makoto, Yuichi, Tetsunori, & Shinji, 2004; Miller & Klippenstein, 2006). Some new technologies along these lines are under development. For instance, Delphi Company is designing a new fuel injector with a high pressure of 100 bar to eject gasoline droplets with diameters of $25 \mu\text{m}$ or less. Although this pressure is not extremely high, the device also known as the Delphi Multec 10 GDi multihole fuel injector, requires substantial changes of the gasoline-fuel lines since current fuel lines in gasoline vehicles can only sustain fuel pressure less than 3 bar. The combustion technology with extreme pressure is still under development.

Another potential technology under study is the electrostatic atomization, which charges the fuel droplets negatively (Kelly, 1999; Kelly & Avva, 1998; Okuda & Kelly, 1996). If charge density on the droplets is high, the droplet size will be small, and no agglomeration will occur because of the repulsion of the negatively charged droplets. The electrostatic atomization technology has not been employed on any fuel system to date, not to mention vehicles. One problem is that the electrostatic atomization technology requires a special fuel injector that is totally different from existing fuel injectors on vehicles. It requires a high voltage applied directly to the nozzle of the injector while the emitter cathode supplies negative charges through the fuel inside to the anode. Such a fuel injector has not been installed on any vehicles yet. There is also concern that such a device may consume too much electric power.

In this thesis, we report on new fuel-injection technology, which utilizes electrorheology to reduce the viscosity of the fuel and improves the atomization. We use a device which is capable of producing a strong electric field to reduce the viscosity of petroleum fuels just before atomization. The viscosity reduction leads to finer fuel droplets, as well as cleaner and more efficient combustion. The device can be easily installed on current engines to improve their efficiency and on future vehicles. Both laboratory and road tests confirm the theory and indicate that such a device improves fuel mileage. We expect the technology will be widely applied to current internal combustion engines and future engines as well.

1.4 Organization of this Thesis

In Chapter 2, a theory of the viscosity reduction technology is discussed in detail. The particle size distribution in the fluid plays an important role. Magnetic and electric fields induce aggregation of the particles in crude oil.

In Chapter 3, some equipment and devices built in our laboratory are illustrated and discussed.

In Chapter 4, our methods for reducing viscosity of crude oils are described in detail, and experimental results for several crude oils are presented and compared.

In Chapter 5, a theory for improving combustion efficiency is presented. Some methods for reducing viscosity of different fuels are described and experimental results are presented and compared.

CHAPTER 2
PHYSICAL MECHANISM FOR REDUCING VISCOSITY OF LIQUID
SUSPENSIONS WITH EM FIELD

2.1 Viscosity

Viscosity is a measure the fluid friction or internal resistance of a fluid that is being deformed by either shear stress or extensional stress.

Depending on the nature of the applied stress and the nature of the fluid, there are coefficients of dynamic viscosity (or absolute viscosity), kinematic viscosity, volume viscosity, shear viscosity, and extensional viscosity (Landau & Lifshitz, 1959). Here our discussion is limited to dynamic viscosity and kinematic viscosity.

2.1.1 Dynamic Viscosity

Dynamic viscosity influences the dynamics of an incompressible Newtonian fluid.

Consider two parallel plates of surface area A , with a liquid in between with a viscosity of η , as shown in Figure 2.1 (left).

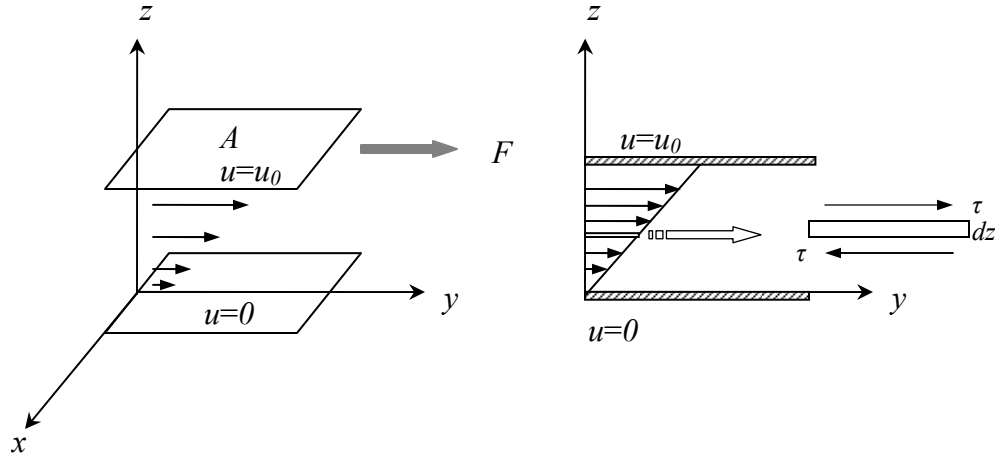


Figure 2.1. Illustration of Viscosity with Fluid between Two Parallel Plates. The top plate moves at speed of u_0 , while the bottom plate is stationary. A cross sectional view of the left schematic is shown on the right.

A tangential force F is exerted on top plate when the plate is moving in the y direction with velocity u_0 . The bottom plate is stationary with velocity 0. Fluid can be treated as many layers, which can slide over each other. Consider the case of no slip between the plate and fluid, so that the fluid layer at the top has the same velocity as the top plate, u_0 , and the fluid layer at the bottom interface has velocity of 0. The intervening layers have intermediate velocities, and there exists a velocity gradient du/dz in the z direction. This is also known as shear rate because

$$u = \frac{dy}{dt},$$

and dy/dz is the shear acting on the sample. Therefore,

$$\frac{du}{dz} = \frac{d}{dt} \left(\frac{dy}{dz} \right) = \dot{\gamma}, \quad (2.1)$$

where $\dot{\gamma}$ is the shear rate.

The shear stress τ is defined as the tangential force F divided by the cross sectional area A of the material where the force is applied A , so that

$$\tau = \frac{F}{A}. \quad (2.2)$$

The dynamic viscosity η is defined as

$$\eta = \frac{F/A}{du/dz} = \frac{\tau}{\dot{\gamma}}. \quad (2.3)$$

The SI unit of dynamic viscosity is the Pascal-second, or $Pa \cdot s$, which equals $kg \cdot m^{-1} \cdot s^{-1}$. The dynamic viscosity is often expressed in the CGS (centimeter-gram-second) unit Poise, or P , which equals $g/cm \cdot s$, or $1/10 Pa \cdot s$. Since P is a quite large unit, the centiPoise, or cP , is used more frequently, where $1 P = 100 cP$. Water at $20.2^\circ C$ has an dynamic viscosity of $1 cP$.

2.1.2 Kinematic Viscosity

In some cases, the ratio of the viscous force to the inertial force is of interest. The viscous force is characterized by the dynamic viscosity η , and the inertial force is characterized by the fluid density ρ . The kinematic viscosity ν is obtained by dividing the absolute viscosity of a fluid by its mass density, so that

$$\nu = \frac{\eta}{\rho}. \quad (2.4)$$

The viscosity ν has a SI unit of Stoke (St), where $1 St = 10^{-4} m^2/s$. Since the Stoke is an unpractically large unit, one often uses the Centistokes (cSt), where $1 St = 100 cSt$.

2.2 Newtonian and Non-Newtonian Fluids

Isaac Newton assumed that the viscosity of fluids is independent of the shear rate. The newtonian fluid is named after him. In the real world most fluids do not exhibit this property. In a non-Newtonian fluid, the viscosity depends on the shear rate.

There are several types of non-Newtonian flow, characterized by the way the viscosity changes in response to variations in shear rate (Brookfield, n.d.). The most common non-Newtonian fluids include (1) pseudoplastics, which display a decreasing viscosity with an increasing shear rate, a famous phenomenon called shear thinning; (2) dilatants, whose viscosity increase with an increasing shear rate; and (3) plastics, which behave as solids under static condition and require sufficient stress before any flow is induced; once flow begins, plastics may display Newtonian, pseudoplastic, or dilatant flow characteristics.

The relationship between shear stress, viscosity and shear strain for typical Newtonian fluid and pseudoplastic Non-Newtonian fluid is shown in 2.2.

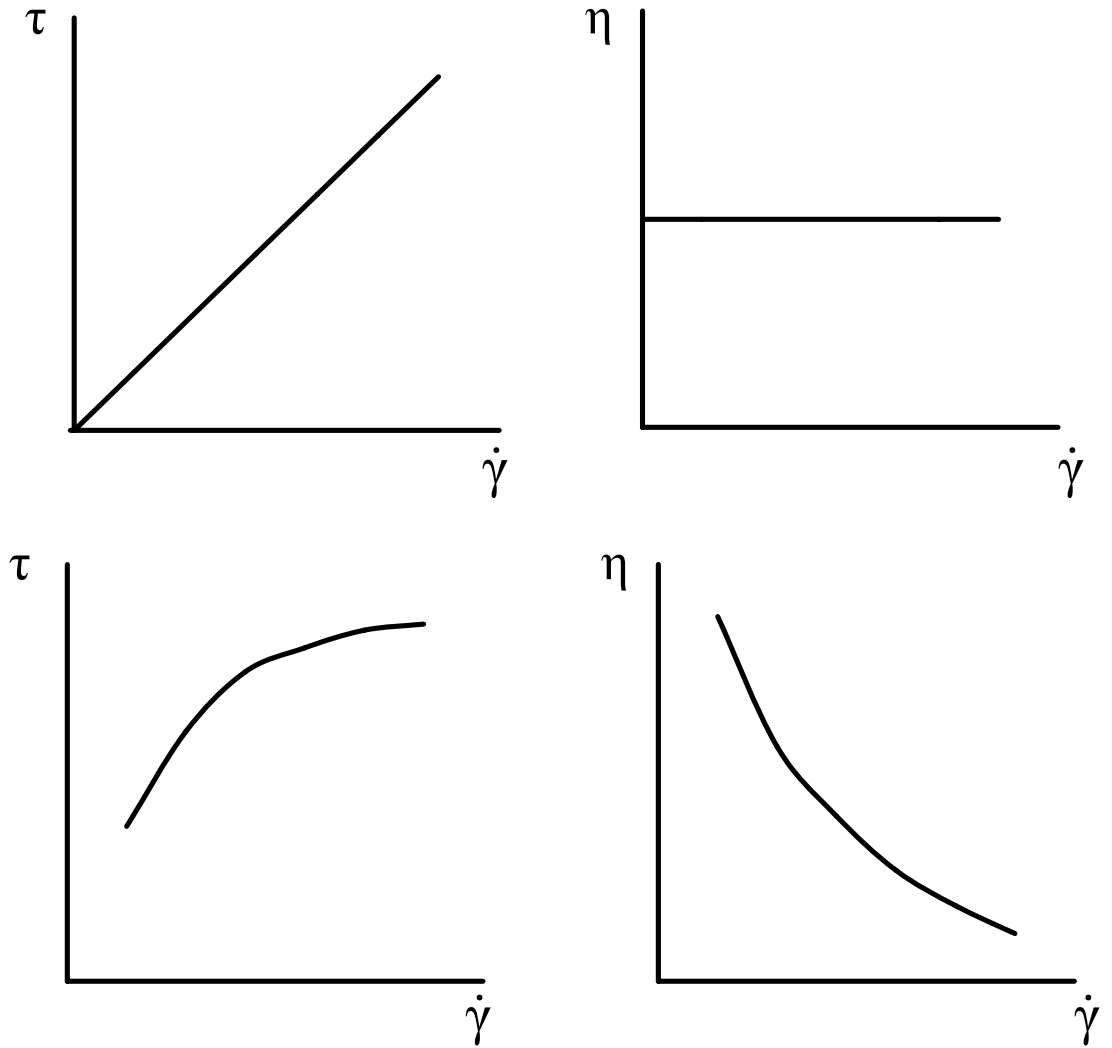


Figure 2.2. Newtonian Fluid and non-Newtonian Fluid (Pseudoplastic). In the upper left graph the shear stress on Newtonian fluid is proportional to the shear strain. In the upper right graph the viscosity remains constant for different shear strain. In the lower left graph the shear stress on non-Newtonian fluid is not proportional to the shear strain. In the lower right graph the viscosity decreases as the shear strain increases, which is a typical phenomenon in a non-Newtonian fluid, known as shear thinning.

2.3 Viscosity and Volume Fraction of Liquid Suspension

Einstein (1905) derived an elegant equation relating the viscosity η of a dilute liquid suspension of noninteracting uniform spheres and the viscosity of its base liquid η_0 . He used this as a model of dilute sugar molecules dissolved in water. Assuming that the sugar molecules are so far apart that the interactions between sugar molecules are negligible, Einstein showed that the apparent viscosity η is given by

$$\eta = \eta_0(1 + 2.5\phi), \quad (2.5)$$

where η_0 is the viscosity of the base liquid and ϕ is the volume fraction of the noninteracting uniform spheres. This is known as Einstein's law of viscosity. It is restricted to very dilute systems with volume fraction $\phi < 0.03$ (Larson, 1999). Many attempts have been made to extend Einstein's equation to higher volume fraction by incorporating a correction term $b\phi^2$ in the equation, where b is a constant coefficient. The corrected equation takes the form

$$\eta = \eta_0(1 + 2.5\phi + b\phi^2). \quad (2.6)$$

Several different models predict $b = 14.1, 12.6$ and 7.35 (Hiemenz, 1986). Now the generally accepted value for b is 6.2 , but Equation 2.6 only works for liquid suspensions with slightly higher volume fraction (Hunter, 1993). At still higher volume fractions, η increases even more rapidly than predicted by Equation 2.6, and a new approach has to be developed.

For higher volume fraction, an approach introduced by Mooney (1951) and developed by Krieger and Dougherty (1959) works very well. Suppose small spheres are

added to the solvent in small groups with each group assigned an index i . Assume that only one group which contains a small amount of spheres, is added to the suspension and before the addition of the extra spheres the suspension is a homogeneous viscous medium so that Equation 2.5 holds. Therefore, the change in the viscosity $d\eta$ is caused by an increase in the volume fraction $d\phi_i$ to a suspension of viscosity $\eta(\phi_i)$ and takes the form

$$d\eta = 2.5\eta(\phi_i)d\phi_i. \quad (2.7)$$

Here $\eta(\phi_i)$ is the viscosity of the suspension prior to the addition of the last fraction.

Adding the same number of spheres to suspensions of different volume fraction clearly has a different impact on the viscosity. The change in the viscosity of a dilute suspension caused by the increase in volume fraction $d\phi$ is much smaller than that of a more concentrated suspension. For a very dilute suspension, adding a small amount of spheres barely changes its viscosity. If the same number of spheres is added to a highly concentrated suspension, the change of the viscosity would be enormous. This is easily seen in the extreme case that a suspension is one group away from the close-packed condition. On adding the very last group of spheres to the suspension, the volume fraction ϕ reaches its maximum value ϕ_m , and the suspension becomes rigid, so that its viscosity goes to infinity.

Thus, the maximum volume fraction ϕ_m must be taken into account. When we add the volume fraction $d\phi$ of spheres to a liquid suspension of volume fraction ϕ , the net available volume fraction is $1 - \phi/\phi_m$. The $d\phi_i$ in Equation 2.7 can be written as

$$d\phi_i = d\phi / (1 - \phi / \phi_m). \quad (2.8)$$

Equation 2.8 becomes

$$d\eta = 2.5\eta d\phi / (1 - \phi / \phi_m), \quad (2.9)$$

or

$$d\eta / \eta = 2.5d\phi / (1 - \phi / \phi_m). \quad (2.10)$$

Integrating Equation 2.10 with $\eta = \eta_0$ at $\phi = 0$ yields

$$\eta / \eta_0 = (1 - \phi / \phi_m)^{-2.5\phi_m}, \quad (2.11)$$

or

$$\eta_r = (1 - \phi / \phi_m)^{-2.5\phi_m}, \quad (2.12)$$

where η_r is the relative viscosity. Equations 2.11 and 2.12 are widely referred to as the Krieger-Dougherty equation. As $\phi \rightarrow 0$, Equation 2.11 reduces to Einstein's formula, which is shown in Equation 2.5. If $\phi \rightarrow \phi_m$, then the viscosity $\eta \rightarrow \infty$, corresponding to the close-packed situation. In many papers (Krieger & Dougherty, 1959; Fitch, 1997), the maximum volume fraction ϕ_m is referred to as the maximum packing fraction p .

So far what we have considered spherical particles. For arbitrarily shaped particles, Krieger and Dougherty (1959) introduced a dimensionless quantity, intrinsic viscosity $[\eta]$, which for suspensions is the dilute limit of the viscosity increment per unit particle volume fraction divided by the viscosity of the base liquid. It is defined as

$$[\eta] = \lim_{\phi \rightarrow 0} \frac{\eta - \eta_0}{\phi \eta_0}. \quad (2.13)$$

For spherical particles, $[\eta] = 2.5$, and for glass plates $[\eta] = 5.8$. The intrinsic viscosity of spherical particles in Equation 2.11 can be replaced by the intrinsic viscosity of arbitrarily shaped particles. Therefore, Equation 2.11 and 2.12 can be generalized to

$$\eta_r = \eta / \eta_0 = (1 - \phi / \phi_m)^{-[\eta]\phi_m}, \quad (2.14)$$

which enables us to estimate the viscosity for particles of any shape by choosing a suitable $[\eta]$ (Krieger and Dougherty). Generally, ϕ_m decreases as $[\eta]$ increases, while the product $[\eta]\phi_m$ usually remains in the range from 1.4 to 3 (Larson, 1999). For a latex/pressure-sensitive adhesive suspension system, Fletcher and Hill (n.d.) verified the above equation, finding that the viscosity increases with the volume fraction.

2.4 Viscosity and Particle Size Distribution

At a high volumn fraction, the viscosity of the liquid suspension strongly depends on the particle size distribution.

To evaluate the effect of particle size distribution on effective viscosity, first the contribution of particle size to the effective viscosity of liquid suspension in a monodisperse system needs to be evaluated. In 1950s and 1960s, many theoretical and experimental studies studies of monodisperse suspensions of particles at micron and sub-micron scales showed that at a constant volume fraction, the viscosity of liquid suspension decreases as the size of the suspended particles increases (Saunders, 1961; Sweeny & Geckler, 1954; Thomas, 1965).

The phenomenon can be explained by an approach proposed by Tao and Xu (2005). The effective viscosity depends on the freedom that the suspended particles have in the system. The less freedom the particles have, the faster the energy dissipates in the system, and the higher the effective viscosity of the suspension. Consider a monodisperse suspension system, with total number of particles N and total volume of the suspension V . The volume fraction ϕ of the spheres (particles) is

$$\phi = (4/3)\pi a^3 n, \quad (2.15)$$

where a is radius of the particle and n is the number density of particles N/V . The mean free path l or average distance a particle travels between collisions with other (“Mean Free Path”, n.d.) is given by

$$l = (n\sigma)^{-1}, \quad (2.16)$$

where σ is the effective cross-sectional area for collisions. In this case, σ has the same value as the surface area of a spherical particle, which is $4\pi a^2$. From Equation 2.15, n can be written in terms of particle radius a and volume fraction ϕ as

$$n = 3\phi / (4\pi a^3). \quad (2.17)$$

With σ replaced by $4\pi a^2$, substitution of n in Equation 2.16 with its expression in Equation 2.17 yields

$$l = ((3\phi / (4\pi a^3))(4\pi a^2))^{-1},$$

or

$$l = a / (3\phi). \quad (2.18)$$

According to Equation 2.18, as the radius of the particles increases, the mean free path increases, indicating that the particles have more free space to move in the suspension.

Thus the viscosity of the suspension goes down.

Thus far the thermal vibration of the particles in the suspension has not been taken into account. Increasing the size of the particles may also bring out another effect if the particles in the system experience thermal vibration. Consider a liquid suspension with noninteracting spheres with diameter of D suspended in a base liquid of viscosity η_0 . Here D equals to $2a$. The particles are treated classically ones since their diameters are of order of nanometers or micrometers. Due to the thermal vibration, particles in the suspension have larger effective diameters. The enlargement of the particle can be estimated. If particles in the system are undergoing thermal vibration and not flowing, the average kinetic energy is close to the thermal energy

$$\overline{\frac{1}{2}mv^2} \approx \frac{3}{2}k_B T. \quad (2.19)$$

Here m is the mass of the particle, v is the velocity, k_B is the Boltzmann constant, which has the value of $1.03806 \times 10^{-23} \text{ J} \cdot \text{K}^{-1}$, and T is the temperature in Kelvin.

According to Equation 2.19, the thermal velocity v_{th} (“Thermal Velocity”, 2008) is

$$v_{th} \approx \sqrt{3k_B T / m} . \quad (2.20)$$

Thus the diameter of the particles is enlarged by $\lambda = v_{th} t_0$ due to the thermal vibration.

We use t_0 for the relaxation time. Therefore, in the base liquid, the effective diameter of the particles is given by

$$D_{eff} = D + \lambda . \quad (2.21)$$

Correspondingly, the effective volume fraction and maximum volume fraction for the particles are

$$\phi_{eff} = \phi (D / D_{eff})^3 = \phi / (1 + \lambda / D)^3 , \quad (2.22)$$

and

$$\phi_{m-eff} = \phi_m (D / D_{eff})^3 = \phi_m / (1 + \lambda / D)^3 , \quad (2.23)$$

where $\phi_m \approx 0.64$ for random close packing situation (Jaeger & Nagel, 1992), while the maximum packing fraction for spheres was first conjectured by Kepler in 1611 and finally proved by Hales (1992) in a series of paper culminating in 1998. Thus, the relative viscosity η_r in Equation 2.14 should be replaced by

$$\eta_r = (1 - \phi_{eff} / \phi_{m-eff})^{-[\eta] \phi_{m-eff}} . \quad (2.24)$$

According to Equation 2.22 and 2.23,

$$\phi_{eff} / \phi_{m-eff} = \frac{\phi (D / D_{eff})^3}{\phi_m (D / D_{eff})^3} = \phi / \phi_m , \quad (2.25)$$

and the relative viscosity becomes

$$\eta_r = (1 - \phi / \phi_m)^{-[\eta]\phi_{m-eff}}. \quad (2.26)$$

According to Equation 2.23, as the diameter of the particles D increases, the effective maximum volume fraction ϕ_{m-eff} increases because the term $(1 + \lambda / D)^3$ decreases.

Clearly η_r , as given by Equation 2.26, decreases as ϕ_{m-eff} increases.

This result confirms that at a constant volume fraction ϕ , the viscosity of the suspension decreases as the size of the particles in it increases.

Vand (1948) proposed an equation for the relative viscosity of suspensions, which is an exponential equation as

$$\eta_r = \exp\left(\frac{\alpha_0 \phi}{1 - k\phi}\right), \quad (2.27)$$

where α_0 is a shape factor and k is a hydrodynamic interaction constant. Mooney's (1950) equation has the same form as Equation 2.27 with α_0 equal to 2.5, so

$$\eta_r = \exp\left(\frac{2.5\phi}{1 - k\phi}\right). \quad (2.28)$$

Matsumoto and Shermax (1969) analyzed suspensions with particles of diameter from $0.07 \mu m$ to $4 \mu m$ and derived an empirical equation for evaluating k , which is given by

$$k = 1.079 + \exp\left(\frac{0.01008}{D}\right) + \exp\left(\frac{0.00290}{D^2}\right), \quad (2.29)$$

where D is the diameter of the particles. It turned out that the value of k calculated by Equation 2.29 together with Equation 2.28 predict the relative viscosity of the suspensions very close to the experimental value measured by a capillary viscometer.

Figure 2.3 is a plot of relative viscosity versus volume fraction for particles with diameters of $0.07 \mu m$, $0.1 \mu m$ and $4 \mu m$ derived from Equation 2.28 and 2.29.

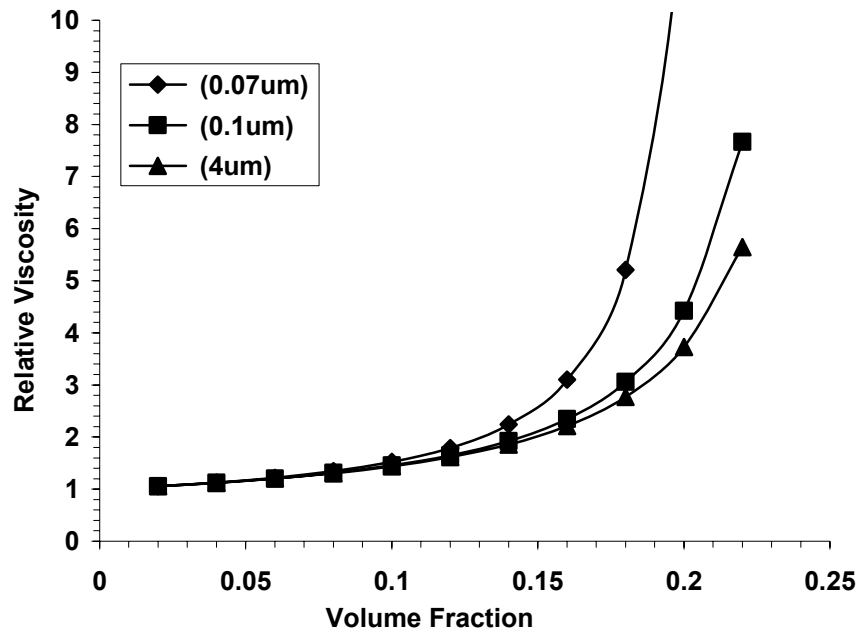


Figure 2.3. Dependence of Viscosity on Particle Size at Same Volume Percentage (Small Particle Diameters). Plot shows the relative viscosity versus volume fraction for monodispersed suspensions with particle diameters of $0.07 \mu m$, $0.1 \mu m$ and $4 \mu m$. Given the same volume fraction, relative viscosity increases with the decrease of particle size in the suspension.

The effect of the particle diameter on the viscosity of the suspension at the same volume fraction is clearly shown in the chart. For instance, a suspension of particles with diameter of $4.0 \mu m$ has approximately half the viscosity of a suspension with particles $0.05 \mu m$ in diameter.

In research conducted by Fletcher and Hill (n.d.), slightly larger particles were considered. A talc-epoxy system with talc particles with diameters of $5 \mu m$ and $19 \mu m$ was used to evaluate the effect of particle size on the viscosity. The result is shown in Figure 2.4.

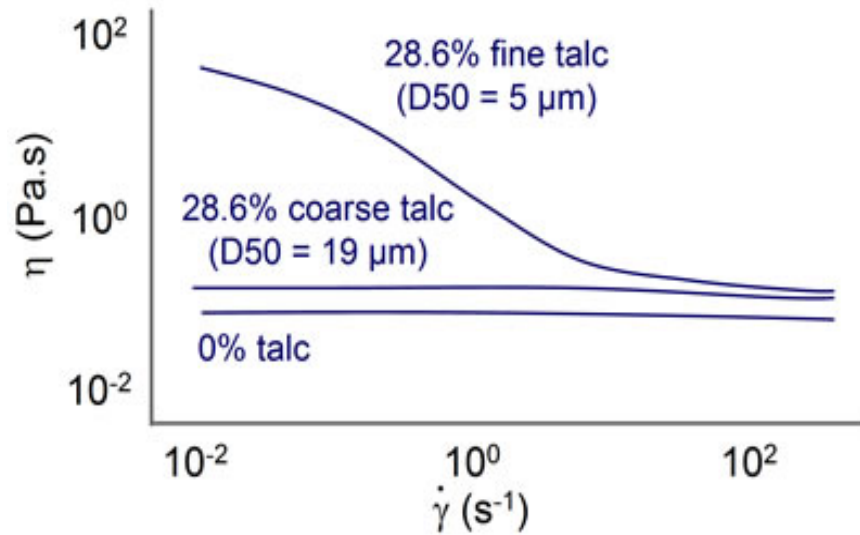


Figure 2.4. Dependence of Viscosity on Particle Size at Same Volume Percentage (Slightly Larger Particle Diameters). Diagram shows viscosity versus shear rate for base liquid and mono-dispersion systems with particle diameters of $5\ \mu\text{m}$ and $19\ \mu\text{m}$. The base liquid is Newtonian and the system with 28.6% coarse talc is still Newtonian, whereas the system with 28.6% fine talc has much higher viscosity at low shear rate and becomes non-Newtonian. Note. From Making the connection - particle size, size distribution and rheology. Fletcher & Hill, n.d., retrieved online (see reference). Adapted with kind permission.

Epoxy is a Newtonian fluid, served as the base liquid. Adding 28.6% volumn percentage of $19\ \mu\text{m}$ talc particles to the epoxy raises the viscosity of the suspension, but the suspension is still Newtonian, which is indicated by the constant viscosity with increasing shear rate. As the finer particles with diameter of $5\ \mu\text{m}$ were added to the epoxy, forming a suspension with the same volume percentage, the viscosity was significantly increased, especially at low shear rate.

This can be explained by colloidal repulsion between a relatively large number of particles which gives structure to the fluid, thus increasing resistance to the flow. In another study, Fletcher and Hill evaluated the effect of particle size with much larger

particles by employing pressure-sensitive adhesive as the base liquid and latex particles with diameter of $175\ \mu\text{m}$ and $750\ \mu\text{m}$, respectively, forming a suspension with a volume percentage of 50%. Their result is shown in Figure 2.5. We see that the suspension containing smaller particles has a higher viscosity than the one with larger particles for most of the shear rate. For very high shear rate, the viscosities become very close. Thus, it is well established that the size of the particles in monodisperse suspensions influences the viscosity of the system.

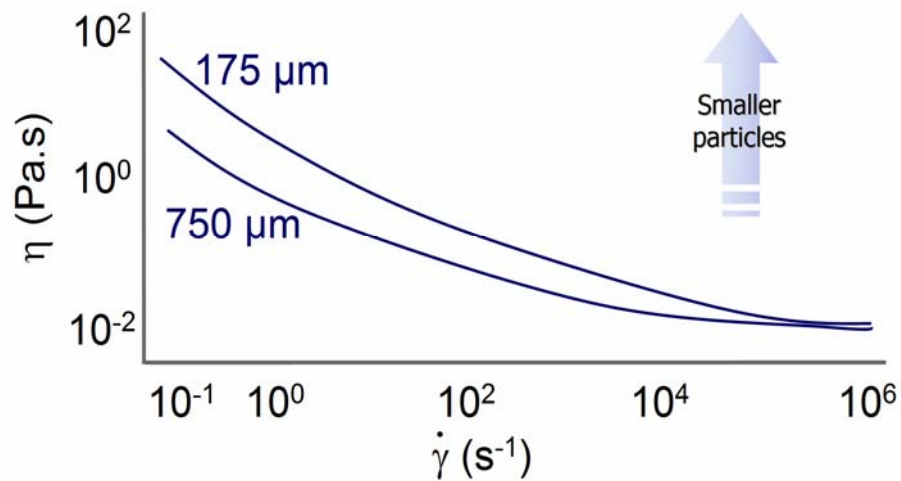


Figure 2.5. Dependence of Viscosity on Particle Size at Same Volume Percentage (Much Larger Particle Diameters). Diagram shows viscosity versus shear rate for mono-dispersed suspensions with particle diameters of $175\ \mu\text{m}$ and $750\ \mu\text{m}$. It is clearly shown that at the same volume fraction, the suspension with larger particle size has lower viscosity for most of the shear rate. Note. From Making the connection - particle size, size distribution and rheology, Fletcher & Hill, n.d., retrieved online (see reference). Adapted with kind permission.

So far, we have concentrated on monodispersed liquid suspensions. In reality, most liquid suspensions are polydisperse, i.e., contain of particles of different size. For a

liquid suspension of high volume fraction, the viscosity is highly dependent on the distribution of the particle size.

Actually, when particles of two different diameters are mixed, the viscosity can be much lower than it is for monodisperse suspensions with the same volume fraction (Larson, 1999). In 1970, Parkinson, Matsumoto and Sherman studied mixtures of several monodisperse suspensions of different sizes with different percentage in the mixed suspension. Their study led to a formula that relates the relative viscosity of the resulting suspension to the volume percentage and the diameter of each monodisperse suspension in the mixture. The formula is an extension of Mooney's equation (Equation 2.24) and has the form

$$\eta_r = \exp\left(\frac{2.5\phi_1}{1-k_1\phi_1}\right) \exp\left(\frac{2.5\phi_2}{1-k_2\phi_2}\right) \exp\left(\frac{2.5\phi_3}{1-k_3\phi_3}\right) \dots \exp\left(\frac{2.5\phi_n}{1-k_n\phi_n}\right),$$

or

$$\eta_r = \prod_{i=1 \rightarrow n} \exp\left(\frac{2.5\phi_i}{1-k_i\phi_i}\right), \quad (2.30)$$

where ϕ_i and k_i are the volume fraction and hydrodynamic interaction constant of the i th monodisperse suspension. The value of k_i can be calculated from the diameter of particle in the suspension using Equation 2.25. In Figure 2.6, the relative viscosity versus total volume fraction for bidisperse suspension with different percentages of large and small particles is plotted. The large and small particles in the suspension have diameter $0.5 \mu m$ and $0.1 \mu m$ respectively.

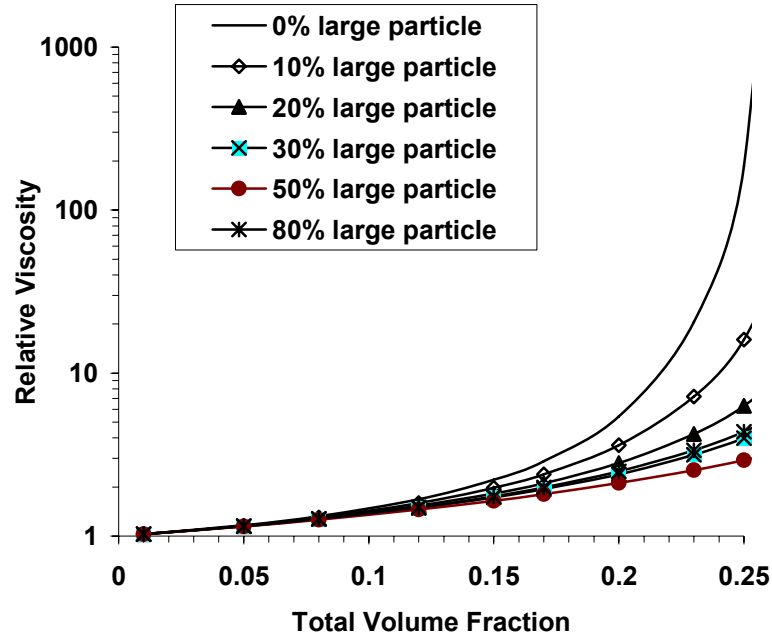


Figure 2.6. Dependence of Viscosity on Particle Distribution at Same Volume Percentage (Submicron Particles). The relative viscosity versus total particle volume fraction is plotted for bidisperse suspensions of particle-size ratio 5:1, with different particle-size distributions.

In Figure 2.6 we see that the relative viscosity drops 60 fold as the percentage of large particles increases from 0% to 50% at 0.25 of the total volume percentage. Then it increases again with a further increase of the fraction of large particles.

Fletcher and Hill (n.d.) also studied bidisperse suspensions made of epoxy and talc particles with diameters of $750 \mu m$ and $175 \mu m$. The total volume fraction is 0.5. The result is shown in Figure 2.7.

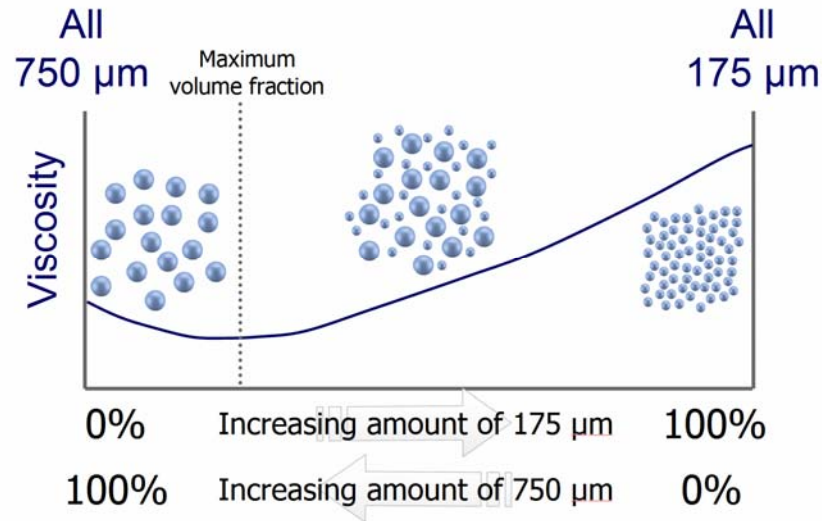


Figure 2.7. Dependence of Viscosity on Particle Distribution at Same Volume Percentage (Micron Particles). Viscosity as a function of fraction of large or small talc particles are plotted for bidisperse suspension with coarse particles of $750 \mu\text{m}$ in diameter and fine particles of $150 \mu\text{m}$ in diameter. Note. From Making the connection - particle size, size distribution and rheology. Fletcher & Hill, n.d., retrieved online (see reference). Adapted with kind permission.

Their study led to a similar conclusion. This could be explained analytically with Equation 2.26,. For a bidisperse suspension, the relative viscosity is given by

$$\exp\left[2.5\phi_1 / (1 - k_1\phi_1)\right] \exp\left[2.5\phi_2 / (1 - k_2\phi_2)\right], \text{ or}$$

$$\exp\left[2.5\phi_1 / (1 - k_1\phi_1) + 2.5\phi_2 / (1 - k_2\phi_2)\right], \text{ where } \phi_1 + \phi_2 \text{ is the total volume fraction.}$$

Assume k_1 and k_2 are hydrodynamic interaction constants for smaller and larger particles respectively. We know that $k_1 > k_2$ from Equation 2.25. Now consider a

suspension of the same volume fraction $\phi_1 + \phi_2$ of monodispersion of fine particles. Its

$$\text{relative viscosity is } \exp\left\{2.5(\phi_1 + \phi_2) / [1 - k_1(\phi_1 + \phi_2)]\right\}, \text{ or}$$

$$\exp\left\{2.5\phi_1 / [1 - k_1(\phi_1 + \phi_2)] + 2.5\phi_2 / [1 - k_1(\phi_1 + \phi_2)]\right\}. \text{ Since } 1 / [1 - k_1(\phi_1 + \phi_2)] \text{ is bigger}$$

than $1/(1-k_1\phi_1)$ or $1/(1-k_2\phi_2)$, the viscosity of the suspension with only fine particles apparently has a larger viscosity than the bidisperse suspension. Experiments done by Serge and Silberberg (1962) also showed that in flow through capillary tubes, the viscosity was further reduced for large suspended particles because of a tendency for large particles to migrate toward the center of the tube.

In summary our discussion indicates that on keeping a constant volume fraction ϕ , increasing the size of the particles and the polydispersity of the suspension leads to the reduction of the viscosity.

2.5 Polarization of Particles in External Field

Dielectric particles become polarized in an external electric field, whereas magnetic particles become polarized in an external magnetic field. After polarization these particles possess electric or magnetic dipole moments. The induced dipoles interact with each other and produce attractive forces among these particles. The following discussion focuses on what happens to suspensions in an electric field. For suspensions in a magnetic field the analysis and results are similar.

2.5.1 Polarization of Dielectrics in Electric Field

Dielectrics become polarized in electric field. Unlike conductors, there are no free electrons in dielectrics. Instead the electrons are tightly bound by the nuclei. In the absence of an external electric field, the nucleus is at the center of the electron clouds. The centers of the negative charges (electron clouds) and the positive charge (nucleus) coincides. In the present of an external field, electron cloud is shifted away from the original position until the external force is balanced by the internal restoring force due to the nucleus. Since the center of the electron cloud no longer coincides with the nucleus, the atom is polarized in the external field, as is shown in Figure 2.8.

Macroscopically, dielectrics are polarized in external field due to the polarization of the individual atoms that they are made of. As the electron clouds of all the atoms shift opposite to the direction of the electric field, the side where the electric field enters becomes negative and the opposite side becomes positive. The polarization of a dielectric slab and a dielectric sphere is shown in Figure 2.9.

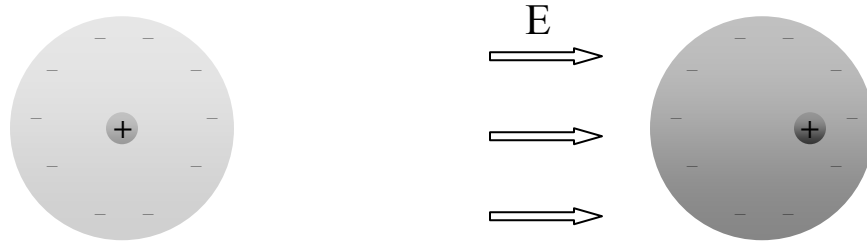


Figure 2.8. Polarization of Dielectric Atom in Electric Field. In the absence of electric field, the nucleus is at the center of the electron clouds and the atom is neutral. In the presence of an external field, electron clouds shift and the atom becomes polarized.

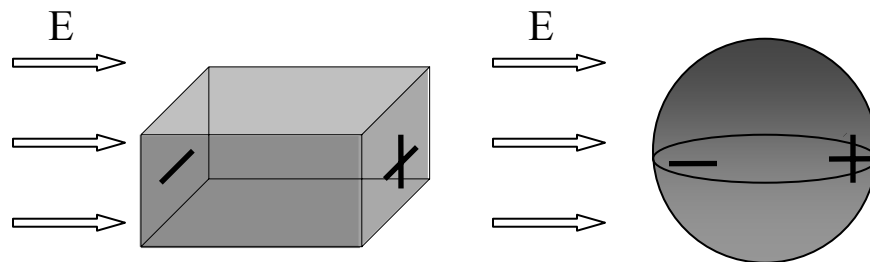


Figure 2.9. Polarization of Dielectric Slab and Sphere. In an electric field directed to the right, the left side of dielectric becomes negative and the opposite side becomes positive, as a result of the polarization of the dielectric atoms.

2.5.2 Dipole Moment of Dielectric Spheres in Electric Field

Dielectric spheres in electric field have dipole moments, and their dipolar interactions are discussed in many books (Grant & Phillips, 1975; Greiner, 1998; Masliyah & Bhattacharjee, 2006). However, the approach for solving this problem is important to our discussion. Thus it is repeated here.

Consider a liquid suspension composed of spherical particles of diameter a , with permittivity ϵ_p and fluid with permittivity ϵ_f , as shown in Figure 2.10.

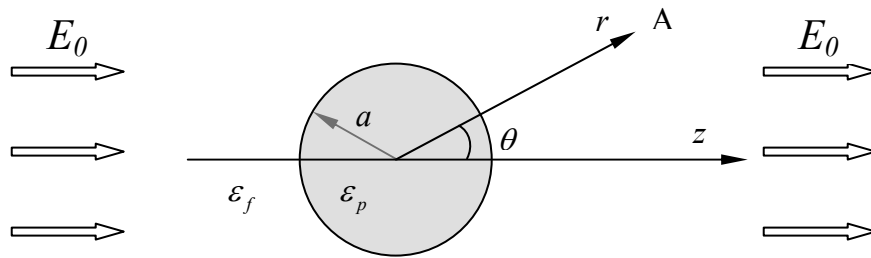


Figure 2.10. Polarization of Dielectric Particle in Liquid Base. The external electric field is \vec{E}_0 . Permittivity of the particle and fluid are ϵ_p and ϵ_f , respectively. The particle is sphere with radius of a .

If an electric field \vec{E}_0 in the z direction is applied, these particles are polarized in the field and become dipoles with dipole moment of \vec{p} . To calculate the dipole moment, we start by considering an arbitrary point A , which has a distance \vec{r} from the center of the particle and makes an angle θ to the field, and then analyze the field inside

and outside the particle by applying boundary conditions. Let's begin with Maxwell's equations. Assuming there is no magnetic field present,

$$\nabla \times \vec{E} = 0, \quad \nabla \cdot \vec{D} = \rho_f, \quad (2.31)$$

where ρ_f is the free charge density. There is no free charge in the liquid suspension since both particles and fluid are dielectrics. Thus $\rho_f = 0$ and Equation 2.31 becomes

$$\nabla \times \vec{E} = 0, \quad \nabla \cdot \vec{D} = 0. \quad (2.32)$$

The left equation in Equation 2.32 implies that \vec{E} can be written as

$$\vec{E} = -\nabla \phi, \quad (2.33)$$

where ϕ is the electric scalar potential. In spherical coordinates, \vec{E} has the normal component

$$E_r = -\frac{\partial \phi}{\partial r}, \quad (2.34)$$

and the tangential component

$$E_\theta = -\frac{1}{r} \frac{\partial \phi}{\partial \theta}. \quad (2.35)$$

Equation 2.33 and the right equation in Equation 2.32 imply Laplace's equation

$$\nabla^2 \phi = 0. \quad (2.36)$$

Assuming that the electric potential is independent of the azimuthal angle ϕ , Laplace's equation in spherical coordinates takes the form,

$$\frac{1}{r^2} \frac{\partial}{\partial r} \left(r^2 \frac{\partial \phi}{\partial r} \right) + \frac{1}{r^2 \sin \theta} \frac{\partial}{\partial \theta} \left(\sin \theta \frac{\partial \phi}{\partial \theta} \right) = 0. \quad (2.37)$$

Applying the method of separation of variables, we assume ϕ can be written as

$$\phi(r, \theta) = \Gamma(r)\Theta(\theta). \quad (2.38)$$

Using Equation 2.38, Equation 2.37 becomes, after rearrangement,

$$\frac{1}{\Gamma(r)} \frac{\partial}{\partial r} \left(r^2 \frac{\partial \Gamma(r)}{\partial r} \right) + \frac{1}{\Theta(\theta) \sin \theta} \frac{\partial}{\partial \theta} \left(\sin \theta \frac{\partial \Theta(\theta)}{\partial \theta} \right) = 0, \quad (2.39)$$

where the first term in Equation 2.39 is purely a function of r and the second term is a function of θ . Since the equation holds for all values of r and θ , both terms must be constants. Therefore, Equation 2.39 splits into two equations,

$$\frac{1}{\Gamma(r)} \frac{\partial}{\partial r} \left(r^2 \frac{\partial \Gamma(r)}{\partial r} \right) = k^2, \quad (2.40)$$

and

$$\frac{1}{\Theta(\theta) \sin \theta} \frac{\partial}{\partial \theta} \left(\sin \theta \frac{\partial \Theta(\theta)}{\partial \theta} \right) = -k^2, \quad (2.41)$$

where k is the separation constant. Equation 2.40 has a solution of the form

$$\Gamma_l(r) = A_l r^l + B_l r^{-(l+1)}, \quad (2.42)$$

where A_l and B_l will be determined by boundary conditions later. The quantities k and l are related by

$$l(l+1) = k^2,$$

where $l = 0, 1, 2, \dots$. The solutions of Equation 2.41 are called Legendre polynomial,

$$\Theta_l(\theta) = P_l(\cos \theta). \quad (2.43)$$

They can be calculated by Rodrigues formula, which has the form

$$P_l(x) = \frac{1}{2^l l!} \frac{d^l}{dx^l} (x^2 - 1)^l.$$

The first three Legendre polynomials are given in Table 2.1.

Table 2.1 First Three Legendre Polynomials

l	$P_l(\cos \theta) / \Theta_l(\theta)$
0	1
1	$\cos \theta$
2	$\frac{1}{2}(3 \cos^2 \theta - 1)$
3	$\frac{1}{2}(5 \cos^3 \theta - 3 \cos \theta)$

From Equation 2.38, 2.42 and 2.43, we have found that

$$\varphi_l(r, \theta) = [A_l r^l + B_l r^{-(l+1)}] P_l(\cos \theta)$$

are all solutions of Equation 2.30, where $l = 0, 1, 2, \dots$. Thus the general solution to

Laplace's equation can be written as

$$\varphi(r, \theta) = \sum_{l=0}^{\infty} [A_l r^l + B_l r^{-(l+1)}] P_l(\cos \theta). \quad (2.44)$$

Equation 2.44 is the general expression for the electric potential in spherical coordinates. Electric potential inside the dielectric sphere can not be infinitely large as $r \rightarrow 0$. This condition requires $B_l = 0$, so electric potentials inside and outside the particle are,

$$\varphi_{in}(r, \theta) = \sum_{l=0}^{\infty} A_l r^l P_l(\cos \theta) \quad \text{for } r < a, \quad (2.45)$$

$$\varphi_{out}(r, \theta) = \sum_{l=0}^{\infty} [A'_l r^l + B'_l r^{-(l+1)}] P_l(\cos \theta) \quad \text{for } r > a, \quad (2.46)$$

where A_l , A'_l and B'_l are to be determined from the boundary conditions. Consider a point at infinity. The only contribution arises from z component of external field potential. Since $\vec{E} = -\nabla\varphi$,

$$\varphi_{out}(r \rightarrow \infty, \theta) = -\vec{E}_0 \cdot \vec{r},$$

or

$$\varphi_{out}(r \rightarrow \infty, \theta) = -E_0 r \cos \theta. \quad (2.47)$$

Since that $P_1(\cos \theta) = \cos \theta$, according to equation 2.46 and 2.47, we find that the only nonvanishing A'_l is $A'_1 = -E_0$. From the boundary conditions on the interface of the particle and the fluid at $r = a$, the other coefficients can be determined. Equation 2.32 implies two boundary conditions. From $\nabla \times \vec{E} = 0$ and Stoke's theorem ($\int_S (\nabla \times \vec{E}) \cdot \vec{n} dS = \oint_c \vec{E} \cdot d\vec{l}$), we know that the tangential component of \vec{E} is continuous, which with Equation 2.35, gives

$$\left(-\frac{1}{r} \frac{\partial \varphi_{in}}{\partial \theta} \right) \Big|_{r=a} = \left(-\frac{1}{r} \frac{\partial \varphi_{out}}{\partial \theta} \right) \Big|_{r=a}. \quad (2.48)$$

Another boundary condition is derived from $\nabla \cdot \vec{D} = 0$ and Gauss's theorem

($\int_V (\nabla \cdot \vec{D}) dV = \oint_S (\vec{D} \cdot \vec{n}) dS$). The normal component of \vec{D} is continuous, which with

Equation 2.34 and $D = \varepsilon E$, implies

$$-\varepsilon_p \frac{\partial \varphi_{in}}{\partial r} \Big|_{r=a} = -\varepsilon_f \frac{\partial \varphi_{out}}{\partial r} \Big|_{r=a}. \quad (2.49)$$

From Equations 2.45, 2.46 and 2.48, we get

$$\sum_{l=0}^{\infty} A_l a^l \frac{dP_l(\cos \theta)}{d\theta} = \sum_{l=0}^{\infty} \left[-E_0 a^l \delta_{1l} + B'_l a^{-(l+1)} \right] \frac{dP_l(\cos \theta)}{d\theta}, \quad (2.50)$$

where $\delta_{l1} = 0$ for all $l \neq 1$. Since Equation 2.50 must be satisfied for all θ , the coefficients for the derivative of each Legendre Polynomials should be equal, and hence

$$A_1 = -E_0 + B'_1 a^{-3} \quad (2.51)$$

and

$$A_l = B'_l a^{-(2l+1)}, \text{ for } l \neq 1. \quad (2.52)$$

Starting from Equation 2.49 together with Equation 2.45, 2.46 and 2.47, another boundary equation can be derived,

$$\sum_{l=0}^{\infty} l A_l a^{l-1} P_l(\cos \theta) = \sum_{l=0}^{\infty} \left[-E_0 a^{l-1} \delta_{l1} - B'_l (l+2) a^{-(l+1)} \right] P_l(\cos \theta), \quad (2.53)$$

which gives rise to the equations

$$\frac{\varepsilon_p}{\varepsilon_f} A_1 = -E_0 - 2B'_1 a^{-3} \quad (2.54)$$

and

$$\frac{\varepsilon_p}{\varepsilon_f} l A_l = -(l+1) B'_l a^{-(2l+1)} \text{ for } l \neq 1. \quad (2.55)$$

It follows from Equation 2.52 and 2.55 that all A_l and B'_l vanish for $l \neq 1$. Solving Equation 2.51 and 2.54 for A_1 and B'_1 gives

$$A_1 = -\frac{3\varepsilon_f}{\varepsilon_p + 2\varepsilon_f} E_0,$$

and

$$B'_1 = \frac{\varepsilon_p - \varepsilon_f}{\varepsilon_p + 2\varepsilon_f} a^3 E_0.$$

Therefore the electric potentials inside and outside the dielectric particle are

$$\varphi_{in}(r, \theta) = -\frac{3\varepsilon_f}{\varepsilon_p + 2\varepsilon_f} E_0 r \cos \theta, \text{ for } r < a,$$

and

$$\varphi_{out}(r, \theta) = -E_0 r \cos \theta + \left(\frac{\varepsilon_p - \varepsilon_f}{\varepsilon_p + 2\varepsilon_f} E_0 a^3 \right) \frac{1}{r^2} \cos \theta, \text{ for } r > a. \quad (2.56)$$

The electric potential in an external field and dipole field is

$$\varphi(\vec{r}) = -\vec{E} \cdot \vec{r} + \frac{1}{4\pi\varepsilon_f} \frac{\vec{p} \cdot \vec{r}}{r^3}, \quad (2.57)$$

where ε_f is the permittivity of the base fluid and \vec{p} is the dipole moment. Comparing Equation 2.56 and 2.57 leads to the dipole moment of a dielectric spherical particle in external field \vec{E}_0 ,

$$\vec{p} = 4\pi\varepsilon_f \frac{\varepsilon_p - \varepsilon_f}{\varepsilon_p + 2\varepsilon_f} \vec{E}_0 a^3, \quad (2.58)$$

which has the same direction as the external field. The electric potential due to the dipole moment is

$$\varphi_p(\vec{r}) = \frac{1}{4\pi\varepsilon_f} \frac{\vec{p} \cdot \vec{r}}{r^3}.$$

2.5.3 Electric Dipole Field, Dipolar Interaction and Forces between Dipoles

Recalling the relationship $E = -\nabla\varphi$ between the electric field and the electric potential, , thus we write the electric field of a dipole as

$$\vec{E}_p = -\nabla \left(\frac{1}{4\pi\varepsilon_f} \frac{\vec{p} \cdot \vec{r}}{r^3} \right). \quad (2.59)$$

Here $\vec{p} \cdot \vec{r} = pr \cos \theta$, and in spherical coordinates

$$\nabla = \frac{\partial}{\partial r} \hat{r} + \frac{1}{r} \frac{\partial}{\partial \theta} \hat{\theta} + \frac{1}{r \sin \theta} \frac{\partial}{\partial \phi} \hat{\phi}, \quad (2.60)$$

where \hat{r} , $\hat{\theta}$, and $\hat{\phi}$ are unit vectors in the r , θ , and ϕ directions, respectively.

With no component in the ϕ direction, Equation 2.59 becomes

$$\vec{E}_p = \frac{1}{4\pi\epsilon_f} \left(2 \frac{p \cos \theta}{r^3} \hat{r} + \frac{p \sin \theta}{r^3} \hat{\theta} \right). \quad (2.61)$$

This is the electric field due to the dipole moment. It has both r and θ components.

The interaction energy between two dipoles is

$$U = -\vec{p} \cdot \vec{E}_p. \quad (2.62)$$

Since \vec{p} is in the z direction, with the geometric relationship among \hat{r} , $\hat{\theta}$, and \hat{z} ,

shown in Figure 2.11, \vec{p} can be written as

$$\vec{p} = p \cos \theta \hat{r} - p \sin \theta \hat{\theta}. \quad (2.63)$$

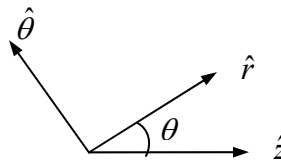


Figure 2.11. Relationship among Unit Vectors \hat{r} , $\hat{\theta}$, and \hat{z} . The angle between \hat{r} and \hat{z} is θ , while \hat{r} and $\hat{\theta}$ are perpendicular.

From Equations 2.61, 2.62, and 2.63, after simplification, the interaction between two dipoles becomes

$$U = \frac{1}{4\pi\epsilon_f} \frac{p^2(1-3\cos^2\theta)}{r^3}, \quad (2.64)$$

where r is the distance between two dipoles and θ is the angle between the external field (recall the external field is in the z direction) and line joining two dipoles.

The force between two dipoles is given by

$$\vec{F} = -\nabla U. \quad (2.65)$$

From Equation 2.60 and 2.65, the force in spherical coordinates is

$$\vec{F} = \frac{p^2}{4\pi\epsilon_f} \left[\frac{\partial}{\partial r} \left(\frac{1-3\cos^2\theta}{r^3} \right) \hat{r} + \frac{1}{r} \frac{\partial}{\partial \theta} \left(\frac{1-3\cos^2\theta}{r^3} \right) \hat{\theta} \right],$$

which yields,

$$\vec{F} = \frac{1}{4\pi\epsilon_f} \frac{3p^2}{r^4} \left[(1-3\cos^2\theta) \hat{r} - 2\sin(2\theta) \hat{\theta} \right] \quad (2.66)$$

after simplification. What concerns us most is the radial component of the force. For two dipoles on the z axis, the force is

$$\vec{F} = -\frac{1}{2\pi\epsilon_f} \frac{3p^2}{r^4} \hat{r}. \quad (2.67)$$

The negative sign in Equation 2.67 indicates an attractive force.

2.5.4 Magnetic Dipole, the Field, Interaction and Forces between Dipoles

For magnetic dipoles, the magnetic field, the interaction between two dipoles, and the force between them are analogous to those of their electric counterparts. We will not discuss the details in the derivation but go directly to the results.

The induced magnetic dipole moment of a permeable particle in external magnetic field $\overline{H_0}$ with permeability of μ_p and diameter a , which is suspended in liquid with permeability μ_f , is given by

$$\overline{m} = 4\pi \frac{\mu_p - \mu_f}{\mu_p + 2\mu_f} \overline{H_0} a^3. \quad (2.68)$$

The interaction energy between two magnetic dipoles is

$$U = \frac{\mu_f}{4\pi} \frac{m^2 (1 - 3 \cos^2 \theta)}{r^3}, \quad (2.69)$$

where θ is the angle between the external field and line joining two dipoles. The force between the two dipoles is given by

$$\overline{F} = \frac{\mu_f}{4\pi} \frac{3m^2}{r^4} \left[(1 - 3 \cos^2 \theta) \hat{r} - 2 \sin(2\theta) \hat{\theta} \right]. \quad (2.70)$$

The direction of the attractive force between two dipoles is parallel to the external field, and for $\theta = 0$, the force them reduces to

$$\overline{F} = -\frac{\mu_f}{2\pi} \frac{3m^2}{r^4} \hat{r}. \quad (2.71)$$

2.6 Brownian Motion, Langevin's Theory and Diffusion Coefficient

2.6.1 Brownian Motion

Brownian motion was first observed by Scottish botanist Robert Brown in 1827 and named after him (Everett, 1988). It is the phenomenon that small suspended particles move randomly in a liquid, due to collisions with surrounding molecules in the liquid the particles.

Einstein realized that small particles immersed in a "bath" of surrounding molecules behave as very large molecules because they are in thermodynamic equilibrium with the molecules in the bath (Haw, 2005). The kinetic theory, together with the principle of equipartition of energy, predicts that liquid or gas molecules have mean kinetic energy $\frac{3}{2}k_B T$. Thus the kinetic energy of a particle in Brownian motion is

$$\overline{E} = \frac{1}{2}m\overline{v^2} = \frac{3}{2}k_B T ,$$

where m is the mass of the particle, $\overline{v^2}$ is the mean square velocity taken over relatively long time, k_B is the Boltzman constant, and T is the temperature. In one dimension, the kinetic energy is

$$\overline{E} = \frac{1}{2}k_B T . \tag{2.72}$$

2.6.2 Langevin's Theory

In 1908, Langevin gave a theoretical treatment of Brownian motion assuming that the molecular collisions driving the motion are completely random, and the motions in

the three dimensions are uncorrelated. Thus, the motions in each dimension can be treated separately and added.

For motion in the x direction, Equation 2.72 can be written as

$$\overline{E} = \frac{1}{2} m \overline{v_x^2} = \frac{1}{2} k_B T ,$$

and since velocity is the time derivative of displacement,

$$m \overline{\left(\frac{dx}{dt} \right)^2} = k_B T . \quad (2.73)$$

When a spherical particle with mass m and radius a undergoes Brownian motion, it experiences a viscous drag force and a “noise force” from random thermal collisions. From Stokes’ law we know the magnitude of the drag force is

$$F = -6\pi a \eta_0 v , \quad (2.74)$$

where η_0 is the dynamic viscosity of the liquid in unit of $Pa \cdot s$ and v is the velocity of the particle. Newton’s second law takes the form

$$m \frac{d^2 x}{dt^2} = -6\pi a \eta_0 \frac{dx}{dt} + F(t) , \quad (2.75)$$

where $F(t)$ is the noise force. This equation is known as the Langevin equation.

2.6.3 Diffusion Coefficient

Multiplying Equation 2.75 by x on both sides, we rewrite it as

$$m \frac{d}{dt} \left(x \frac{dx}{dt} \right) - m \left(\frac{dx}{dt} \right) \left(\frac{dx}{dt} \right) = -6\pi a \eta_0 x \frac{d}{dt} x + x F(t) ,$$

which further simplifies to

$$\frac{m}{2} \frac{d^2}{dt^2} x^2 - m \left(\frac{dx}{dt} \right)^2 = -3\pi a \eta_0 \frac{d}{dt} x^2 + xF(t). \quad (2.76)$$

On averaging over time, Equation 2.76 yields

$$\frac{m}{2} \frac{d^2}{dt^2} \overline{x^2} - m \overline{\left(\frac{dx}{dt} \right)^2} = -3\pi a \eta_0 \frac{d}{dt} \overline{x^2}, \quad (2.77)$$

since the average of the noise term $\overline{xF(t)}$ vanishes. From Equation 2.73 and 2.77, we obtain

$$\frac{m}{2} \frac{d^2}{dt^2} \overline{x^2} + 3\pi a \eta_0 \frac{d}{dt} \overline{x^2} = k_B T. \quad (2.78)$$

The solution to Equation 2.78 is

$$\overline{x^2(t)} = \frac{k_B T}{3\pi a \eta_0} t + C_1 \exp\left(-\frac{6\pi a \eta_0}{m} t\right) + C_2. \quad (2.79)$$

The second term in Equation 2.79 is only important for very small t . For instance, for a particle with diameter of $1 \mu m$ and density close to water suspended in water with viscosity that $0.001 Pa \cdot s$, the coefficient $6\pi a \eta_0 / m$ has the value $4.5 \times 10^6 s^{-1}$. This means that the second term in Equation 2.79 is negligible after $1 \mu s$. So there is no contribution from this term in our time frame, which is in the range of seconds or longer. If at $t = 0$ the particle is at the origin, then the third term vanishes as well. With these assumption Equation 2.79 simplifies to

$$\overline{x^2(t)} = \frac{k_B T}{3\pi a \eta_0} t. \quad (2.80)$$

The diffusion coefficient can be evaluated from the convection-diffusion equation without the convection term in this case, which is

$$\frac{\partial n}{\partial t} = D \frac{\partial^2 n}{\partial x^2}, \quad (2.81)$$

where $n(x, t)$ is the number of particles per unit volume at distance x and time t , and D is the diffusion coefficient. The boundary conditions are $n(\pm\infty, t) = 0$ for all t . If initially all the particles are at $x = 0$ and there are no particles elsewhere, $n(x, 0) = N\delta(x)$. The corresponding solution of Equation 2.81 is given by the Gaussian distribution

$$n(x, t) = \frac{N}{2\sqrt{\pi Dt}} \exp\left(-\frac{x^2}{4Dt}\right), \quad (2.82)$$

where

$$N = \int_{-\infty}^{\infty} n(x, t) dx$$

is the number of particles released at $x = 0$ per unit cross-section area. The mean square displacement from $x = 0$ at time t has the form

$$\overline{x^2(t)} = \frac{1}{N} \int_{-\infty}^{\infty} x^2(t) n(x, t) dx. \quad (2.83)$$

With Equation 2.82, Equation 2.83 implies

$$\overline{x^2(t)} = 2Dt. \quad (2.84)$$

Comparing Equation 2.84 with Equation 2.80 immediately yields the formula for the diffusion coefficient

$$D = \frac{k_B T}{6\pi a \eta_0}. \quad (2.85)$$

2.7 Reducing the Viscosity of Liquid Suspension by Electric or Magnetic Field

From the analysis in section 2.4 and 2.5, it is clear that at a constant volume fraction, the effective viscosity of the suspension is reduced if small particles in the liquid suspension aggregate together into larger ones. For most suspensions, this can be realized with either electric or magnetic field by polarizing these particles and aggregating them through dipole attraction.

2.7.1 Reducing the Viscosity by Electric Field

For a dielectric particle with diameter a and permittivity ε_p suspended in base liquid with permittivity ε_f , in the presence of an external electric field \vec{E}_0 , the particle is polarized with dipole moment $\vec{p} = 4\pi\varepsilon_f(\varepsilon_p - \varepsilon_f)/(\varepsilon_p + 2\varepsilon_f)\vec{E}_0a^3$ (refer to Equation 2.58). Equation 2.64 gives the interaction energy of two induced electric dipoles, which is $U = p^2(1 - 3\cos^2\theta)/(4\pi\varepsilon_f r^3)$, with r being the distance between two dipoles and θ being the angle between the external field and the line joining two dipoles.

If the interaction is strong enough to overcome the Brownian motion, the particles aggregate and align in the field direction. If the external field is so strong that the particles in the suspension quickly form macroscopic chains or columns jamming the liquid flow, the viscosity of the suspension increases, which is a well-known phenomenon in magnetorheological (MR) and electrorheological (ER) fluids (Ginder & Davis, 1994; Tao, 2001; Tao & Sun, 1991; Wittle & Bullough, 1992;).

However, if the electric field is applied in such a short pulse that the dipolar interaction is not sufficient to affect particles separated by macroscopic distances but

sufficient to assemble nearby ones, the assembled clusters are of limited size in the micrometer range. Some particles in the liquid suspension may not participate in the aggregation, while other particles aggregate, forming larger particles. During the application of the field, the viscosity changes rapidly. After the electric field is off, the suspension has a lower viscosity. This follows from the facts and discussion of section 2.4. While the volume fraction remains the same, larger size and polydispersity of the suspended particles favor a viscosity decrease of the suspension.

It is important to note that this viscosity reduction does not come from a change of temperature. The reduction becomes more pronounced as the volume fraction ϕ increases. Thus the electric or magnetic field pulse is more effective in dense suspensions than in dilute ones.

2.7.2 Critical Electric Field

The critical electric field E_c required for the formation of clusters can be estimated as follows. In a suspension with number density of suspended particles n , the volume occupied by one particle is $1/n$. Therefore, the typical separation between two adjacent particles is about $n^{-1/3}$. With r in Equation 2.64 replaced by $n^{-1/3}$, the dipolar interaction between two particles is

$$U = np^2(1 - 3\cos^2\theta) / (4\pi\epsilon_f). \quad (2.86)$$

This interaction must overcome the thermal Brownian motion in order to pull the particles together. This requires

$$U \geq \frac{3}{2}k_B T, \quad (2.87)$$

which, with Equation 2.86, becomes

$$-np^2(1-3\cos^2\theta)/(4\pi\varepsilon_f) \geq \frac{3}{2}k_B T,$$

which with $\theta = 0$, reduces to,

$$np^2/(\pi\varepsilon_f) \geq k_B T. \quad (2.88)$$

From Equation 2.58 and 2.88, we have

$$E_0 \geq \frac{1}{4a^3} \left(\frac{3k_B T}{\pi\varepsilon_f n} \right)^{1/2} \left(\frac{\varepsilon_p + 2\varepsilon_f}{\varepsilon_p - \varepsilon_f} \right),$$

where k_B is the Boltzmann constant and T is the absolute temperature. Thus, the critical electric field E_c is estimated to be

$$E_c = \frac{1}{4a^3} \left(\frac{3k_B T}{\pi\varepsilon_f n} \right)^{1/2} \left(\frac{\varepsilon_p + 2\varepsilon_f}{\varepsilon_p - \varepsilon_f} \right). \quad (2.89)$$

In order to change the viscosity of the liquid suspension, the applied electric field should be bigger than E_c .

2.7.3 Minimal Field Pulse Duration

To estimate the minimal field pulse duration required to aggregate the particles, Equation 2.67 is used. The force between two adjacent particles is about

$(3/2\pi\varepsilon_f)p^2n^{4/3}$. According to Equation 2.74, Stoke's drag force has the magnitude

$6a\pi\eta_0v$. These two forces balance if

$$(3/2\pi\varepsilon_f)p^2n^{4/3} = 6a\pi\eta_0v,$$

which yields the average velocity

$$v = p^2 n^{4/3} / (4\pi^2 \varepsilon_f \eta_0 a). \quad (2.90)$$

The time required for two adjacent particles to come together is about

$$\tau = r / v = n^{-1/3} / v.$$

With Equation 2.58 and 2.90, this becomes

$$\tau = \eta_0 (\varepsilon_p + 2\varepsilon_f)^2 / [4\varepsilon_f n^{5/3} a^5 (\varepsilon_p - \varepsilon_f)^2 E_0^2]. \quad (2.91)$$

If the electric field pulse is much shorter than τ , the time duration is insufficient for the aggregation of the particles. However, if the field is on for a period much longer than τ , macroscopic chains form and jam the flow, which is unfavorable for viscosity reduction. Therefore, in order to reduce the viscosity of the liquid suspension, the pulse duration for the field should be of order τ .

2.7.4 Critical Field and Minimal Pulse Duration in the Presence of Magnetic Field

If the electric field is replaced by a magnetic field, from Equation 2.68, 2.69 and 2.87, a similar estimate for the critical magnetic field gives

$$H_c = \frac{1}{4a^3} \left(\frac{3k_B T}{\pi n \mu_f} \right)^{1/2} \left(\frac{\mu_p + 2\mu_f}{\mu_p - \mu_f} \right). \quad (2.92)$$

From Equation 2.71, 2.74, and 2.92, the minimal pulse duration is

$$\tau = \eta_0 (\mu_p + 2\mu_f)^2 / [4\mu_f n^{5/3} a^5 (\mu_p - \mu_f)^2 H_0^2]. \quad (2.93)$$

2.7.5 Field Application Duration, Direction and System Relaxation Time

Unlike the case of ER and MR fluids, our approach reduces the viscosities of liquid suspensions by the application of an electric field or magnetic field above the critical field for a short period, usually within a couple of seconds. During the application

of the field, particles may undergo rotation due to resulting torques. Thus, the viscosity of the liquid suspension system is steady and varies with time. However, the system quickly evolves to a quasi-stable state when the field is turned off as a consequence of the disappearance of the polarization forces or torques. By choosing the proper direction of the applied field, the viscosity can be further reduced by suppressing the particle rotation. For instance, the aggregated particles form ellipsoid-like shapes with their long axis parallel to the applied field (Promislow & Gast, 1996). If the field direction is parallel to the flow direction, these ellipsoids do not rotate in the flow, and the viscosity can thus be further reduced.

Particles in a liquid suspension undergo Brownian motion. When the field is turned off, the dipolar interaction and attractive forces between the aggregated particles disappear, and they gradually dissemble. Therefore, the viscosity of the suspension gradually increases and returns to its original value after all aggregated particles disintegrate. The time this takes can be estimated as follows. In absence of other disturbances, such as in a stationary or a constant flow state, the particles in the suspension separate diffusively due to the Brownian motion. According to Equation 2.85 the average time required for two spheres of radius a , which are initially in contact, to diffuse apart by a distance of a is

$$t = \frac{a^2}{2D},$$

with $D = k_B T / (6\pi a \eta_0)$, which yields the relaxation time

$$t = 3\pi a^3 \eta_0 / (k_B T). \quad (2.94)$$

With $a = 2\mu m$ and $\eta_0 = 100cp$, the estimated relaxation time is about 7 hours at room temperature. Therefore, this disassembling process is slow, and the viscosity reduction lasts for several hours, long enough for many practical applications.

After all the aggregated particles have disintegrated, the suspension returns to the rheological state prior to field treatment, and the viscosity returns to its original value.

This process is repeatable. A reapplication of the field pulse reduces the viscosity again.

2.8 Experiment Verification and Applications with MR Fluid

The above theory has been verified by experiments in our group (Tao & Xu, 2006). Nanoparticles of iron with diameter 35 to 40 *nm* were mixed in pump oil as a dilute magnetorheological (MR) fluid. The iron particles in MR fluid were well dispersed by coating the particle surface with a small amount of surfactant. The volume fraction ϕ of the iron particles in the MR fluid was 9%. To keep the MR fluid at a constant temperature, the container was placed in a thermal bath with temperature set at 23.5°C. Initially the viscosity of the a MR fluid was 880 *cp* , as measured by our Brookfield DV-II+ pro rotational viscometer at 10 rotations per minute (*rpm*). It is well known that the viscosity of MR fluid increases in a constant magnetic field, and the stronger the magnetic field, the higher the effective viscosity (Kormann, Laun & Richter, 1996). However, after applying a magnetic field pulse of 0.15 Tesla (T) for 5 minutes, the viscosity of the MR fluid decreased to 496 *cp* , as a result of the suspended nano particles aggregating to form larger ones. The result is shown in Figure 2.12.

After the field was turned off, the viscosity gradually went up. After 240 minutes, it increased to 780 *cp* , which was still lower than its initial value of 880 *cp* . The viscosity was back to the original value after 12 hours with the suspended iron particles again dispersed in the base liquid.

This process is repeatable. If we reapply the magnetic field after the viscosity returns to its original value, it is reduced again.

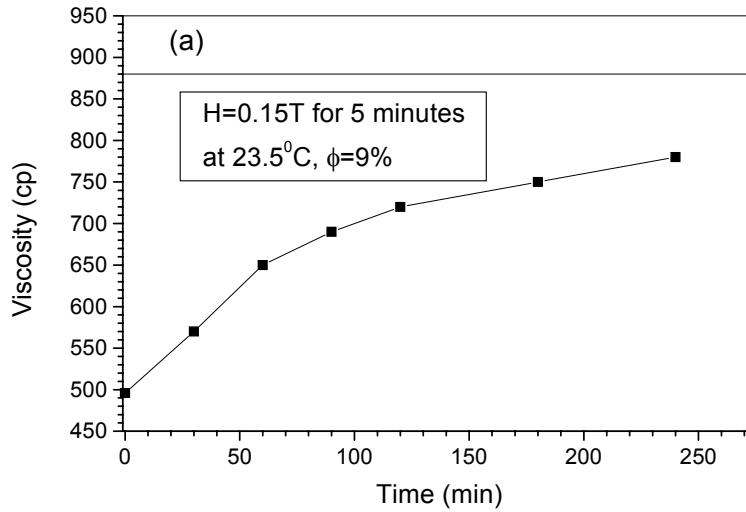


Figure 2.12. Magnetic Pulse Field Reduces Viscosity of MR Fluid. The viscosity of an MR fluid decreased to 496 *cp* from 880 *cp* after applying a magnetic field of 0.15 T for 5 minutes. It then gradually returned to the original rheological state.

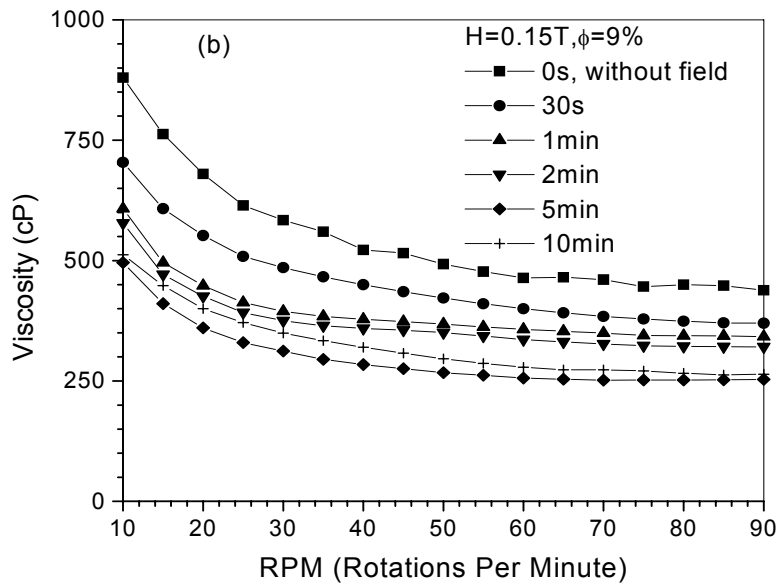


Figure 2.13. Viscosity Drop of MR Fluid Depends on Field Duration. For pulses ranging from 0 second to 10 minutes, a magnetic field pulse of 5 minutes produced the greatest viscosity reduction.

As shown in shown in Figure 2.13, the viscosity drop after application of a magnetic field pulse depended on the pulse duration. A magnetic field pulse of 5 minutes seemed to produce the maximum viscosity reduction for measurement with rotational speed from 10 to 90 *rpm* . The aggregated magnetic particle clusters were shaped like ellipsoids (Promislow & Gast, 1996). A more dilute MR fluid of $\phi = 1\%$ was used to measure the size of clusters with different field strength. After a pulse of 0.38 T for 1 s , the suspended particles with diameters of 30 to 40 *nm* aggregated in to clusters with average size of 9.9 μm ; A pulse of 10 s led to clusters with size 15.4 μm . The result is shown in Figure 2.14. The increase of the average cluster size leads to the viscosity reduction.

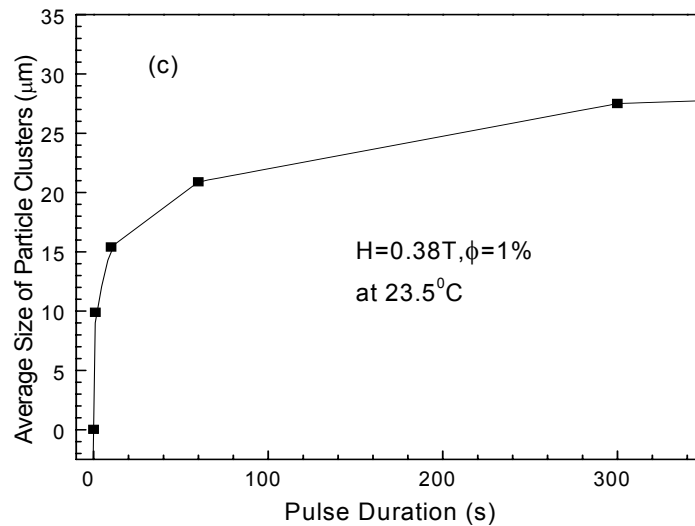


Figure 2.14. Average Size of Particle Clusters vs. Magnetic Field Duration. With increase of the magnetic field pulse duration, the average size of aggregated particles gets larger.

We note that According to Equation 2.92, H_c is 0.07T and 0.21T for $\phi = 9\%$ and $\phi = 1\%$ respectively. Our applied fields here were slightly stronger than these estimates. A picture of an aggregated particle cluster is shown in Figure 2.15.

We have applied this method for viscosity reduction to crude oil (Tao & Xu, 2006). It was found that the paraffin-base crude oil, the viscosity could be reduced by a pulsed magnetic field whereas for asphalt-base crude oil, the viscosity could be reduced by a pulsed electric field. These experimental results indicate that this method of reducing the viscosity, is very promising for a broad range of applications.

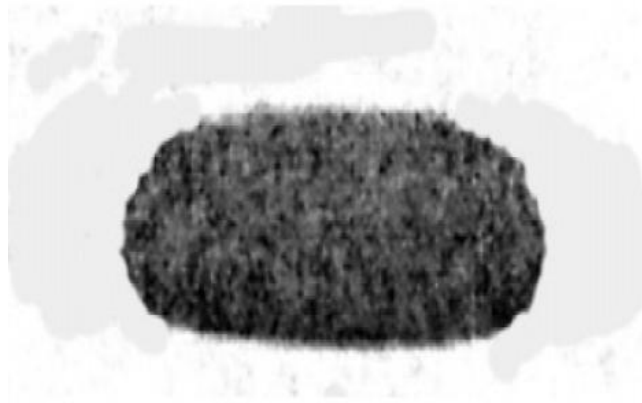


Figure 2.15. Picture of Aggregated Particle Cluster. Its longitudinal diameter is about $25 \mu m$.

CHAPTER 3
EQUIPMENT AND DEVICES USED IN FIELD TREATMENT AND DIESEL
AUTOMIZATION AND SPRAY EXPERIMENT

3.1 Electric Magnet and Power Supply

The electromagnet in the experiment was made by Magnion and driven by a power supply with model No. Magnion HS-1365B. The power supply and magnet are shown in Figure 3.1.



Figure 3.1. Magnion Power Supply and Magnet. The model number of the power supply is HS-1365B (left). The system is able to provide a uniform magnetic field of 1.5 Tesla between the poles.

The power supply supplies a stable current to the magnet of up to 50 Amperes, producing a uniform magnetic field of up to 1.5 Tesla, or 13000 Gauss. The relationship between the current supplied by the power supply and the magnetic field strength between the two poles of the magnet is shown in Figure 3.2.

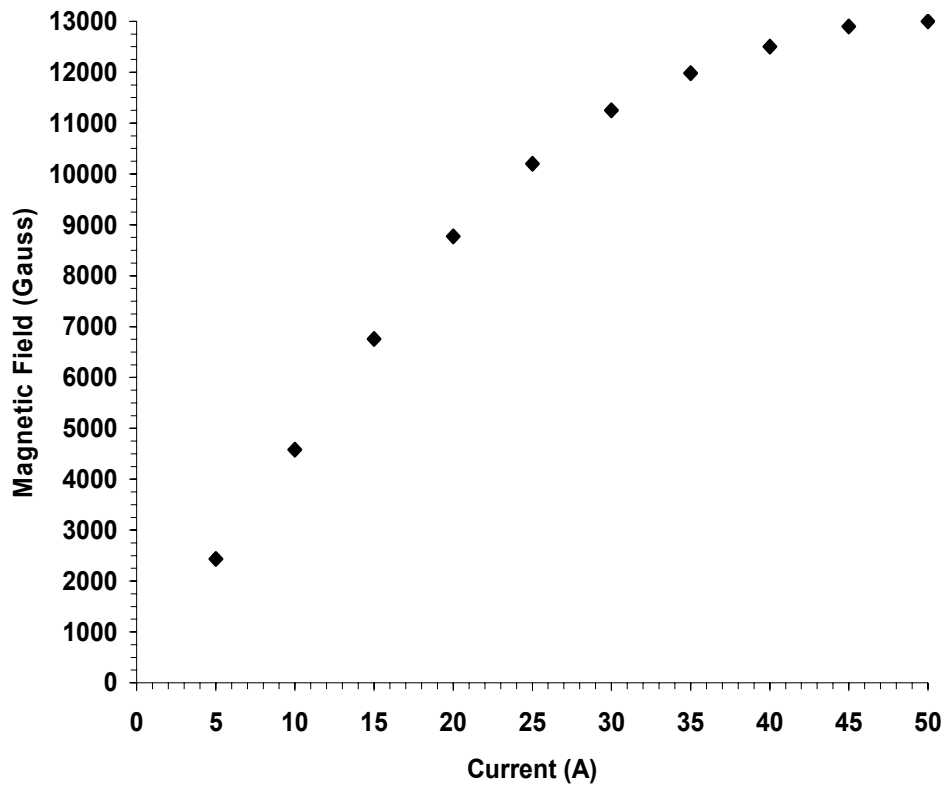


Figure 3.2. Magnetic Field Strength vs. Power Supply Current.

Figure 3.2 indicates that the magnetic field strength is not proportional to the current of the power supply. As the current approaches 50 A, the field strength becomes saturated.

3.2 High Voltage Power Supply

An EMCO 4200 high voltage power supply and An Ultravolt 40A-12-P4 were used in the electric field treatment. Their input was provided by a Harrison 6210B DC Power Supply which supplies 0 to 24 Volts. These devices are shown in Figure 3.3.

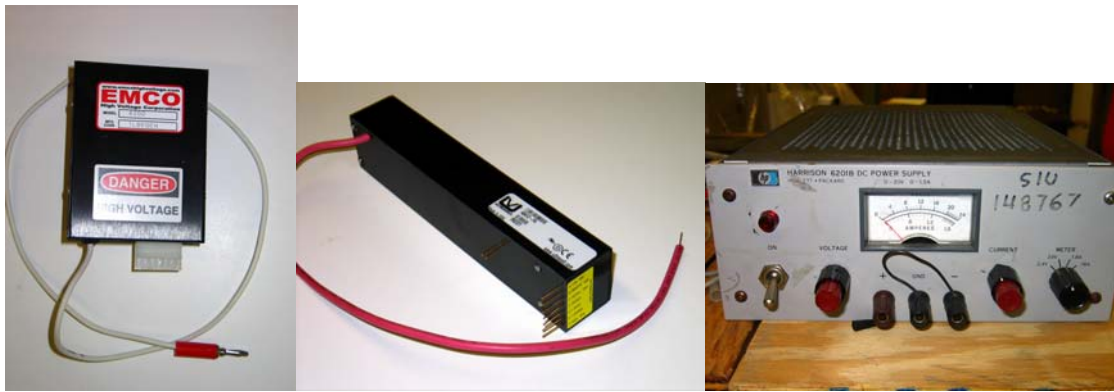


Figure 3.3. High Voltage Power Supplies and DC Power Input. The EMCO 4200 model (left) provides up to 20,000 V, whereas the Ultravolt 40A-12-P4 (middle) has a maximum output of 40,000 V. The Harrison 6210B DC Power Supply (right) serves as their input.

The EMCO 4200 (left in Figure 3.3) uses a 24 V DC input and provide voltages 0 V to 20,000 V with a control voltage from 0 V to 10 V. The output current is less than 0.5 mA, and the maximum output power is 10 W. The Ultravolt 40A-12-P4 (middle in Figure 3.3) uses a 12 V DC input and has an output range from 0 V to 40,000 V, with control voltage from 0 V to 5 V. Its output current is less than 0.1 mA, and the maximum output power is 4 W. The Harrison 6210B DC Power Supply provides an output voltage from 0 V to 24 V, which is a sufficient input for the high voltage power supplies.

3.3 Rotational Viscometers

3.3.1 Brookfield Rotational Viscometer

The Brookfield DV-III and DV-II+ Pro Viscometers are the most important equipment used in our viscosity measurements. They are rotational rheometers. The spindle of the rheometer is mounted on a calibrated spring. The spring is deflected by the viscous drag force during the rotation of spindle, and the deflection is measured with a rotary transducer. The measurement range of the rheometer is affected by several factors, including the size and shape of the spindle, the rotational speed of the spindle, the container of the sample, and the full scale torque of the calibrated spring (Brookfield Engineering Laboratories [BEL], n.d.). The viscometer are shown in Figure 3.4. The main specifications for DV-III and DV-II+ Pro are listed in Table 3.1.



Figure 3.4. Rotational Viscometers. Brookfield DV-III (left) and DV-II+ Pro (right) Viscometers.

Table 3.1 Main Specifications for DV-III and DV-II+ Pro

Specifications	DV-III	DV-II+ Pro
Minimum Speed (RPM)	0.01	0.01
Maximum Speed (RPM)	250	200
Viscosity Repeatability	±0.2%	±0.2%

There are four spring sets with different torques provided by Brookfield available for rotational viscometers. They are listed in Table 3.2.

Table 3.2 Spring Sets with Different Torques Provided by Brookfield

Model	Torque ($\times 10^{-3}$ N·m)
LV	0.0673
RV	0.7187
HA	1.4374
HB	5.7496

The measurement of viscosity in different ranges is usually carried out by changing the spindle and adjusting the rotational speed. The torque of the spring plays an important role in the measurement. Spring with low torque is suitable for measurements of samples with low viscosity, whereas the spring with high torque is needed for the

samples with high viscosity. Our DV-III model uses the HA spring set, and the LV set is installed in our DV-II+ Pro viscometer.

3.3.2 Brookfield HA/HB and LV Spindle Sets

There are three sets of spindles available in our lab for measurement of viscosities. There are five spindles in the HA/HB series and four spindles in the LV series. The third one is a ULA spindle with container and water jacket, which is used with a water bath to control the sample temperature. The HA/HB-2 to HA/HB-5, LV-2 and LV-3 spindles are disc spindles whereas the LV-1 and LV-4 spindles are cylindrical. The ULA spindle and container form a coaxial cylinder. The HA/HB and LV spindles are shown in Figure 3.5. The ULA spindle and its container with water jacket are shown in Figure 3.6.



Figure 3.5. Spindles Used in Viscosity Measurements I. Spindles in the left picture are HA/HB-1 to HA/HB-5, and spindles in the right picture are LV-1 to LV-4.



Figure 3.6. Spindles Used in Viscosity Measurements II. The ULA Spindle is shown in the left picture, and its container and water jacket are shown on the right.

The formulas for derivation of the viscosity measured by the cylindrical spindles are (Brookfield Engineering Laboratories [BEL], n.d.)

$$\dot{\gamma} = \frac{2\omega R_c^2 R_s^2}{x^2 (R_c^2 - R_s^2)}, \quad (3.1)$$

$$\tau = \frac{M}{2\pi R_s^2 L}, \quad (3.2)$$

$$\eta = \frac{\tau}{\dot{\gamma}}, \quad (3.3)$$

where $\dot{\gamma}$ is the shear rate in unit of s^{-1} , ω is the angular velocity of spindle in rad/s ; R_c and R_s are the radius of the container and the spindle in cm , respectively; x is the radius at which the shear rate is calculated in cm ; τ is the shear stress in units of $dyne/cm^2$, or $10^{-1} N/m^2$; M is the torque input from the viscometer in units of $dyne \cdot cm$, or $10^{-7} N \cdot m$; L is the effective length of the spindle in cm .

The formulas for the viscosity calculation with the coaxial cylinders are similar to those for cylindrical spindles except that Equation 3.1 is replaced by

$$\dot{\gamma} = \frac{2\omega R_s^2}{R_c^2 - R_s^2}, \quad (3.4)$$

where ω , R_c and R_s are defined as in Equation 3.1.

3.3.3 Spindle Range Coefficient

With the different spring sets and spindles, a broad range of viscosities can be measured. The Spindle Range Coefficient (*SRC*) is a coefficient employed by Brookfield for the evaluation of the viscosity range for a spring set and spindle. The maximum viscosity that a viscometer can measure with given spring set, spindle model and rotational speed is given by

$$\eta_{\max} = \frac{SRC}{\omega}, \quad (3.5)$$

where η_{\max} is the maximum viscosity in *cP*, or *mPa·s*, *SRC* is the Spindle Range Coefficient measured by the manufacturer, and ω is angular or rotational velocity of the spindle in units of revolutions per minute (*rpm*).

The *SRC* s for different spring sets and spindle models are shown in Table 3.3. The maximum viscosity that a spring set and a spindle operated at certain rotational speed is determined by Equation 3.5 and Table 3.3. For instance, the DV-III viscometer in our lab has an HA spring set installed. If an HA/HB-2 spindle is mounted on the viscometer and operated at a angular velocity of 50 *rpm*, according to Table 3.3 the *SRC* is 80,000, and from Equation 3.5, it follows that the maximum viscosity that can be measured is 1600 *cP*.

Table 3.3 Spindle Range Coefficient (*SRC*) for Different Brookfield Spring Sets and Spindle Models

Spindle	SRC (LV Spring)	SRC (HA Spring)
HA/HB-1	937	20,000
HA/HB-2	3,750	80,000
HA/HB-3	9,375	200,000
HA/HB-4	18,750	400,000
HA/HB-5	37,500	800,000
LV-1	6,000	128,000
LV-2	30,000	640,000
LV-3	120,000	2,560,000
LV-4	600,000	12,800,000
ULA	600	12,800

3.4 Capillary Viscometers

The capillary viscometer is a U-shaped glass tube. In measuring viscosity, it is held vertically in a controlled temperature bath. In one arm of the U-shape glass there is a vertical section with a precise narrow bore, and the time for the liquid to pass through it is measured. This is the reason this kind of viscometer is known as the capillary viscometer. There are two bulbs, one above the capillary and another bulb located lower down in the other arm. In measuring viscosity, the liquid sample is drawn into the upper bulb by a vacuum. After that it is allowed to flow down through the capillary into the lower bulb. There are two marks, one above and one below the upper bulb, which serve as indicators. Figure 3.7 shows a capillary viscometer and a close-up of the bulb with marks blow and above.

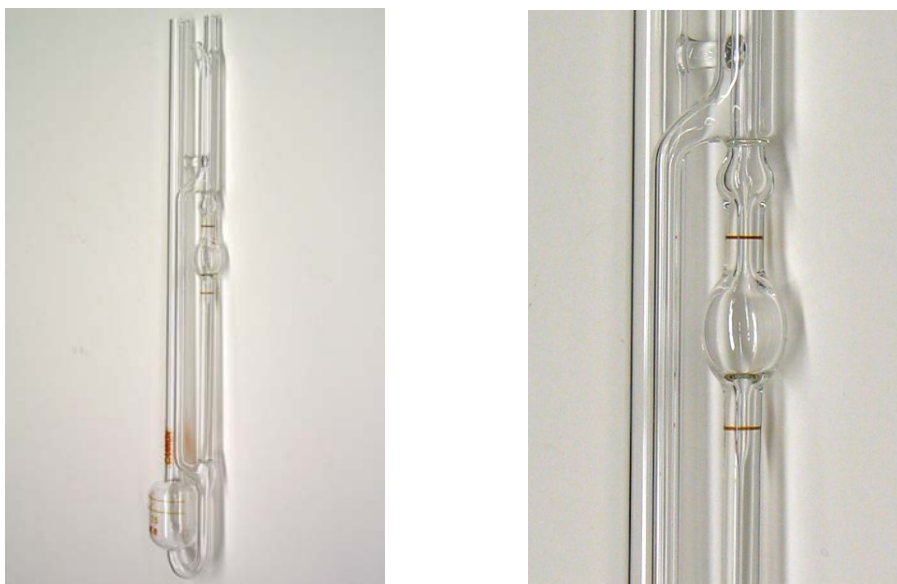


Figure 3.7. Capillary Viscometer. The capillary viscometer (left) is a U-shaped glass tube with a bulb on each arm. The marks above and below the bulb (right) serve as indicators for measuring the flow time of the liquid inside, from which the viscosity of the liquid can be determined.

The time needed for the level of the liquid sample to pass between the two marks is proportional to the kinematic viscosity. The kinematic viscosity is calculated by multiplying the time for the liquid to pass between the two marks by the viscometer constant of the capillary viscometer, or

$$\nu = Ct, \quad (3.6)$$

where ν is the kinematic viscosity, C is the viscometer constant and t is the flowing time.

The kinematic viscosity has the unit Centistokes (cSt), as mentioned in Chapter 2. The viscometer constant for a particular capillary viscometer is determined using a standard fluid of known viscosity flowing through the capillary. The viscometer constant has the unit cSt/s .

There are Ubbelohde series capillary viscometers manufactured by Cannon available in our lab. Table 3.4 lists the kinematic viscosity range of these viscometers.

The model number of the viscometer is related to the size of its capillary. A larger model number indicates a larger capillary diameter. For a fluid with a given viscosity, the smaller the model number, the longer the measurement time. If a fluid with very high viscosity is measured by a viscometer with small model number, the time for the measurement will be extremely long. Therefore, in viscosity measurement a capillary viscometer is selected so that the measurement time is between 250 and 1000 seconds.

Kinematic viscosities are based on the primary viscosity standard, water, at 20 °C. The internationally accepted dynamic viscosity for water is 1.0016 $mPa \cdot s$ or cP , whereas the kinematic viscosity of water is 1.0034 cSt .

Table 3.4 Kinematic Viscosity Range of Cannon Capillary Viscometers

Model No.	Viscometer Constant (cSt/s)	Viscosity Range (cSt)
25	0.002	0.5 to 2
50	0.004	0.8 to 4
75	0.008	1.6 to 8
100	0.015	3 to 15
150	0.035	7 to 35
200	0.1	20 to 100
300	0.25	50 to 250
350	0.5	100 to 500
400	1.2	240 to 1200
450	2.5	500 to 2500
500	8	1,600 to 8000
600	20	4,000 to 20,000
650	45	9,000 to 45,000
700	100	20,000 to 100,000

3.5 Devices Used in Electric Field Treatment

Most of the devices used in the field treatment for both crude oil and diesel fuel were designed in our lab. In some designs the field is applied to a stationary sample, whereas in others the field is applied while sample is flowing. In some devices the field is parallel to the flow direction of the sample, whereas in other devices the field is perpendicular to the flow direction.

3.5.1 Solid Plate Capacitor Sample Treatment Container

There are two kinds of containers in this category. One consists of a piece of insulating ring, usually made of Teflon or plastic, with a brass bottom plate and a lid made of brass. A container of this type is shown in Figure 3.8.

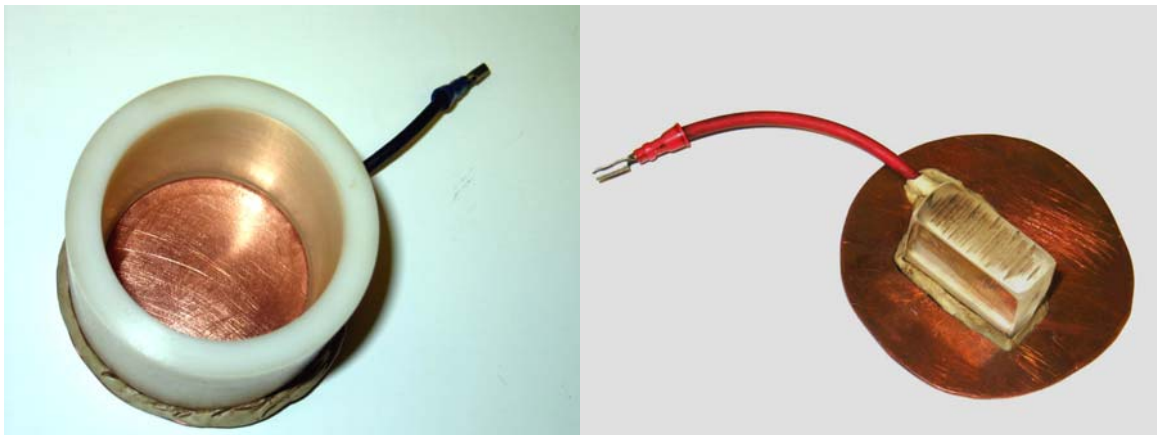


Figure 3.8. Solid Plate Capacitor Sample Treatment Container I. Container (left) is made of a piece of Teflon ring and a brass bottom plate. The lid (right) is a brass plate.

Both the bottom plate and the lid have a lead that is connected to the high voltage power supply during application of the electric field. The field strength on the sample is calculated by dividing the voltage difference of the two plates by the distance between the plates. For instance, if the voltage difference is 32,000 V and the distance is 5 cm, the electric field strength is 640 V/mm. This container is used in electric field application for both crude oil and diesel fuel. After the treatment, the viscosity of sample is immediately measured with the rotational viscometer.

Another kind of solid plate capacitor sample treatment container was used for the treatment of diesel fuel. It consists of a flat insulating box, usually made of plastic, with two capacitor plates attached to the inside walls. There are three holes in the box, two on top and one at bottom. One of the top holes is the sample filling opening and the other is venthole. The bottom hole is used to mount thin tubes through which sample is flowing. A device of this kind is shown in Figure 3.9.

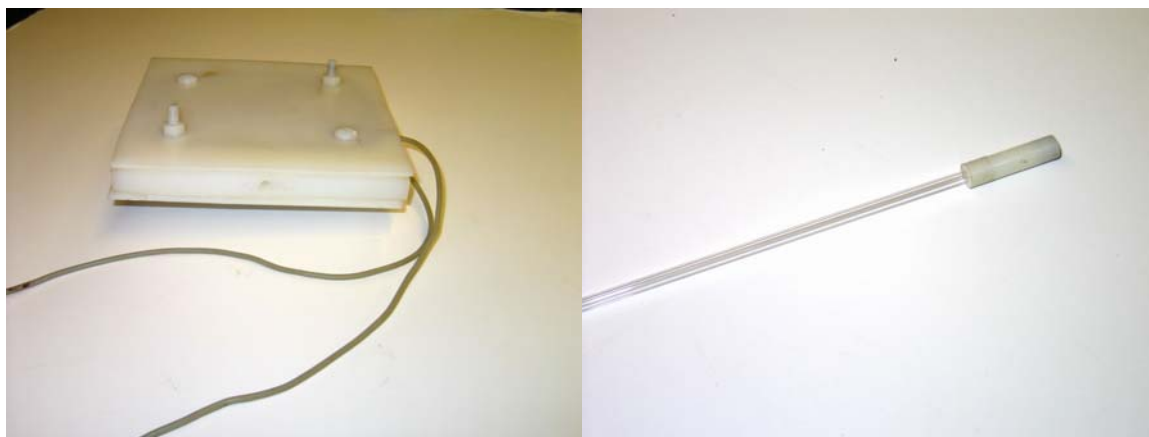


Figure 3.9. Solid Plate Capacitor Sample Treatment Container II. Container (left) has two capacitor plates connected to the two leads. The bottom hole is for mounting a thin tube with adapter (right).

After field treatment inside the container, the sample liquid flows through the thin tube to a collector underneath. The flow time is compared to that before field treatment. Again the field strength is calculated by dividing the voltage difference between the plates by the distance between the plates. The treatment time is controlled by a switch.

There is another design for applying the field is applied while the sample is flowing continuously through the capacitor container. In this design, the field is constant and the time exposure is controlled by the flow rate. The direction of field is perpendicular to the direction of flow.

3.5.2 Mesh Capacitor Sample Treatment Container and Tube

Instead of using two solid plates, two mesh plates are used in this device. The sample flows through the meshes where the field is applied. Thus, the field direction is parallel or antiparallel to the direction of the flow. Theoretically, this design favors the flow more than the design with the field direction perpendicular to the flow direction.

One device of this type is illustrated in Figure 3.10. Two mesh grids are inside a guard ring made of insulating material, separated by a spacer. Leads are soldered to the mesh grids for connection to a high voltage power supply. The bottom plate is assembled to the guard ring with an O-ring. There is a hole in the bottom plate for installation of an adapter which is connected to a glass tube with a small inner diameter. After the field application, the fluid sample flows through the device, and the flow time is measured and compared to that before the field treatment.



Figure 3.10. Mesh Capacitor Sample Treatment Container. The left picture shows a device of this kind with a glass tube and an adapter mounted on the bottom plate. The top mesh with lead soldered on it is shown in the right picture.

In another design the field is applied to the sample while it is flowing through meshes. Two or more mesh grids are placed inside a glass tube, with a certain distance in between. One of these devices is shown in Figure 3.11.

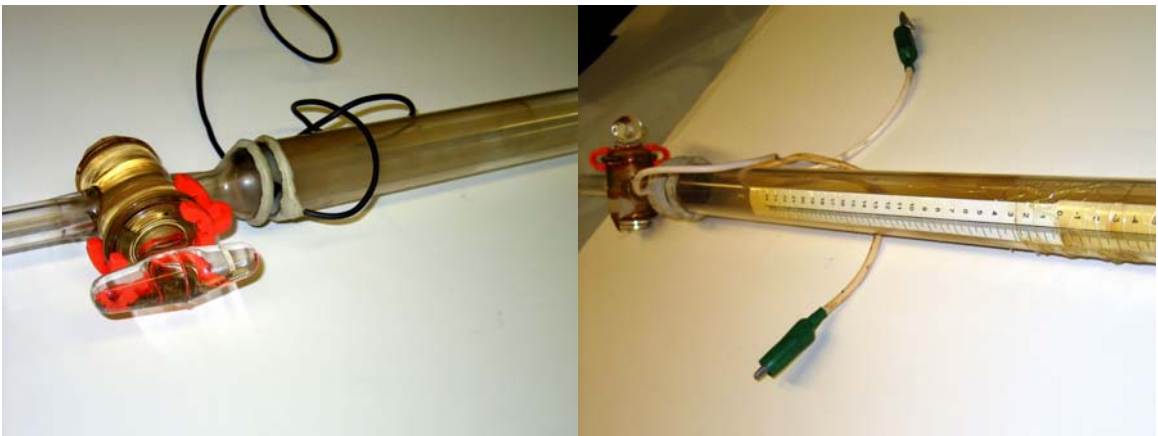


Figure 3.11. Mesh Capacitor Sample Treatment Tube. The left picture shows a sample treatment tube with two meshes. The right picture shows a tube with three meshes. A valve is used to control the flow rate.

In the field treatment, the tube is filled with sample to a certain level. The field is on while the sample is flowing through the meshes. The flow rate of the sample is controlled by the glass valve at bottom of the tube, thus determining the treatment time of the sample. Additional sample is filled from the top during the treatment to ensure that the level of the sample is always the same and the flow rate is constant. The treatment time is determined by the flow rate τ , the diameter D of the tube, and the distance h between the two meshes according to

$$\tau = \frac{\pi D^2 h}{4q} . \quad (3.7)$$

For instance, for a flow rate of 5 ml/s, a tube diameter 4 cm, and a distance between the two meshes of 2 cm, the treatment time is 7.85 s.

3.6 Devices Used in Fuel Treatment, Atomization, and Spray Experiment

3.6.1 Field Application Device

The device used for field application in the fuel atomization and spray experiments is similar in principle to those for continuous treatment mentioned in last section. In addition, it has openings on both ends with female threads for connecting to brass tubes. This device and its schematic are shown in Figure 3.12. There are two meshes inside the device, which are perpendicular to the direction of flow. Two leads are soldered to the meshes for connection to a high voltage power supply. The whole device is sealed and able to withstand pressure.

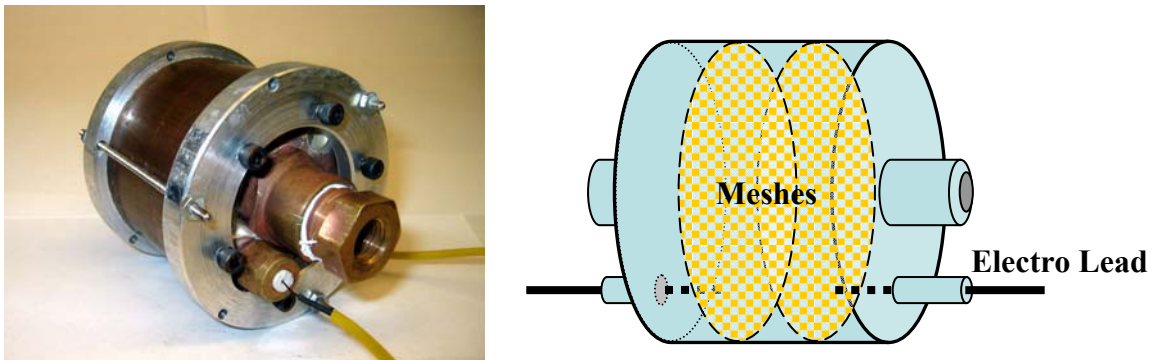


Figure 3.12. Field Treatment Device and Its Schematic. On the left is a picture of the field treatment device and on the right is a schematic of the device showing its inner structure.

3.6.2 Pressurized Fuel Container and Fuel Injector

The fuel container is connected to the field application device and supplies pressurized fuel. The container and its schematic are shown in Figure 3.13. Pressurized air coming from the nitrogen gas cylinder pushes the fuel in the container out through the fuel pipe into the field treatment device. The other end of the field treatment device is connected to a fuel injector in an adapter, shown in Figure 3.14. The fuel injector responds to an electric pulse and jets out the fuel. The duration of the ejection is controlled by the duration of the electric pulse. A home made circuit composed of a 555 Timer and a RC circuit is used as the controller. With different combinations of a resistor and a capacitor, the duration of the pulse can be varied.

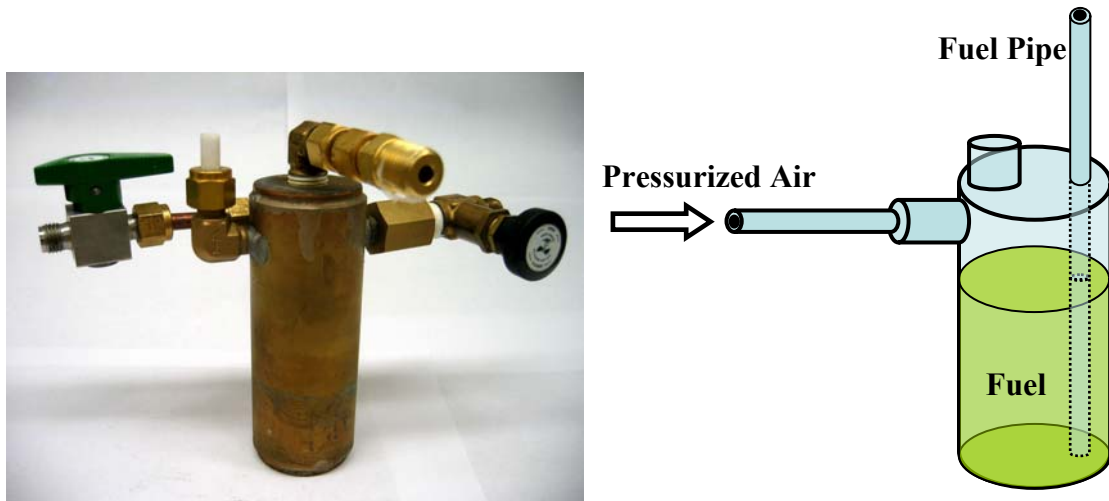


Figure 3.13. Pressurized Fuel Container and the Schematic. On the left is a picture of the field treatment device, and on the right is a schematic of the device showing its inner structure.



Figure 3.14. Fuel Injector and the Adapter. In the right picture it can be seen that the fuel injector has two control taps, which respond to an electric pulse and open the injector for the duration of the pulse.

3.7 Other Devices

Many other devices were used in our experiments, including glass tubes and needles, a micro balance, beakers, containers with water jackets, experimental stands, etc. Some glass tubes and needles with different sizes and openings, which are mounted on the sample treatment container are shown in Figure 3.15.

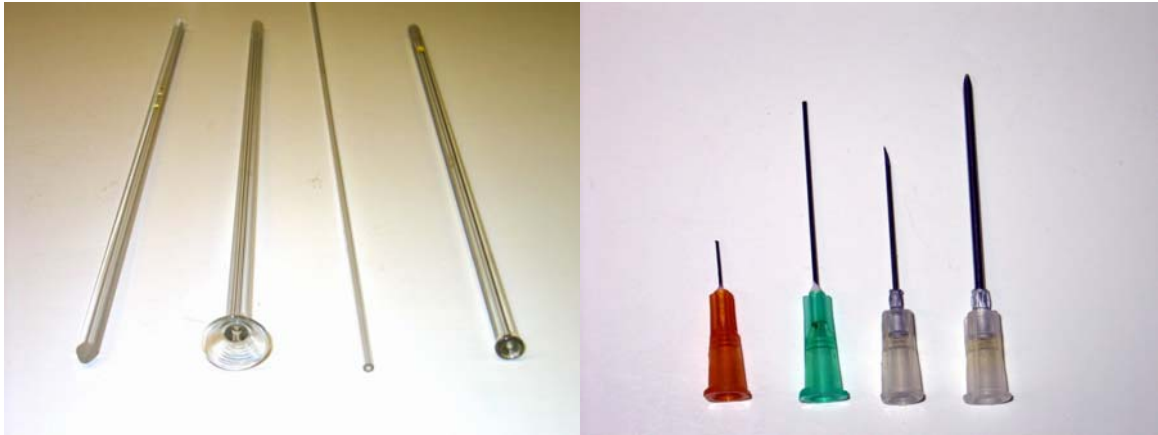


Figure 3.15. Glass Tubes and Needles. Glass tubes with different inner diameters and openings are shown on the left. Needles of different size are shown on the right.

The micro balance is used to accurately determine the mass of samples. It is also used in diesel viscosity measurement to take real time increments of the sample. It is shown in Figure 3.16. In the viscosity measurement with the capillary viscometer, the viscometer must be in a vertical position. A home made experimental stand ensures the vertical position of viscometer. This is shown in Figure 3.17. A container with water jacket keeps the sample at a constant temperature. This is shown in Figure 3.18.



Figure 3.16. Micro Balance.



Figure 3.17. Experimental Stand with Capillary Viscometer.



Figure 3.18. Container with Water Jacket.

CHAPTER 4

REDUCING THE VISCOSITY OF CRUDE OIL

4.1 Crude Oils

Crude oil or petroleum is a naturally occurring, flammable liquid found in rock formations in the Earth consisting of a complex mixture of hydrocarbons of various molecular weights, plus other organic compounds (“Petroleum”, n.d.). From field to field crude oils can be very different in appearance and viscosity. They vary in color, odor, and other properties. However, hydrocarbons are the main components contained in all crude oils, including alkanes, cycloalkanes and various aromatic hydrocarbons. Besides majority of hydrocarbons, crude oils also contain other organic compounds with nitrogen, oxygen and sulfur, and trace amounts of metals such as iron, nickel, copper and vanadium.

4.1.1 Composition of Crude Oils

Although the exact molecular composition of crude oil varies widely, the proportion of chemical elements is limited to a very narrow range (Speight, 1999). This is shown in Table 4.1.

Four different types of hydrocarbon molecules appear in crude oil. They are paraffins, naphthenes, aromatics, and asphaltics (Hyne, 2001). Their relative percentages are shown in Table 4.2.

Table 4.1 Composition of Elements in Crude Oil by Weight Percentage

Element	Percent range (%)
Carbon	83 to 87
Hydrogen	10 to 14
Nitrogen	0.1 to 2
Oxygen	0.1 to 1.5
Sulfur	0.5 to 6
Metals	less than 1000 ppm

Table 4.2 Weight Percentage of Four Types of Hydrocarbon Molecules in Crude Oil

Hydrocarbon	Average Percentage (%)	Percent range (%)
Paraffins	30	15 to 60
Naphthens	49	30 to 60
Aromatics	15	3 to 30
Asphaltics	6	remainder

Crudes are roughly classified into two groups from the view point of petroleum refining (Bacon & Hamor, 1916), according to the nature of the hydrocarbons they contain. Paraffin-base crude oils contain no asphalt but do contain solid hydrocarbons of the paraffin series, which have molecular formula C_nH_{2n+2} , whereas asphalt-base crude oils are rich in asphalt and contain no solid paraffin. There is still another class of crude oils which is called mixed-base or paraffin-asphalt crude because they contain both paraffin and asphalt.

4.1.2 API Gravity of Crude Oils

The full name of API gravity is American Petroleum Institute Gravity (“API Gravity”, n.d.). It is a measure of the density of a petroleum liquid relative to water. It has the definition

$$API\ gravity = \frac{141.5}{S.G.} - 131.5, \quad (4.1)$$

where S.G. is the specific gravity of the crude oil at 15.6 °C, which does not have a unit. If crude oil has API gravity greater than 10, it is lighter than water, whereas crude oil with API gravity less than 10 is heavier than water and sinks. The API gravity frequently used to compare the relative densities of different crude oils. If one crude oil floats on another, it is less dense and has a greater API gravity. Since API gravity is calculated from pure numbers without units, API gravity also has no units. However, traditionally it is quoted in “degrees”. API gravity is graduated in degrees on hydrometer instruments and is defined so that most values would be between 10 ° and 70 ° API gravity degrees.

Usually, crude oils with API gravities between 40 ° and 45 ° have the highest prices. Molecular chains in crude oils above 45 ° degrees are shorter and less valuable to refineries. According to its API gravity, crude oil can be classified in three categories, namely, light, medium, or heavy. With API gravity higher than 31.1 °, a crude oil is a light crude oil. Medium oils have API gravity between 22.3 ° and 31.1 °. Heavy oil has an API gravity below 22.3 °. Crude oil with API gravity less than 10 ° is referred to as extra heavy oil or bitumen. Bitumen derived from the oil sand deposits in the Alberta, Canada area has an API gravity around 8 °.

4.2 Experiment Methods and Setup

4.2.1 *Experiment Methods*

Before being taken out from the barrel, each crude oil sample was stirred continuously for no less than 12 hours to ensure uniformity. Samples taken from barrels were immediately stored in plastic containers which are inert to crude oil. Just before removal from the storage container for an experiment, the container with crude oil sample was placed on a paint shaker for 20 to 30 minutes to ensure that the crude oil was well mixed. After removal from the container, extra time was allowed for the samples to cool to the temperature of the environment or the water bath. This is important in the viscosity measurements, because the temperature of the crude oil increases during the shaking, and the viscosity of crude oil is sensitive to temperature changes.

Crude oil is so inhomogeneous that even after such careful mixing, two samples taken from the same storage container may still have a discrepancy in their viscosities. This is especially evident in sticky crude oil with high viscosity. This increases the difficulty of the experiment. However, we only compare viscosity readings before and after field treatment for samples from the same treatment container. Comparison of viscosity readings from different samples can be misleading.

4.2.2 *Experiment Setup*

We used two kinds of experiment setup. One is the setup for static field treatment, where the sample in the field is not moving. The schematic for this setup is shown in Figure 4.1.

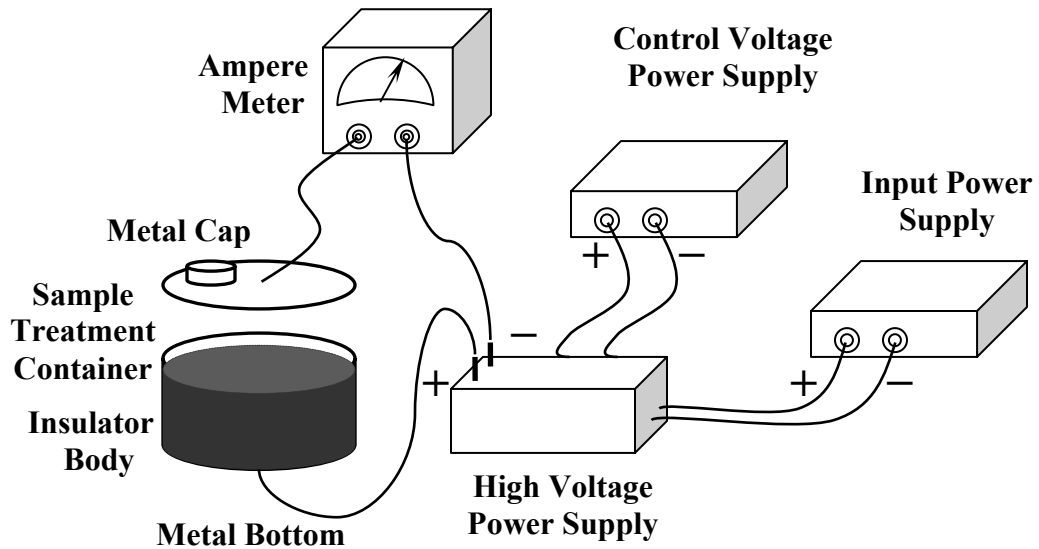


Figure 4.1. Schematic of Setup for Static Field Treatment. Sample is in treatment container which is connected to high voltage power supply through an ampere meter. High voltage power supply has a DC input power supply and a DC control voltage power supply.

In this setup, the sample is treated without flowing in a solid plate sample treatment container. The metal cap of the container is connected to the positive electrode of the high voltage power supply, and the metal bottom is connected to the negative electrode. The high voltage power supply has a DC input power supply and a DC control voltage power supply. The field application time is controlled by a switch. The sample fills the container to avoid an air gap between plates during the field treatment. If air bubbles are present, dielectric breakdown may occur when the voltage between the plates is high. The viscosity and temperature readings before and after field treatment are taken with the rotational viscometer and an appropriate spindle with sample in the container.

Another setup is usually used for continuous field treatment. In this setup, the mesh capacitor sample treatment tube is used in place of the treatment container. The schematic for the setup is shown in Figure 4.2.

The treatment tube is usually mounted on an experimental stand. The crude oil sample flows through the meshes while the field is on. Additional sample is added in order to keep the sample inside the tube at the same level during the experiment. The meshes are connected to the high voltage power supply through an ammeter, used to monitor the electric current through the crude oil. If there is no dielectric break down, the current should be in the μA range. The electric field is parallel to the direction of flow, with the top mesh connected to the positive electrode and the bottom mesh connected to the negative electrode. If the connections are inversed, then the field direction is opposite to the flow direction.

The sample is treated while it flows between the meshes. The flow speed is controlled by the flow rate control valve. As the field is always on during the experiment, the field treatment time is determined by the flow rate. The slower the flow rate, the longer the treatment time. The formula for the treatment time is Equation 3.7.

The viscosity of the crude oil before and after field treatment is measured with the rotational viscometer. Another way of comparing the viscosity before and after the field treatment is to record the time for same volume of sample flowing through the tube with field on and off.

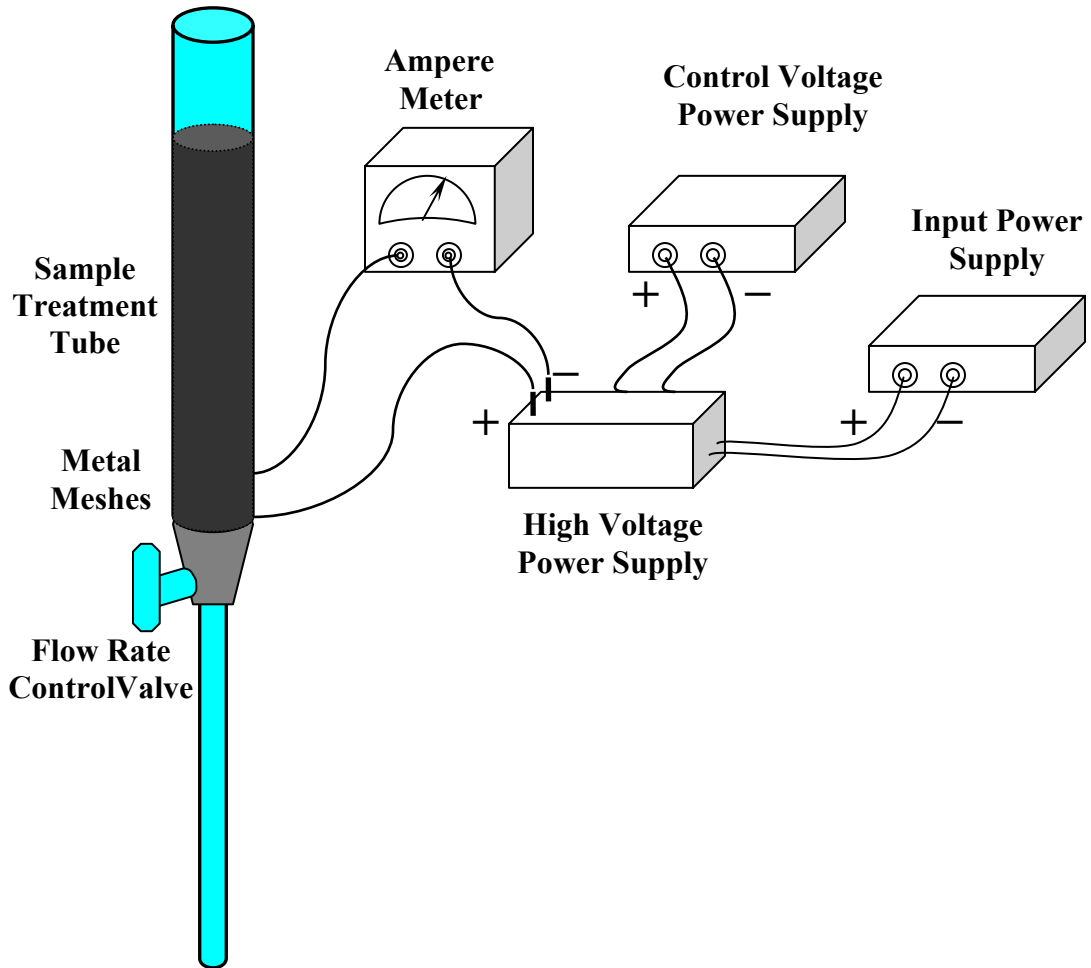


Figure 4.2. Schematic of Setup for Continuous Field Treatment. High voltage power supply is connected to meshes of the device through an ammeter. The field is either parallel or antiparallel to the direction of the flow.

4.3 Crude Oils from JGC

Three barrels of heavy crude oil, provided by the Japanese company JGC, were tested with our viscosity reduction method. According to the JGC labels, the API gravity was 11 °, 15 °, and 21 °, respectively. The crude oils were well mixed for overnight and stored in small containers made by materials inert to crude oil. Measurements of viscosity from the same sample still showed some variation. The viscosity results for the API 11 °, 15 °, and 21 ° crude oil samples at room temperature of 21 °C are shown in Table 4.3.

Table 4.3 Viscosities of JGC Crude Oils with API Gravity of 11 °, 15 ° and 21 ° at 21 °C

Crude Oils	Viscosity Range (<i>cP</i>)
API 11°	96,000 to 108,000
API 15°	390,000 to 423,000
API 21°	390 to 430

The API 21 ° crude oil is liquid-like, whereas the API 11 ° and API 15 ° crude oils are like gels. Although API 15 ° crude oil has a moderately higher API degree than API 11 ° crude oil, its viscosity is much higher. The API 15 ° crude oil can not be poured out without squeezing the storage container. Crude oil samples with API gravity of 15 ° and 21 ° are shown in Figure 4.3.

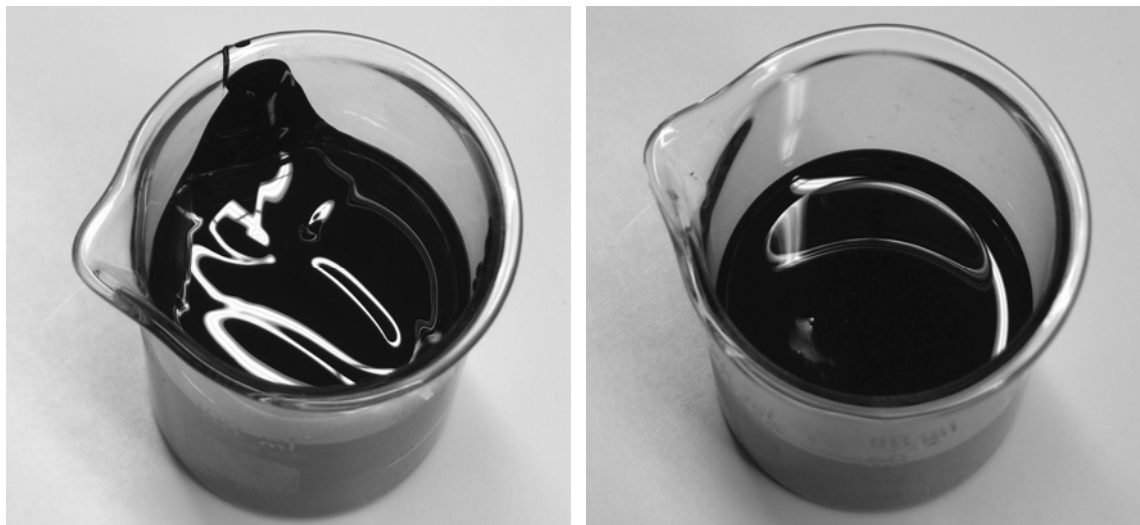


Figure 4.3. JGC Crude Oil Samples. The left picture shows crude oil sample with API gravity of 15° , which has a viscosity around $400,000\text{ cP}$. The right picture is crude oil sample with API gravity of 21° , which has a viscosity around 400 cP .

As shown in Figure 4.3, the API 15° crude oil has a very high viscosity around $400,000\text{ cP}$, and therefore is very sticky. This crude oil sample had an uneven surface in the beaker for quite a long time before finally becoming level. The sample stuck so tightly to the beaker that it stayed in the beaker for several minutes even when it was turned upside down. The API 21° has more liquid-like behavior because of its much-lower viscosity, which is around 400 cP . When the sample was poured into a beaker, a level surface was formed immediately.

Electric fields of 120 V/mm to 960 V/mm were applied to the crude oils with durations from 5 s to 1440 s . The temperatures of the crude oil samples were measured immediately before and after field treatment were measured to ensure viscosity decrease of the sample was not caused by an increase of the sample temperature. The temperatures before and after treatment were usually unchanged, with changes of 0.1°C or 0.2°C in

some cases. This is important to check, since heavy crude oils are strongly affected by temperature.

4.3.1 Temperature Effects of JGC Crude Oils

The viscosities of all three crude oil samples are strongly temperature dependent. At 20.3 °C, the crude oil sample of API 21 ° had an average viscosity of 540 *cP*. At 25.5 °C, its viscosity decreased to 402 *cP*. The viscosity reduction rate in this region was about 4.91% per degree Celsius. At 20.7 °C, the crude oil sample of API 11 ° had an average viscosity of 101,547 *cP*. Its viscosity decreased to 65,289 *cP* as the temperature increased to 25.2 °C, for viscosity reduction rate of about 7.94% per degree Celsius. For the crude oil sample of API 15 °, the viscosity was 488,320 *cP* at 20.6 °C. At 25.9 °C, its viscosity decreased to 320,000 *cP*. The viscosity reduction rate in this region was about 6.50% per degree Celsius.

4.3.2 Repeatability of Measurement

To ensure that the viscosity reduction of the crude oils was entirely due to the electric field, from the same experimental procedures were followed for each sample, apart from the field. These measurements were compared with the measurements taken before going through procedures. Our results showed that the difference between viscosities before and after the procedures was within 0.5 percent. A sample result is shown in Figure 4.4.

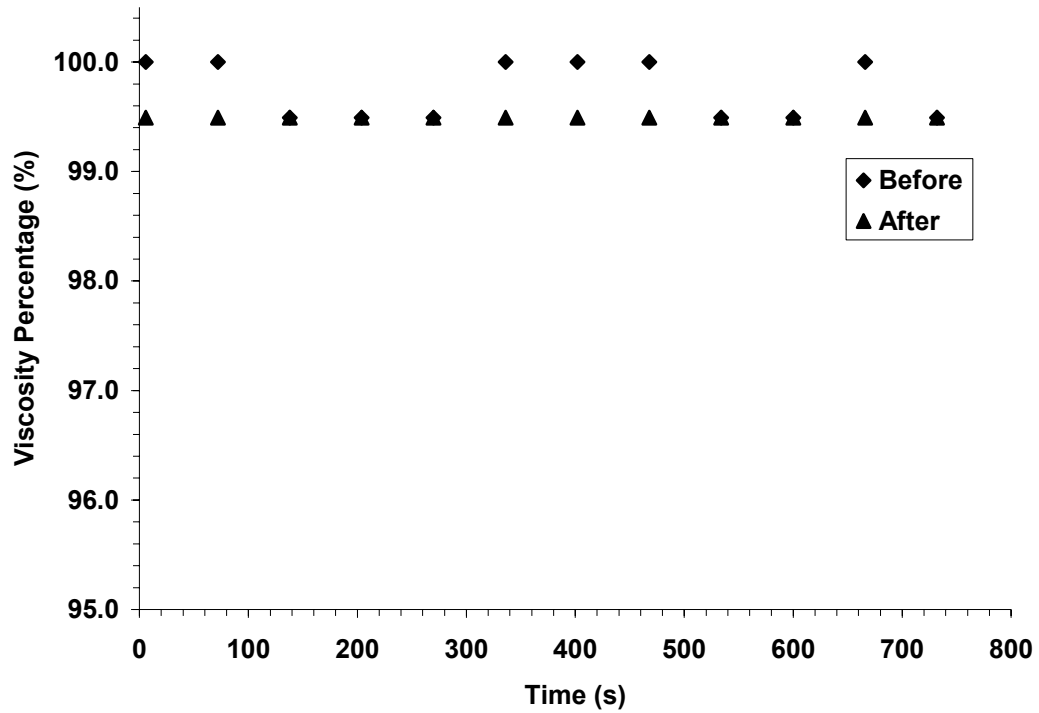


Figure 4.4. Reproducibility of Measurement. Difference between viscosities of API 11 ° crude oil sample measured before and after going through the whole procedure without applying the field was within 0.2%.

The viscosities of the same API 11 ° crude oil sample were measured twice with the Brookfield DV-III rotational viscometer with the HA spring set and LV4 spindle at 30 RPM. The temperature was 21.9 °C. As shown in Figure 4.4, the average initial viscosity was 83,888 *cP*. After going through the whole procedure without applying field, the average viscosity dropped to 83,680 *cP*. Thus, the difference of the viscosity before and after the procedures was only 0.2 percent.

4.3.3 Reducing Viscosity of JGC Crude Oils by Electric Field

The electric field strong affects on the viscosity of the API 11 ° crude oil sample. For API 11 ° crude oil, a moderate electric field reduces its viscosity significantly. Figure 4.5 shows the viscosities of JGC API 11 ° crude oil before and after treatment with an electric field of 280 V/mm for 45 seconds.

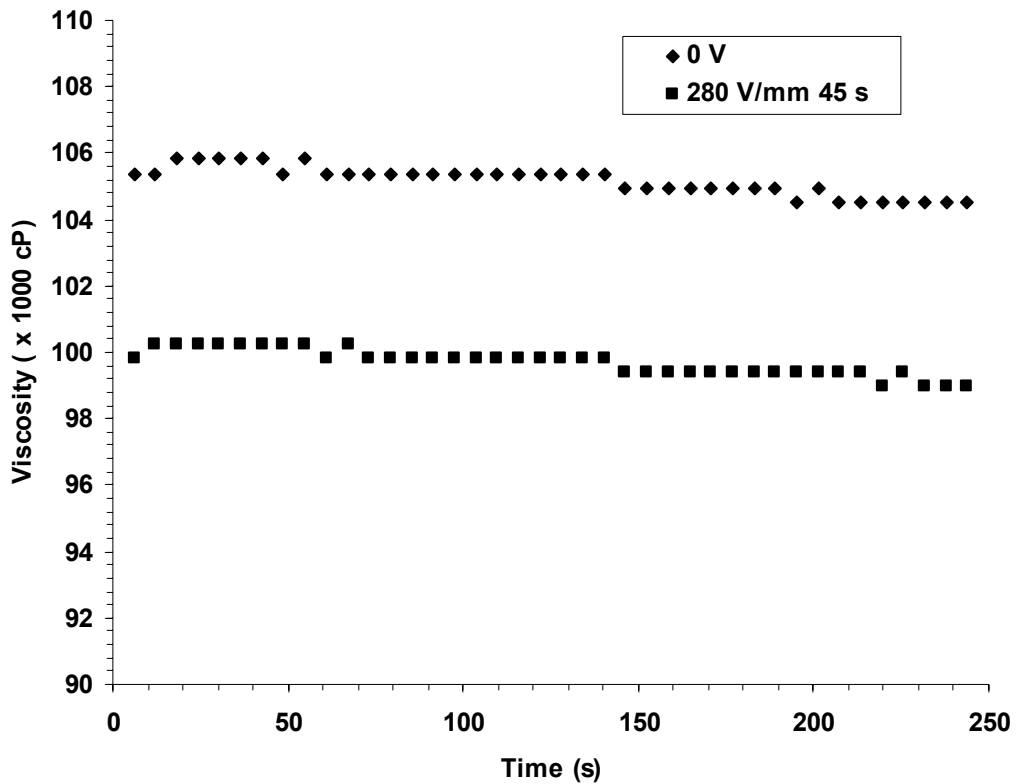


Figure 4.5. Viscosity Reduction after Field Treatment. API 11 ° crude oil was treated by field of 280 V/mm for 45s. After the field application, the viscosity was dropped by 6% from 105,184 cP to 99,712 cP.

The viscosities were measured with the Brookfield DV-III rotational viscometer with HA spring set and LV4 spindle at 30 RPM. The temperature was 21.6 °C. The

viscosity of the API 11 ° JGC crude oil sample was 105,184 *cP* initially. After a 45 s field treatment with strength of 280V/mm, it decreased to 99,712 *cP*, which is a 6% reduction.

An electric field of 280 V/mm was very effective in reducing the viscosity of the samples. Experiments with different duration time and with 280 V/mm were conducted. An average reduction of 6.7% ~ 7.1% was obtained with a field duration of 35s to 60s. The results are shown in Figure 4.6.

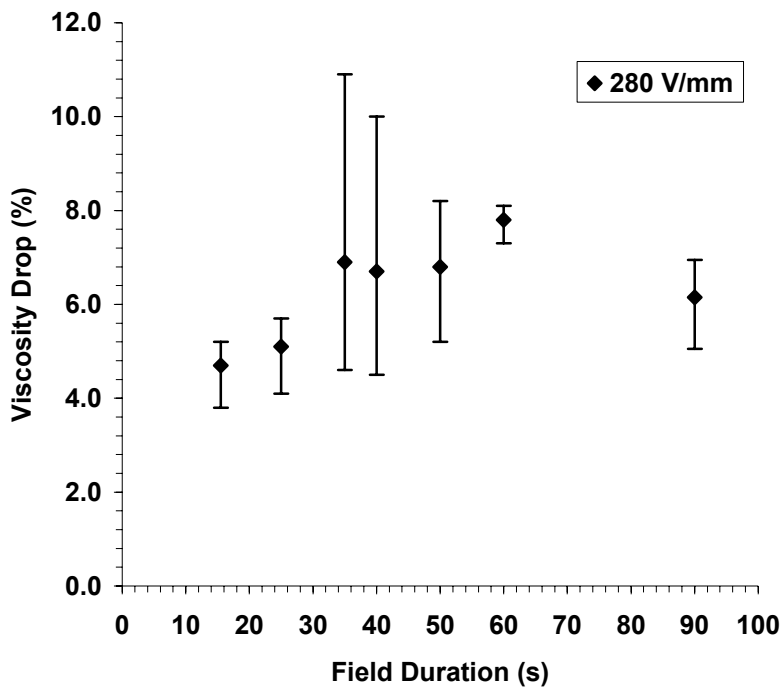


Figure 4.6. Viscosity Drop vs. Field Duration. JGC API 11 ° crude oils were treated by a field of 280 V/mm for different field duration. For short application times, the viscosity reduction was small. As the duration time increased further, an average viscosity reduction of 6.7 to 7.8 percent was achieved. As the field duration increased even further, the viscosity reduction drop became small again.

The plot indicates that when field duration is short, the viscosity reduction is not very big. As the duration increases, the viscosity drop is large. As duration increased further, the reduction became smaller again. As shown in the graph, even with the same field strength and duration, the reduction of viscosity varies from trial to trial. This can be explained by the non-uniform distribution of suspended particles in the crude oil sample, even after careful mixing with machines for a long time. As discussed in Chapter 2, a different particle distributions in the liquid suspension leads to a different response to the electric field.

With the field treatment duration time fixed at 60 s, several different field strengths were tried. The results are shown in Figure 4.7.

Initially, the average viscosity drop becomes larger as the field strength increases from 185 V/mm to 280 V/mm. As the field strength increases further, the viscosity drop becomes smaller. This can be explained by the theory presented in Chapter 2. As the field strength increases, the particles suspended in the crude oil move faster. The size of particle clusters increases with the increase of the field strength. As the particle clusters become larger, the effective viscosity of the crude oil sample drops. However, when the field strength increases further, the particle clusters become even larger, with some of them aggregating into chains and jamming the flow. Therefore, the reduction of the viscosity first increases and then decreases with increasing field strength. If the field strength and time increases even further, the viscosity of crude oil may increase.

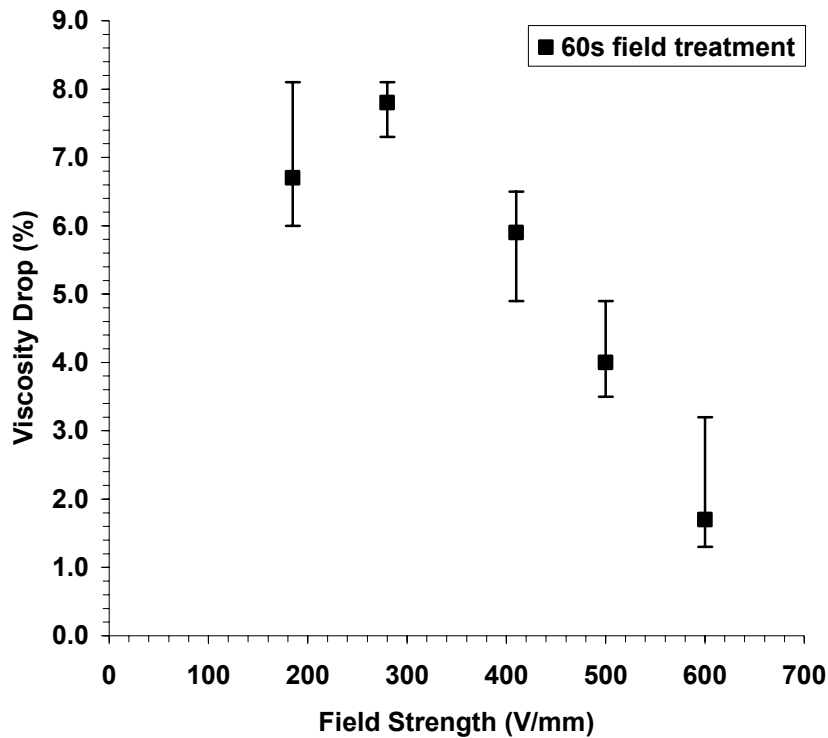


Figure 4.7. Viscosity Drop vs. Field Strength. JGC crude oil samples with API 11^o were treated for 60 s field duration with different field strength. As the field increases, the viscosity drop first increases and then decreases.

After appropriate field treatment, the viscosity decreases as a result of the aggregation of suspended particles into clusters. When the field is off, the particle clusters tend to separate due to Brownian motion. This is the relaxation of the system, as we discussed in section 2.7.5. The relaxation time of system is typically in hours. One of the results is shown in Figure 4.8. Initially the viscosity was 96,427 *cP*. After field treatment with 451 V/mm for 45 s, it immediately dropped to 92,160 *cP*, then dropped further to 90,880 *cP*, a 5.8% reduction. After that, it gradually increased back to its initial value in 1.5 hours.

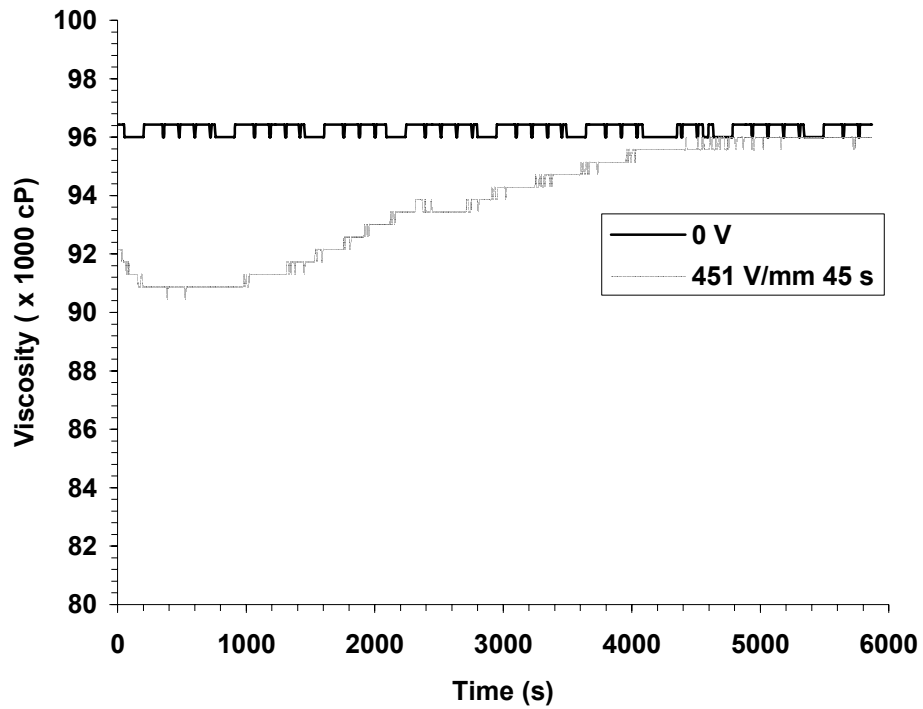


Figure 4.8. System Relaxation after Field Treatment. JGC Crude Oil with API 11^o were treated with 451 V/mm for 45 s. Viscosity was dropped by 5.8% after field treatment and gradually increased back to its original value in 1.5 hours.

A significant of viscosity reduction for API 11^o crude oils was found for a wide range of field strength, from 180 V/mm to 560 V/mm for different field durations. Some results for different field strength are listed in Table 4.4.

From the table one sees that with increasing of field strength, the largest viscosity reduction is generally achieved with shorter field duration. The electric current measured by the ammeter in these experiments was negligible, generally less than 1 μA .

The electric field also reduces the viscosity of API 21^o crude oil. Some of the our results are shown in Table 4.5.

Table 4.4 Viscosity Reduction for JGC API 11 ° Crude Oil by Electric Field

Field Strength (V/mm)	Treatment Time (s)	Original Viscosity (cP)	Viscosity after Treatment (cP)	Viscosity Drop (%)	Temperature Change (°C)
187	60	108,373	106,240	6.7	0
200	40	97,707	87,893	10.0	0
274	40.5	102,400	92,160	10.0	0
277	35.5	105,386	93,867	10.9	0
414	50.5	111,360	104,107	8.6	0
524	31	104,960	97,280	7.8	0
560	3	102,827	96,427	6.2	0

Table 4.5 Viscosity Reduction for JGC API 21 ° Crude Oil by Electric Field

Field Strength (V/mm)	Treatment Time (s)	Original Viscosity (cP)	Viscosity after Treatment (cP)	Viscosity Drop (%)	Temperature Change (°C)
652	600	469	429	8.6	0.2
648	1200	483	413	14.5	1.6
800	18.8	423	280	34.0	3.3

In connection with the third result in table 4.5, we note that in this experiment the crude oil was treated continuously in a mesh capacitor sample treatment tube, as illustrated in Figure 4.2. When the crude oil sample passed between the two metallic meshes in the tube, it was exposed to the electric field on the meshes. In this experiment, the crude oil took about 18.8 seconds to pass between the two meshes. The current monitored by the ammeter was moderate, 25 μ A. However, the temperature increased from 21.7 °C to 25 °C. Of the total viscosity reduction of 34%, part of the reduction was contributed by the 3.3 °C temperature increase and the rest was caused by the electric field effect. As described in 4.3.1, the viscosity reduction due to a temperature change for

API 21 ° is about 4.91% per degree Celsius. Therefore, the temperature change contributed a viscosity reduction of 16%, whereas the remaining 18% reduction was caused by the electric field.

The viscosity reduction of the API 15 ° JCG crude oil with our current high voltage power supply is not as striking as for the other two JCG crude oils. The electric field does affect on the viscosity of API 15 ° crude oil sample. However, the optimal combination of field strength and duration time was difficult to determine. One possible reason is that the field strength available in our lab was not strong enough aggregate the suspended particles due to the extremely high viscous drag force. The viscosity of API 15 ° crude oil is around 400,000 *cP*. Some of our results are listed in Table 4.6.

Table 4.6 Viscosity Reduction of JGC API 15 ° Crude Oil by Electric Field

Field Strength (V/mm)	Treatment Time (s)	Original Viscosity (cP)	Viscosity after Treatment (cP)	Viscosity Drop (%)	Temperature Change (°C)
872	60	387,840	373,760	3.7	0.1
872	120	375,040	363,520	3.1	0.1
864	240	428,800	407,040	5.1	0

4.3.4 Reducing Viscosity of JGC Crude Oils by Magnetic Field

Treatment with a magnetic field treatment was also found to reduce the viscosity of all three JGC crude oils. However the reduction is moderate. Table 4.7 summarizes some of our results.

Table 4.7 Viscosity Reduction of JGC Crude Oils by Magnetic Field Treatment

API	Field Strength (Gauss)	Treatment Time (s)	Original Viscosity (cP)	Viscosity after Treatment (cP)	Viscosity Drop (%)	Temperature Change (°C)
11 °	13,000	10	104,960	98,133	6.5	0
11 °	2,500	0.33	73,387	72,533	2.0	0
11 °	2,500	0.97	76,373	75,947	1.0	0
11 °	13,000	10	96,853	93,440	3.5	0
15 °	5,550	1.46	439,040	426,240	3.0	0
15 °	6,000	2.29	486,400	463,360	4.7	0
15 °	13,000	20	458,240	451,840	1.4	0
21 °	13,000	40	650	630	3.1	0
21 °	13,000	35	623	613	1.6	0
21 °	12,900	50	650	627	2.6	0

4.4 Crude Oils from Shell

Two kinds of crude oil supplied by Shell Oil from Maya and Quo Iboe were tested in our lab. The storage containers for the crude oil from Maya and Quo Iboe are shown in Figure 4.9.



Figure 4.9. Shell Crude Oils from Maya and Quo Iboe. Container crude oil from Maya is shown in the left picture and container with crude oil from Quo Iboe is shown in the right picture.

The crude oil from Maya is much thicker than the crude oil from Quo Iboe. At 24 °C, the Maya oil has a viscosity around 300 *cP* whereas the viscosity of Quo Iboe oil is around 30 *cP*. This difference is reflected in their containers. In Figure 4.9, one sees that the container for Maya oil has an additional cap, which functions as a venthole when pouring the oil.

4.4.1 *Temperature Effects of Shell Crude Oils*

The viscosity of the Maya crude oil depends strongly on temperature. Its viscosity is 280 *cP* at 23.8 °C. However, when the temperature drops to 4 °C, the viscosity increases to around 1025 *cP*. These results were obtained with the Brookfield DVIII rotational viscometer, HA spring set and ULA adapter at 10 RPM.

If a crude oil is paraffin based, as the temperature decreases to a temperature called critical temperature, paraffins inside the oil crystallize into tiny particles, making the viscosity increase faster. This critical temperature is usually referred as the wax appearing temperature (WAT). As the temperature drops, the Maya crude oil does not show such a transition. Therefore, it can be inferred that the Maya crude oil is asphalt based. If it contains some paraffin, the amount must be small. The temperature dependence of the viscosity of the Maya crude oil is shown in Figure 4.10.

The viscosity of the Qua Iboe crude oil is very low. As shown in Figure 4.11, it is below 10 *cP* at room temperature. As the temperature drops to 4 °C, the viscosity increases to 70.4 *cP*, but is still low. In view of this, we concentrated on Maya crude oil.

4.4.2 *Reducing Viscosity of Maya Crude Oil by Electric Field*

Extensive tests were conducted for the Maya crude oil. Since the motivation for the research on Maya crude oil is to facilitate transportation of the crude oil through deepwater pipelines, where the temperature is as low as 4 °C, most of our experiments were conducted inside a large refrigerator, where the interior temperature was around 4 °C.

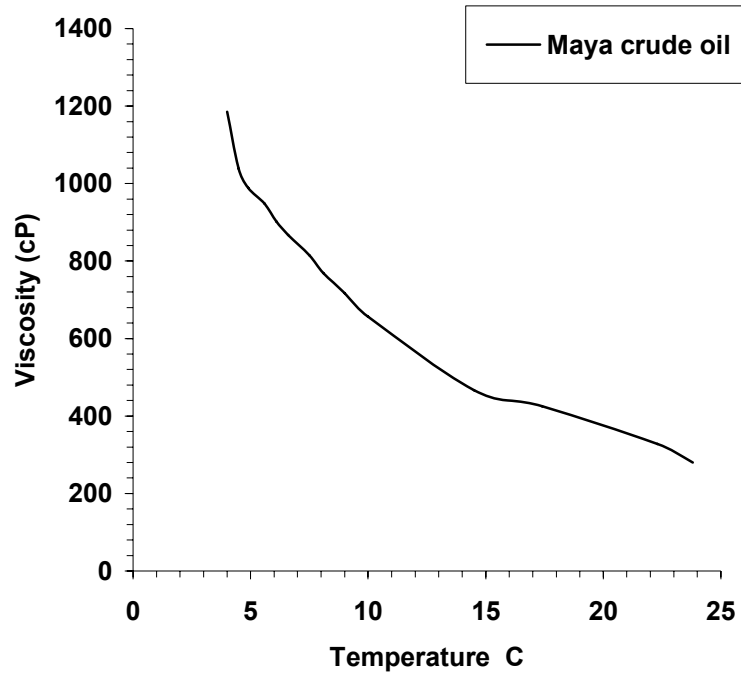


Figure 4.10. Temperature Effect of Maya Crude Oil.

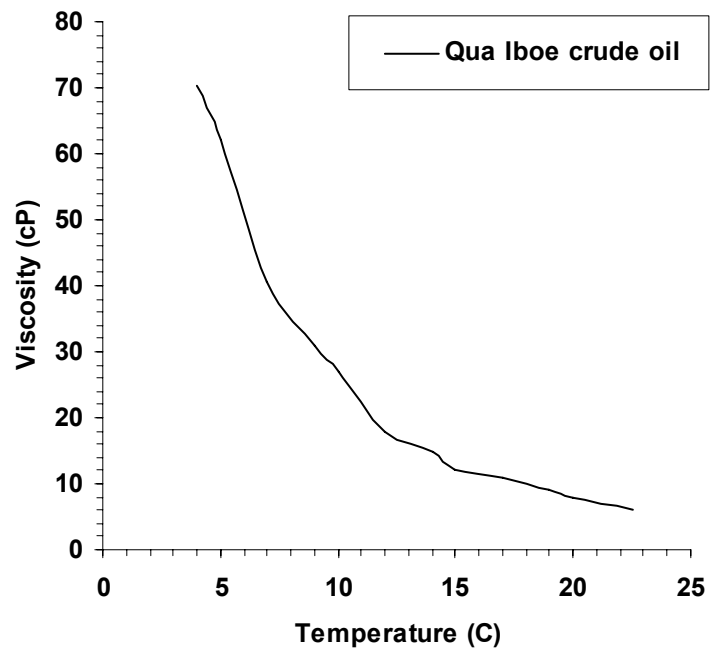


Figure 4.11. Temperature Effect of Qua Iboe Crude Oil.

As seen from Figure 4.1, the Maya crude oil has a viscosity around 1025 *cP* at 4 °C. Since the oil's density is about 0.93 g/cm³, the kinetic viscosity, according to equation 2.2, is about 1102.2 cSt. Two different methods were used to treat the sample. The first treatment setup is shown in Figure 4.1. In the experiment, we first used a rotational viscometer to measure a sample's viscosity, next applied an electric field to the sample for a couple of seconds, and finally remeasure the viscosity right after the treatment. The temperature change during the field treatment was also monitored. The power consumed during the experiment was determined from the voltage applied in the treatments and the current through the crude oil, which was measured by the ammeter.

The electric field strongly affects the viscosity of the Maya crude oil samples. Moderate to strong electric fields reduce its viscosity significantly. Table 4.8 summarizes our main results. Applying an electric field with strength around 800V/mm for 5 seconds reduces the viscosity of the crude oil by 20%. Not much energy is needed in the treatment. From our experiment, we estimate that the energy cost is about 0.01 kW-h/barrel.

Table 4.8 Viscosity Reduction of Shell Maya Crude Oil by Electric Field

Field Strength (<i>V/mm</i>)	Treatment Time (<i>s</i>)	Original Viscosity (<i>cP</i>)	Viscosity after Treatment (<i>cP</i>)	Viscosity Drop (%)	Temperature Change (°C)	Current (μA)	Power (<i>W</i>)
800	5.3	1,128	896	20.6	0.15	11	0.0495
800	5.2	1,232	960	22.1	0.15	12	0.0540
800	3.0	1,112	936	15.8	0.30	12	0.0540

In order to observe the flow rate for the crude oil after field treatment in real time, a continuous dripping flow device, shown in Figure 4.12, was designed.

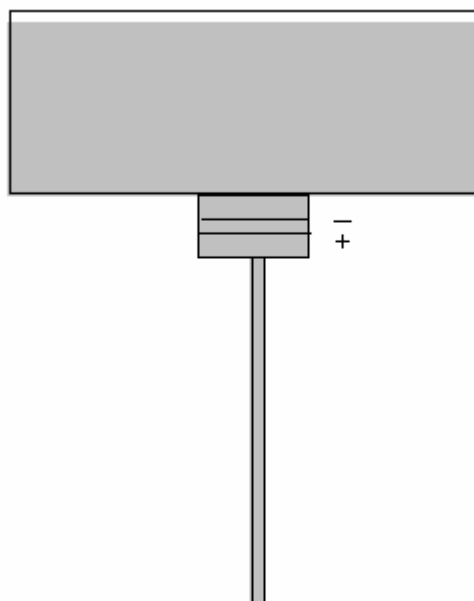


Figure 4.12. Dripping Flow Device Used in Continuous Field Treatment for Maya Crude Oil. This device allows observation of the flow rate before and after field treatment.

The setup is similar to Figure 4.2 except that the mesh capacitor sample treatment tube replaced by this device. The funnel-shaped device is similar to the mesh capacitor sample treatment tube except that it has a container with much larger diameter than the tube. Crude oil in this container flows vertically downward and passes through the mesh capacitor before it drips into a capillary tube. Two measurements were conducted in a single test. The first measurement of flow rate was taken with crude oil flowing down the capillary tube without application of the electric field. The second flow rate measurement was carried out with an electric field in the mesh capacitor. The lower the viscosity of the

crude oil, the higher the observed flow rate. In order to maintain a temperature around 4 °C, the whole setup was placed inside a large refrigerator.

The test results are very promising. One example had a flow rate of 0.44 g/s before the electric field treatment. After treatment with a field strength of 1,000 V/mm between the two meshes, the flow rate increased to 0.511 g/s, corresponding to a 16.1% increase in flow rate. The consumption of electric energy was very low. The voltage difference in the on mesh capacitor was about 4000 V, and the current reading was about 17 μ A. Multiplying these two values gives 68 mW for the electric power. This corresponds to 0.133 J/g or 0.0055 KW-h per barrel. At such low energy consumption, the electric field has little effect on the temperature.

The field strength and size of the capillary tube were not optimized in the experiment. Optimizing these quantities is expected to further increase the flow rate.

In addition to the experiments at 4 °C, we tested Maya crude oil at room temperature around 22 °C. The electric field was found to reduce the viscosity of the crude oil by 20%, even though the initial viscosity was only about 300 *cP*. Especially in the tests with our home-made dripping flow device at room temperature, significant increases in flow rate were found after field treatment. A capillary tube with smaller diameter was used in the tests at room temperature to compensate for the increased flow rate caused by higher temperature.

Promising results were also obtained at room temperature. In one experiment, the flow rate was 0.231 g/s before field treatment. After exposure to 800 V/mm, the flow rate rose to 0.277 g/s. This was an increase of 20% in flow rate. This corresponds to a

viscosity reduction of more than 30%. On the other hand, the power consumption was at very low, about 0.01KW-h per barrel.

4.4.3 Reducing Viscosity of Maya Crude Oil by Magnetic Field

Magnetic fields have a weak effect on the viscosity of Maya crude oil. Table 4.9 summarizes the test results. The results further confirm that Maya crude oil is asphalt based crude oil, with a negligible concentration of paraffin particles.

Table 4.9 Viscosity Reduction of Shell Maya Crude Oil by Magnetic Field

Field Strength (<i>V/mm</i>)	Treatment Time (<i>s</i>)	Original Viscosity (<i>cP</i>)	Viscosity after Treatment (<i>cP</i>)	Viscosity Drop (%)	Temperature Change (°C)
13,000	30	936	928	0.9	0.1
13,000	60	1168	1120	4.1	0.4
13,000	120	984	944	14.1	0.8

4.5 Electric Field Treatment Device and Cost Estimate for Commercial Pipeline

One of our electric field treatment devices designed for an oil pipeline is illustrated in Figure 4.13. The connections to the main pipeline are designed, as shown, in Figure 4.14 to facilitate periodic pigging process.

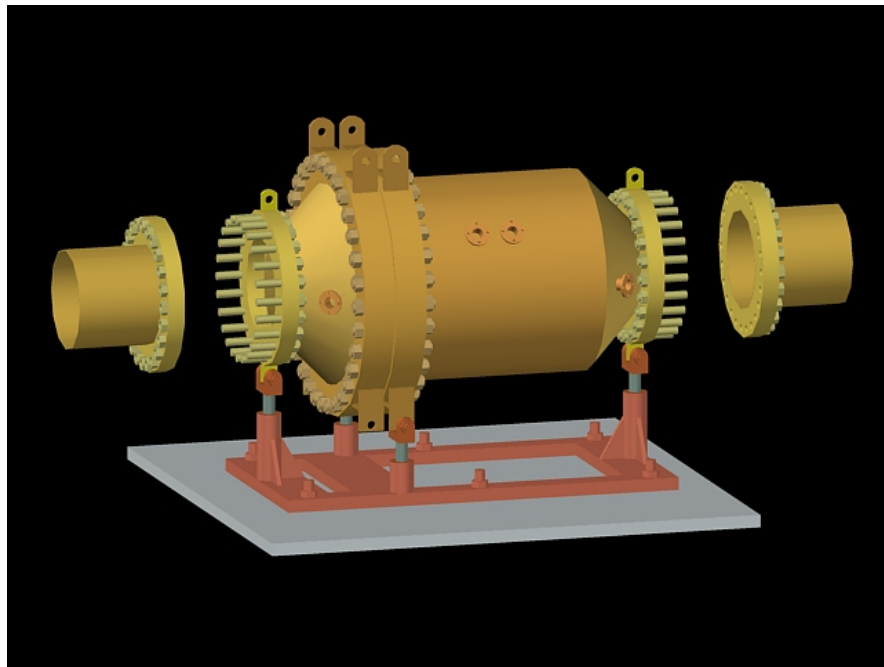


Figure 4.13 Design of Electric Field Treatment Device on Oil Transportation Pipelines.

Under normal operating conditions, the valve colored in green is in the off position, and crude oil flows through the two electric field treatment devices shown in brown. Filters are to be installed to remove potential unwanted materials from clogging the devices. During the pigging process, the green valve is open and the valves that control the passages to the electric devices are closed.

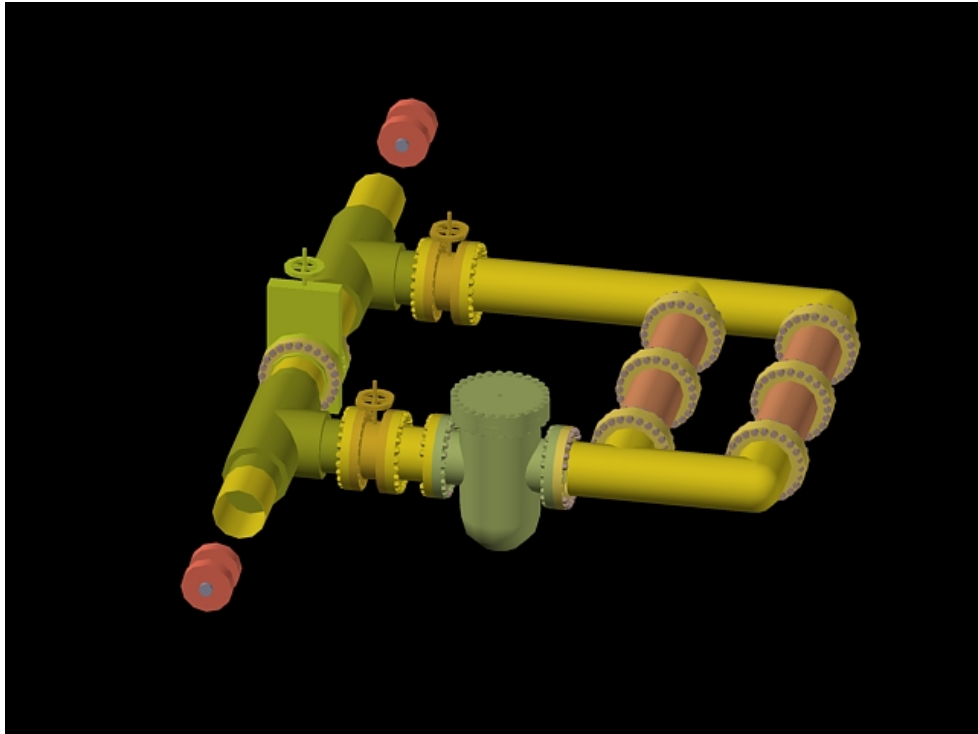


Figure 4.14 Design of Connections for Electric Field Treatment Devices to Oil Transportation Pipelines.

The operating cost for the field treatment device is low, since it operates at a low power level. We estimate the energy cost for the operation to be about 0.01 kW-h/barrel, almost negligible. In manufacturing the electric field treatment system, the power supplies and field treatment devices are the key components. Since the treatment systems run at low power level, the power supplies are not expensive. The fabrication cost for the mesh capacitors depends on the API degree of the crude oil. Once it is in mass production, the cost will come down. We expect to install one device every 20-30 kilometers along the pipeline.

CHAPTER 5
VISCOSITY REDUCTION OF FUELS FOR IMPROVED COMBUSTION
EFFICIENCY

5.1 Viscosity Reduction For Finer Droplets and Better Fuel Efficiency

5.1.1 Viscosity Reduction and Droplet Formation

Atomization is a process that transforms a bulk liquid fuel into small droplets (Lefebvre, 1989). In the process of pressure atomization (Graco, n.d.), the fuel is pressurized before being injected into the combustion chamber. When the injector is triggered, high pressure forces fluid through a small nozzle into combustion chamber. The fluid emerges as a stream at a high speed. The stream first breaks into fragments, then into drops, and ultimately into droplets as a result of the interaction between the stream and surrounding air. As a drop is deformed by aerodynamic pressures, the pressure distribution around it also changes. The drop splits, becoming smaller and smaller, until the external aerodynamic forces are balanced by the internal forces due to surface tension and viscosity. Under equilibrium conditions, the internal pressure p_i at any point on the droplet surface equals the sum of the external aerodynamic pressure p_a and the surface tension pressure p_σ ,

$$p_i = p_a + p_\sigma \tag{5.1}$$

The surface tension pressure for a spherical droplet is given by

$$p_{\sigma} = \frac{4\sigma}{D}, \quad (5.2)$$

where σ is the surface tension and D is the diameter of the droplet. It is clear from Equation 5.2 that the surface tension pressure increases as the droplet diameter decreases. A droplet is stable if a change in the air pressure at any point on its surface is compensated by a change in the surface tension, so the internal pressure stays constant. When pressurized fuel is sprayed out of a nozzle with high speed, the aerodynamic pressure on a drop is much larger than the surface tension pressure. Thus, the aerodynamic pressure deforms the drop and may lead to breakup of the drop into smaller drops. As a drop becomes smaller, the surface tension pressure on the drop increases. This process continues until the aerodynamic pressure and surface tension pressure are equal.

The role of viscosity in this process is to increase the breakup time since it opposes deformation of a drop. After the fuel is injected, the aerodynamic force on a drop decreases with time. Even if the aerodynamic force is initially large enough to break a drop, the drop may not split if viscosity lengthens the breakup time.

By reducing the viscosity of the fuel, smaller droplets can be obtained in a spray from injector, with other conditions remaining the same. Therefore, reducing the viscosity of the fuel can greatly improve the fuel atomization.

5.1.2 Fuel Efficiencies in Fast Combustion and Slow Combustion Processes

Figure 5.1 illustrates the four cycles of a typical four-stroke internal combustion engine. They are the intake stroke, compression stroke, combustion stroke, and exhaust stroke.

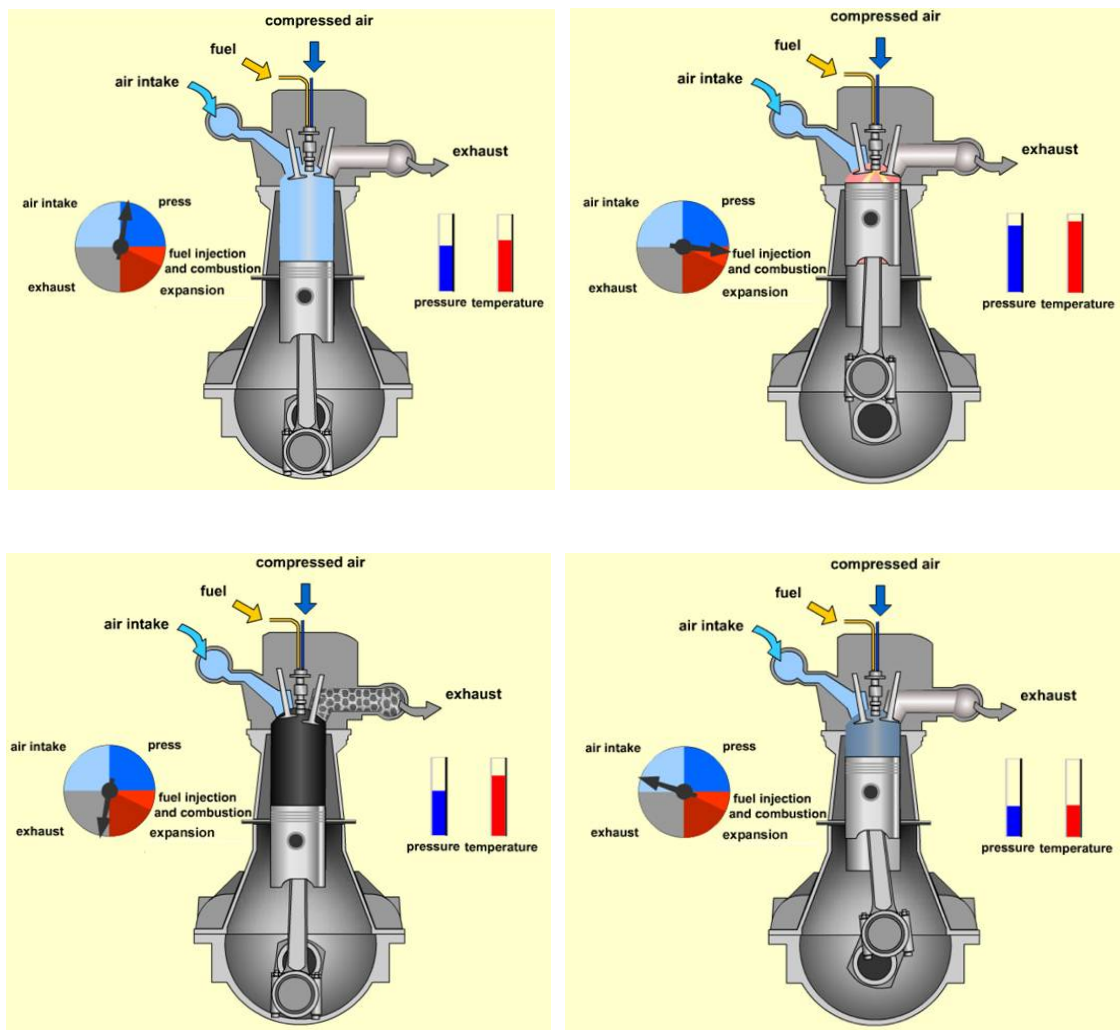


Figure 5.1. Four-stroke Engine Cycles of an Internal Combustion Engine. Upper left: intake stroke; Upper right: compression stroke; Lower left: combustion stroke; Lower right: exhaust stroke.

Two widely used idealized models of engine combustion process are the constant-volume combustion process and the constant-pressure combustion process (Heywood, 1988). In the constant-volume combustion process, the combustion is assumed to occur infinitely fast when the piston is at the top center (TC) crank position, immediately after injection of fuel into the chamber. In contrast, the constant-pressure combustion process is a slow combustion process. The Pressure-volume (P-V) diagrams for these two processes are shown in Figure 5.2.

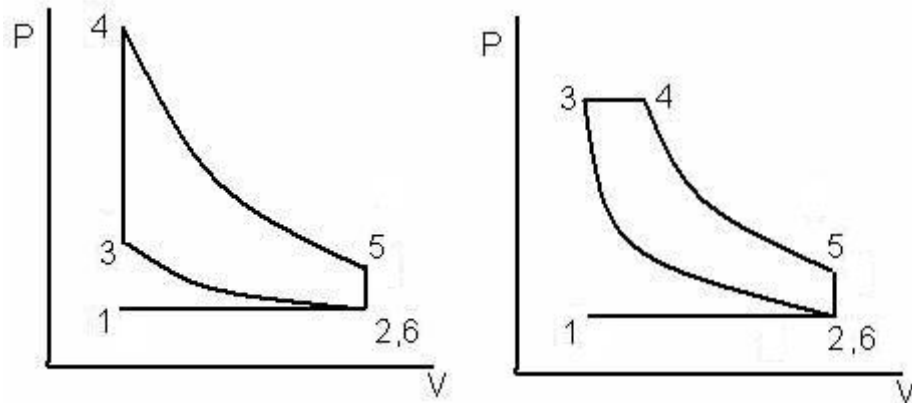


Figure 5.2. Pressure-volume (P-V) Diagram for Fast and Slow Combustion Process. Left: P-V diagram for constant-volume combustion process; Right: P-V diagram for constant-pressure combustion process.

In the P-V diagram for constant-volume combustion shown in Figure 5.2 (left), 1 → 2 is an isobaric (constant pressure) expansion, corresponding to the intake stroke. 2 → 3 is an adiabatic compression that corresponds to the compression stroke. 3 → 4 is an isochoric (constant volume) increase in pressure, corresponding to the combustion stroke. 4 → 5 is an adiabatic expansion process in which work is done by the gas on the piston. 5

$\rightarrow 6$ is an isochoric process in which the exhaust valve is opened and the residual heat in the gas escapes to the surroundings. $6 \rightarrow 1$ is an isobaric compression, which corresponds to the exhaust stroke.

The fuel efficiency η_f is defined as

$$\eta_f = W / (m_f Q_{LHV}), \quad (5.3)$$

where W is the total work done by the engine in the four strokes, m_f is the fuel mass consumed by the engine, and Q_{LHV} is the heating value of the liquid fuel. W is the sum of the compression stroke work W_C and the expansion stroke work W_E ,

$$W = W_C + W_E. \quad (5.4)$$

According to the laws of thermodynamics, in the constant volume combustion process as shown in Figure 5.2 (left), W_C and W_E are given by

$$W_C = U_2 - U_3 = mc_V(T_2 - T_3),$$

and

$$W_E = U_4 - U_5 = mc_V(T_4 - T_5), \quad (5.5)$$

where U is the internal energy, m is the mass of the gas in the combustion chamber, and c_V is the specific heat of the gas at constant volume, and T is temperature.

If the fuel is burned completely inside the combustion chamber, then the heat energy released is

$$m_f Q_{LHV} = mc_V(T_4 - T_3). \quad (5.6)$$

Using Equation 5.3–5.6, the fuel efficiency in the constant volume combustion process can be written as

$$\eta_{f,v} = 1 - \frac{T_5 - T_2}{T_4 - T_3}. \quad (5.7)$$

As usual c_p denotes the specific heat of the gas at constant pressure. Both c_p and c_v are constant, and their ratio γ is define as

$$\gamma = \frac{c_p}{c_v}. \quad (5.8)$$

The compression ratio, or the ratio of the maximum cylinder volumn V_2 to the minimum cylinder volumn V_3 , is defined as

$$r_c = \frac{V_2}{V_3} = \frac{V_5}{V_4}. \quad (5.9)$$

In the reversible adiabatic expansion and compression processes, the pressure and volume satisfy

$$P_2 V_2^\gamma = P_3 V_3^\gamma,$$

and

$$P_4 V_4^\gamma = P_5 V_5^\gamma. \quad (5.10)$$

For an ideal gas, the equation of state is

$$PV = nRT, \quad (5.11)$$

where $R = 8.314 \text{ J} / (\text{K} \cdot \text{mol})$ is the ideal gas constant, which is. According to

Equations 5.9, 5.10, and 5.11, the temperatures in a reversible adiabatic process satisfy

$$\frac{T_3}{T_2} = \frac{T_4}{T_5} = r_c^{\gamma-1}. \quad (5.12)$$

Using Equations 5.7 and 5.12, we find the fuel efficiency in the constant volume combustion process

$$\eta_{f,v} = 1 - \frac{1}{r_c^{\gamma-1}}. \quad (5.13)$$

Similarly, in the P-V diagram of the constant pressure combustion process shown on the right side of Figure 5.2, 1→2 is an isobaric (constant pressure) expansion, corresponding to the intake stroke. 2→3 is an adiabatic compression, corresponding to what happens in the compression stroke. 3→4 is an isobaric increase in volume, corresponding to the combustion stroke. 4→5 is an adiabatic expansion in which work is done by the gas on piston. 5→6 is an isochoric (constant volume) process in which the exhaust valve is opened and the residual heat in the gas escapes to the surroundings. 6→1 is an isobaric compression process, corresponding to the exhaust stroke.

In the constant pressure combustion process

$$W_C = U_2 - U_3 = mc_v(T_2 - T_3),$$

is the same as in the constant volume process, and

$$W_E = P_3(V_4 - V_3) + (U_4 - U_5) \quad (5.14)$$

is different.

In the isobaric expansion process 3→4,

$$c_p(T_4 - T_3) = P_3(V_4 - V_3) + (U_4 - U_3),$$

so

$$P_3(V_4 - V_3) = c_p(T_4 - T_3) - (U_4 - U_3). \quad (5.15)$$

According to Equations 5.4, 5.14 and 5.15, the work done by the engine in the constant pressure combustion process is

$$W = m[c_p(T_4 - T_3) + c_v(T_2 - T_5)]. \quad (5.16)$$

The heat energy released in burning process is given by

$$m_f Q_{LHV} = m\gamma c_v(T_4 - T_3). \quad (5.17)$$

Thus, the fuel efficiency in the constant pressure process is, using Equations 5.3, 5.8, and 5.17,

$$\eta_{f,P} = \frac{mc_v[\gamma(T_4 - T_3) + T_2 - T_5]}{mc_v\gamma(T_4 - T_3)} = 1 - \frac{T_5 - T_2}{\gamma(T_4 - T_3)},$$

or

$$\eta_{f,P} = 1 - \frac{T_2/T_3}{\gamma} \cdot \frac{T_5/T_2 - 1}{T_4/T_3 - 1}. \quad (5.18)$$

The cut-off ratio, α , which is the ratio between the final and initial volume for the combustion phase, satisfies

$$\frac{V_4}{V_3} = \frac{T_4}{T_3} = \alpha, \quad (5.19)$$

since the stroke is isobaric. In Equation 5.18, the term T_5/T_2 can be written

$$\frac{T_5}{T_2} = \frac{T_5}{T_4} \cdot \frac{T_4}{T_3} \cdot \frac{T_3}{T_2}. \quad (5.20)$$

2→3 is an adiabatic process, in which

$$\frac{T_3}{T_2} = \left(\frac{V_2}{V_3}\right)^{\gamma-1} = r_c^{\gamma-1}, \quad (5.21)$$

where

$$r_c = \frac{V_2}{V_3} \quad (5.22)$$

is the compression ratio, or the ratio of the maximum cylinder volume V_2 to the

minimum cylinder volume V_3 . In the adiabatic process 4→5, the temperature and volume satisfy

$$\frac{T_5}{T_4} = \left(\frac{V_4}{V_5} \right)^{\gamma-1}. \quad (5.23)$$

Notice that $V_5 = V_2$ in the P-V diagram of the constant-pressure combustion process.

Using this and Equations 5.19 and 5.22, Equation 5.23 become

$$\frac{T_5}{T_4} = \left(\frac{\alpha}{r_c} \right)^{\gamma-1}. \quad (5.24)$$

Finally, using Equation 5.18 to 5.21, and 5.24, we obtain

$$\eta_{f,P} = 1 - \frac{1}{r_c^{\gamma-1}} \cdot \frac{\alpha^\gamma - 1}{\gamma(\alpha - 1)}, \quad (5.25)$$

for the fuel efficiency in the constant pressure process. Here α is related to the specific enthalpy decrease per unit mass of the working fluids during the combustion. From Equation 5.17,

$$Q' = m_f Q_{LHV} / m = \gamma c_v (T_4 - T_3) = \gamma c_v (\alpha - 1) T_3. \quad (5.26)$$

Obviously, Q' is positive, which requires $\alpha > 1$. Comparing Equation 5.13 and 5.25 implies

$$\eta_{f,V} > \eta_{f,P}. \quad (5.27)$$

This means that the fuel efficiency of fast combustion (constant volume process) is higher than that of slow combustion (constant pressure process) when in both combustion processes the fuel is burned completely inside the combustion chamber.

Using the parameters $\gamma = 1.3$, $r_c = 12$, and $\alpha = 4.12$, which correspond to working fluid properties in a real engine, we compare the fuel efficiencies in the fast and

slow combustion process. In constant pressure (slow) combustion process, the fuel efficiency $\eta_{f,P}$ is 0.380, and in the constant volume combustion (fast) process, the fuel efficiency $\eta_{f,V}$ is 0.525 . Thus, assuming the 100% burning percentage or combustion efficiency, the fuel efficiency can be improved by 38.3% for the same engine by increasing the combustion speed.

The limited pressure combustion model shows that the fuel efficiency in the engine improves as the combustion speed increases (Heywood, 1988). The constant-volume combustion process has infinitely fast combustion and the highest efficiency for a given engine.

5.1.3 Viscosity Reduction Increases Fuel Efficiency

Slow combustion occurs when large fuel droplets are injected into the combustion chambers. The combustion takes more time, and some heat is released too late to be utilized. With smaller fuel droplets, the fuel-air mixing is improved, and the combustion is faster and cleaner, with heat released in time to push the piston. It is clear that the fuel efficiency is higher the finer the fuel droplets.

5.2 Diesel, Gasoline and Ethanol Fuels

Diesel fuel can be produced from crude oil or other substances. The resulting products are interchangeable in most applications. Diesel fuel generally refer to any of the fuels used in diesel engines, such as the most common petroleum diesel, and alternatives that are not derived from petroleum, including biodiesel, biomass to liquid (BTL), and gas to liquid (GTL) diesel (Diesel, n.d.). If not specified, the diesel fuel mentioned in this chapter refers to diesel fuel distilled from crude oil, sometimes referred to as petrodiesel (Collins, 2007) or fossil diesel. It is produced by the fractional distillation of crude oil at temperatures between 200 °C and 350 °C in atmospheric pressure. The resulting product is a mixture of molecules that normally have 8 to 21 carbon atoms per molecule.

Gasoline, also known as petrol, is another fuel derived from crude oil. Actually it is a mixture of several products of the refining. Generally it consists of aliphatic hydrocarbons, enhanced with iso-octane or the aromatic hydrocarbons toluene and benzene to increase the octane rating (Gasoline, n.d.). Different grades of gasoline are produced by adjusting the ratios. Usually, for tuning the engine performance or reducing harmful exhaust emissions, small quantities of various additives are added to gasoline.

Sometimes significant amounts of ethanol are used as a partial alternative fuel to gasoline. When anhydrous ethanol (ethanol with less than 1% water) is mixed with gasoline in varying percentages up to 100%, the mixture is denoted by the ethanol percentage, for example, E10, E20 ... and E100 (Ethanol Fuel, n.d.). Most modern gasoline engines operate well with mixtures of 10% ethanol (E10). E85 is a fuel mixture

that usually contains up to 85 volume percentage of denatured fuel ethanol and gasoline or other hydrocarbons (HC). On an undenatured basis, the ethanol component ranges from 70% to 83% (E85, n.d.).

5.3 Reducing Viscosities of Fuels

The viscosities of fuels can be reduced by exposure to magnetic or electric fields using the same field treatment techniques as for crude oils.

5.3.1 *Temperature Effects on Fuels*

The viscosities of fuels decrease as temperature increases. This is referred to as the temperature effect. Generally, the temperature effect applies to all kind of fuels. As an example, the temperature effect for pure diesel obtained from Sunoco refinery is shown in Figure 5.3. According to Figure 5.3, the viscosity of diesel fuel at 65 °C is approximately half of the value at 25 °C. If sample temperature before and after field treatment is different, temperature effect needs to be considered.

5.3.2 *Reducing Viscosity of Fuels by Magnetic Field*

From the theory considered in chapter 2, a pulsed magnetic field greater than the critical field can reduce the viscosity of pure gasoline, pure diesel, and those fuels with ethanol or additives. Since current gasoline for vehicles contains additives, experiments were carried out on gasoline with additives.

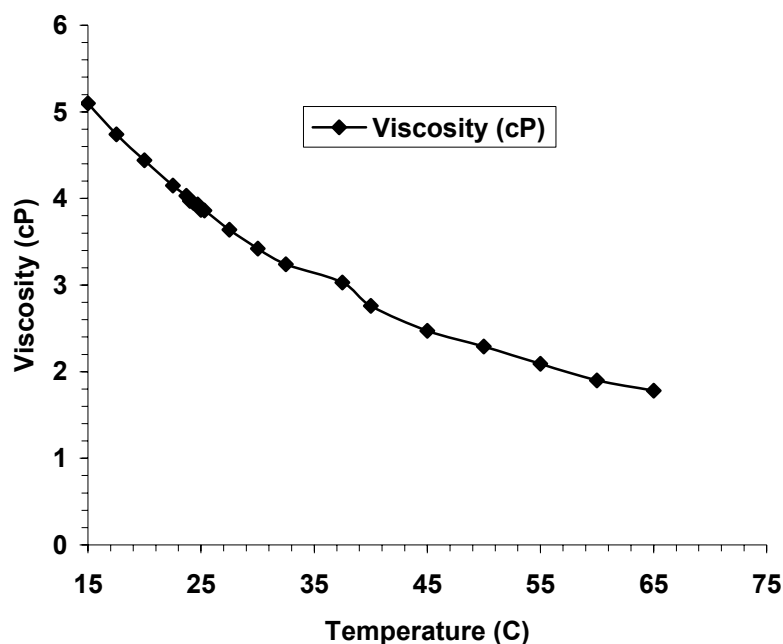


Figure 5.3. Temperature Effect on Viscosity of Pure Diesel.

MTBE (methyl tertiary butyl ether) is a volatile, flammable and colorless liquid that is immiscible with water. It has the molecular formula $C_5H_{12}O$. Experiments on gasoline with 10% MTBE were conducted, since MTBE was widely used at the time of the experiment as an oxygenate and to raise the octane number. The viscosity of MTBE is slightly higher than that of gasoline, which gives a mixture of gasoline with 10% MTBE at 10 °C a very low viscosity of 0.84 cP, slightly higher than that of pure gasoline. An optimal result was achieved with a magnetic field treatment of 1.3 Tesla applied for around 1 second. Right after the field treatment, the apparent viscosity of the sample immediately dropped to 0.77 cP. Then it fluctuated around 0.78 cP for several hours before gradually increasing. As shown in Figure 5.4, after more than 2 hours, the viscosity was still about 7% below the original value 0.84 cP.

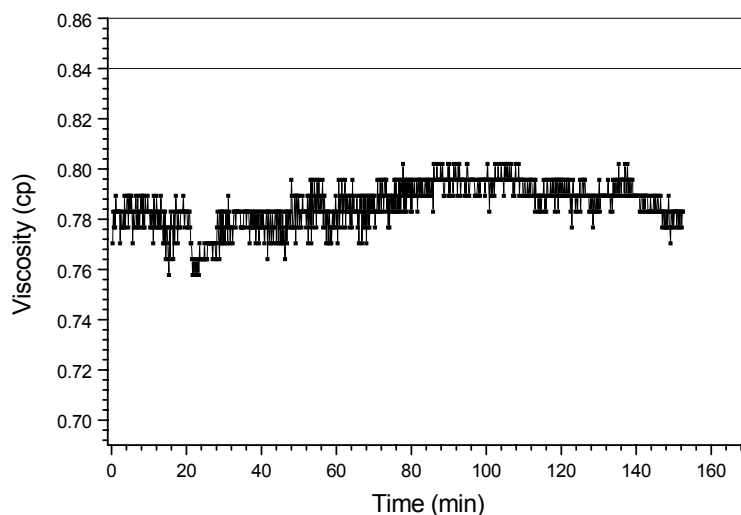


Figure 5.4. Viscosities of Gasoline with 10% MTBE before and after Magnetic Field Treatment. The viscosity at 10 °C after application of a magnetic field of 1.3 Tesla for 1 second drops 7% from its original viscosity 0.84 cP.

The measurements were made with the Brookfield DV-III viscometer with the LV spring set and the ULA spindle at 95 RPM. The temperature during, before, and after the treatment was unchanged.

As previously mentioned, in gasoline on the market, a certain amount of ethanol is substituted for gasoline. Gasoline with 20% ethanol (E20) is claimed to burn cleaner and will be widely adopted in the near future. Therefore, experiments with E20 were conducted. It is worth mentioning that pure gasoline has a viscosity lower than water, of around 0.8 cP at 10 °C. On the other hand, ethanol has a viscosity higher than water, about 1.7 cP at 10 °C. Therefore, a mixture of 80% gasoline and 20% ethanol has a viscosity around 0.95 cP. A strong magnetic field of 1.3 Tesla applied for 5 seconds is very effective in reducing the viscosity of E20. In one of the experiments, immediately after the field treatment, the apparent viscosity dropped to 0.81 cP, then soon climbed to

about 0.875 cP. After 3 hours, the apparent viscosity remained at 0.88 cP, 8% below the original value. The result is shown in Figure 5.5.

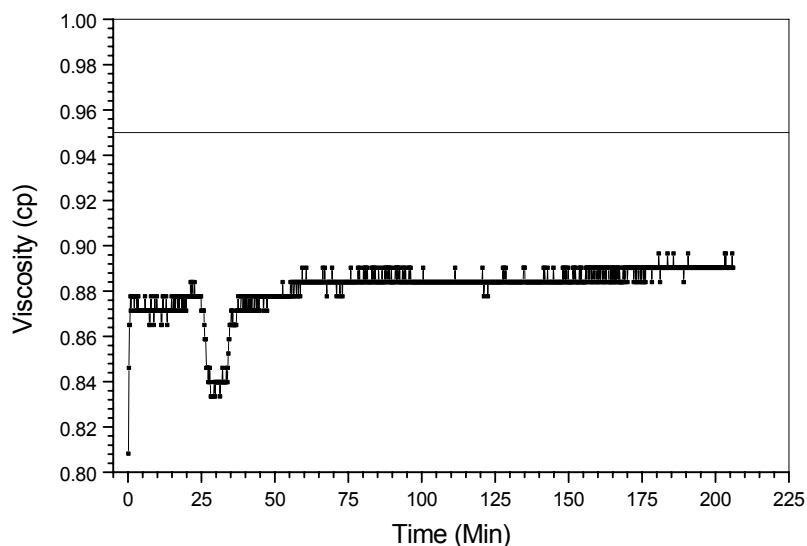


Figure 5.5. Viscosities of E20 before and after Magnetic Field Treatment. Viscosity of gasoline with 20% ethanol at 10 °C after application of a magnetic field of 1.3 Tesla for 5 second drops 8% from its original value of 0.95 cP.

This behavior is similar to that of gasoline with MTBE in a pulsed magnetic field. However, for gasoline with 20% ethanol, the magnetic pulse duration should be longer than that for gasoline with 10% MTBE.

The diesel sample provided by Sunoco refinery is pure diesel fuel refined from crude oil, without any further processing, which is different from the diesel fuel available on the market. The diesel fuel sample was stored in a special container provided by the company, as shown in Figure 5.6.



Figure 5.6. Pure Diesel Fuel from Sunoco in Special Container.

The viscosity of diesel fuel is much higher than that of gasoline. Experiments were conducted with pure diesel and diesel fuel with 0.5 % of ethylhexyl nitrate (EHN) as additive. Both samples are very similar since the volume fraction of the additive is small. The initial viscosity of the diesel fuel was 5.80 cP at 10 °C, which is considerably higher than that of gasoline. After a magnetic field treatment of 1.1 Tesla for 8 seconds, the apparent viscosity dropped to 5.64 cP, then remained at 5.70 cP for several hours. This is shown in Figure 5.7.

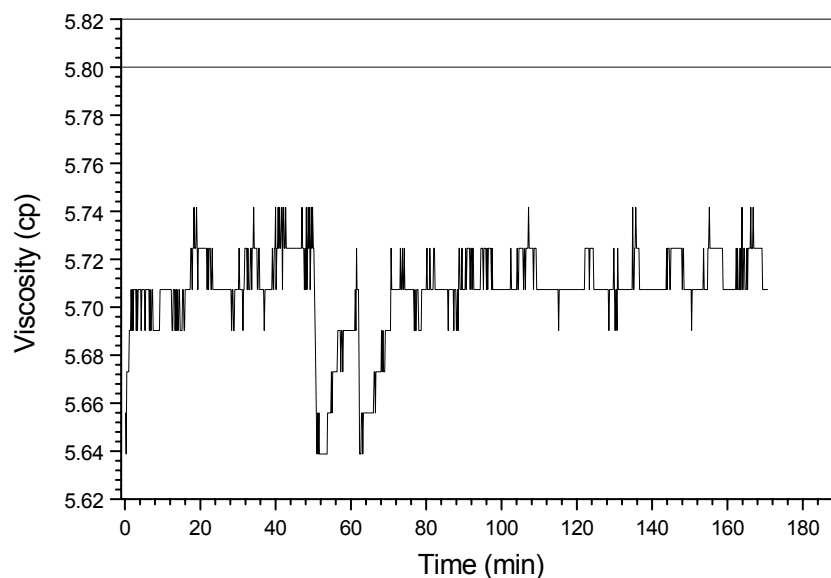


Figure 5.7. Viscosities of Pure Diesel before and after Magnetic Field Treatment. Viscosity of diesel at 10 °C after application of a magnetic field of 1.1 Tesla for 8 second drops 2%.

5.3.3 Reducing Viscosity of Fuels with Electric Field

The magnetic fields required for significant viscosity reduction in fuels are relatively large, which is a major problem in the realization of compact devices that can be mounted on vehicles. However, strong electric fields also reduce the viscosity of fuels. It is much easier to design compact devices for vehicles that utilize high voltage. This provided motivation for our experiments on electric field treatments.

Experiments were performed with electric field treatment of diesel fuel, E20, and E85. Both pure diesel and diesel were used in the experiments. An optimal result is shown in Figure 5.8.

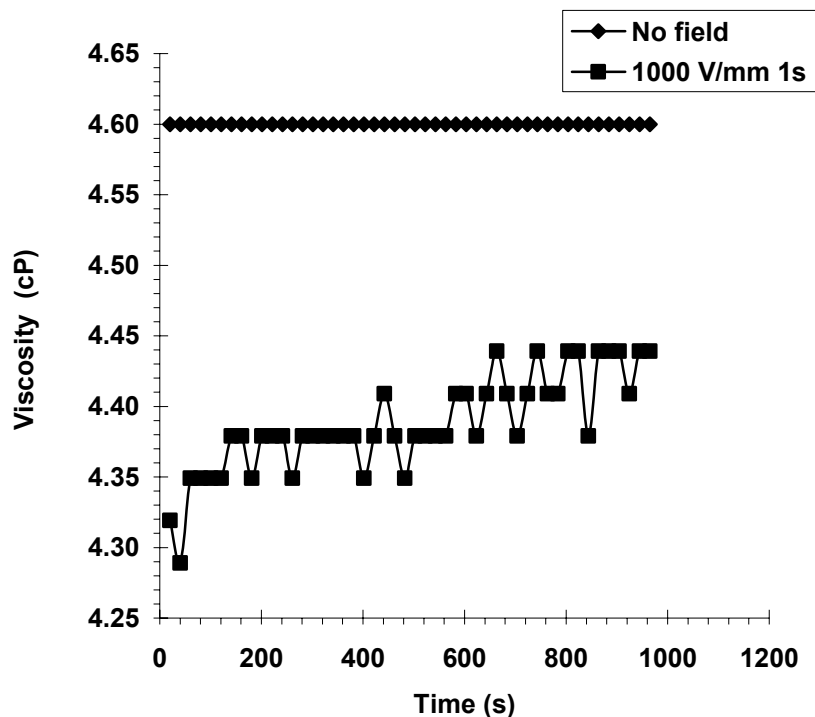


Figure 5.8. Viscosities of Pure Diesel before and after Electric Field Treatment. Viscosity of diesel obtained from Sunoco refinery at 19.5 °C after application of an electric field of 1000 V/mm for about 1s second dropped 7%.

For pure diesel fuel, the viscosity at 19.5 °C was 4.6 cP before treatment. After exposure to an electric field 1000 V/mm for about 1 second, the viscosity dropped to 4.3 cP, which corresponds to a 7% reduction. The measurement was made with the Brookfield DV-II+ Pro viscometer with the LV spring set and the ULA adapter at 20 RPM.

Experiments on Sunoco diesel obtained from a gas station showed that this diesel fuel is different from what we obtained from refinery. The viscosity of diesel fuel from the gas station was much lower than the pure diesel fuel from the refinery. At room

temperature around 22.5 °C, the viscosity of pure diesel fuel was around 4.15 cP as indicated in Figure 5.3, whereas the viscosity of gas station diesel was around 3.15 cP.

The electric field did reduce the viscosity of the gas station diesel fuel, but the reduction was lower than for pure diesel fuel. Figure 5.9 shows an optimal result for an electric field of 900 V/mm applied for 2.5 s.

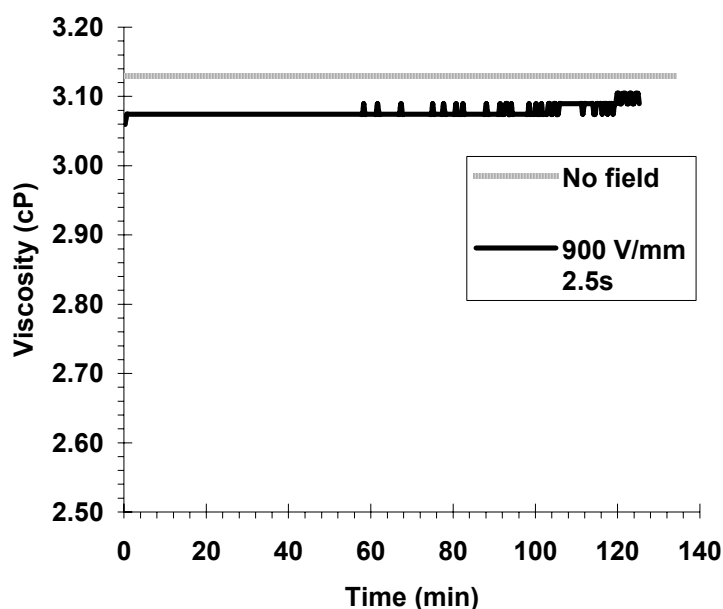


Figure 5.9. Viscosities of Gas Station Diesel before and after Electric Field Treatment. Viscosity of diesel from Sunoco gas station at 22.4 °C after application of an electric field of 900 V/mm for about 2.5 second dropped 3%.

Before the field treatment, the diesel fuel had an average viscosity around 3.15 cP at 22.4 °C. After the field treatment it dropped to 3.06 cP and gradually increased. As shown in Figure 5.9, the viscosity was still below its original value after 2 hours. The viscosities were measured with the Brookfield DV-II+ Pro rotational viscometer with the LV spring set and the ULA adapter at 40 RPM.

Similar experiments were carried out for E20 and E85. It was found that for 1000 V/mm applied for 1 s, the viscosity of E20 dropped 3.4% from its original value of 0.88 cP to 0.85 cP immediately after the treatment. Then it decreased further to 0.82 cP before gradually increasing. In 2.5 hours, it increased back to its original value. The temperature was unchanged before and after the treatment and was around 19.5 °C. The result is shown in Figure 5.10. The viscosities were measured with the Brookfield DV-II+ Pro rotational viscometer with the LV spring set and the ULA adapter at 90 RPM.

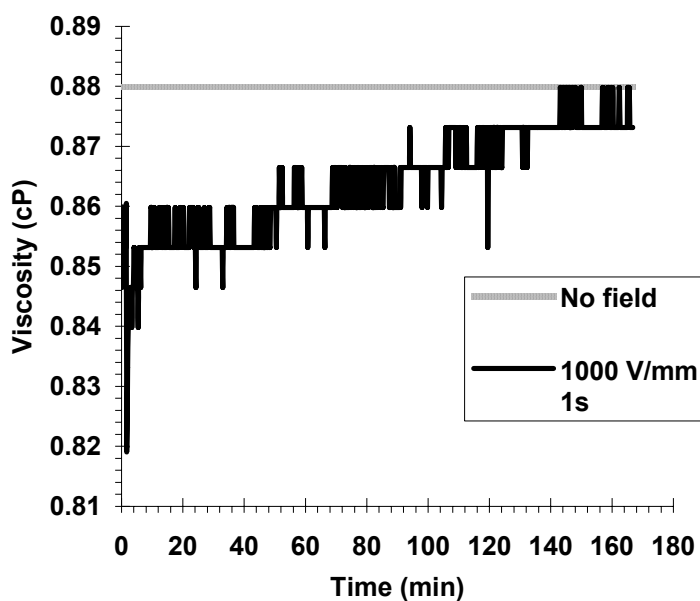


Figure 5.10. Viscosities of E20 before and after Electric Field Treatment. Viscosity of E20 at 19.5 °C after application of an electric field of 1000 V/mm for about 1 second dropped 3.4% immediately after the field treatment.

In the experiments on E85, after an electric field treatment of 133.3 V/mm for 20 seconds, the viscosity of E85 dropped from 1.16 cp to 1.10cp at 22 °C and gradually increased after that. However, the viscosity remained substantially below the initial value

for more than an hour after application of the electric field. This is shown in Figure 5.11.

The measurement was taken with the Brookfield DV-II+ Pro rotational viscometer with the LV spring set and the ULA adapter at 80 RPM.

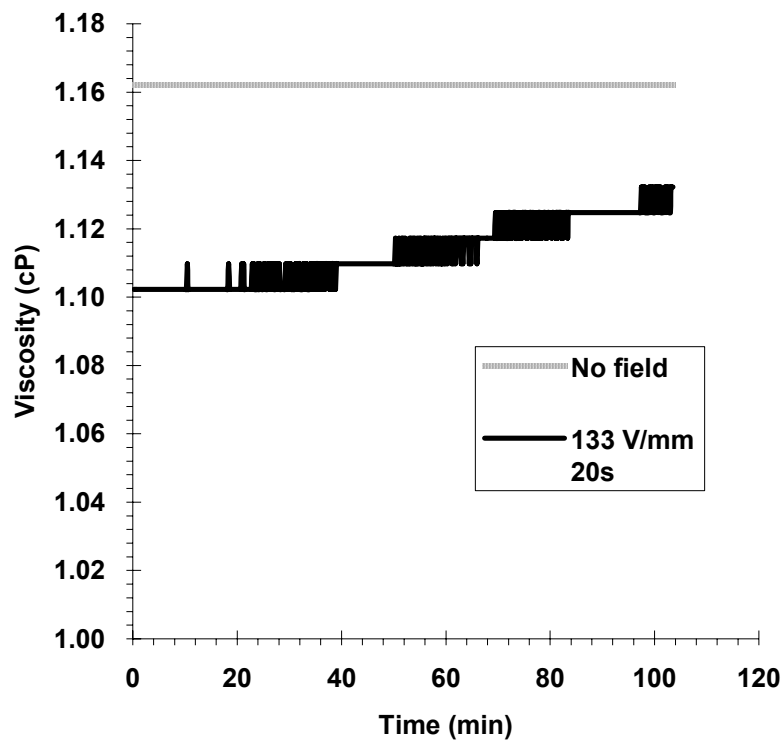


Figure 5.11. Viscosities of E85 before and after Electric Field Treatment. Viscosity of E85 at 22.4 °C after application of an electric field of 133 V/mm for about 20 second dropped from 1.16 cP to 1.10 cP immediately after the field treatment.

5.4 Flow Experiments with Diesel

Flow experiments with diesel fuel were also conducted and the results are consistent with the results described above.

5.4.1 Experiment Setup in Flow Experiments

The field treatment device in the flow experiments was the solid plate capacitor sample treatment container discussed in chapter 2. The schematic of the setup is shown in Figure 5.12.

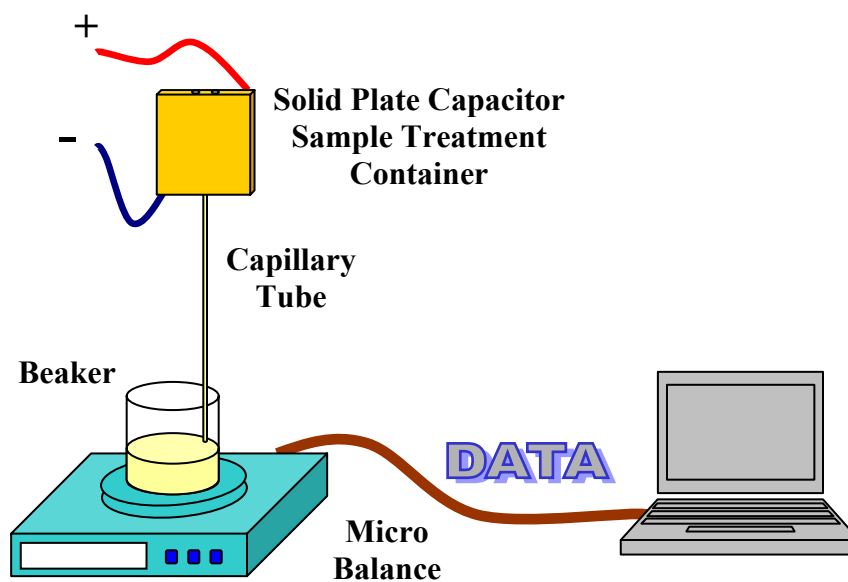


Figure 5.12. Experiment Setup in Diesel Flow Experiment.

As shown in the schematic, after field treatment in the sample treatment container, the diesel sample flows down through a capillary tube into the collecting beaker, which is placed on a micro balance. Readings from the micro balance are collected in real time by a home made Labview program. The flow rate of the diesel sample is derived from accumulation rate of mass in the beaker and the viscosity of the sample is directly proportional to the flow rate, keeping other conditions the same. The interface of the home made Labview program is shown in Figure 5.13.

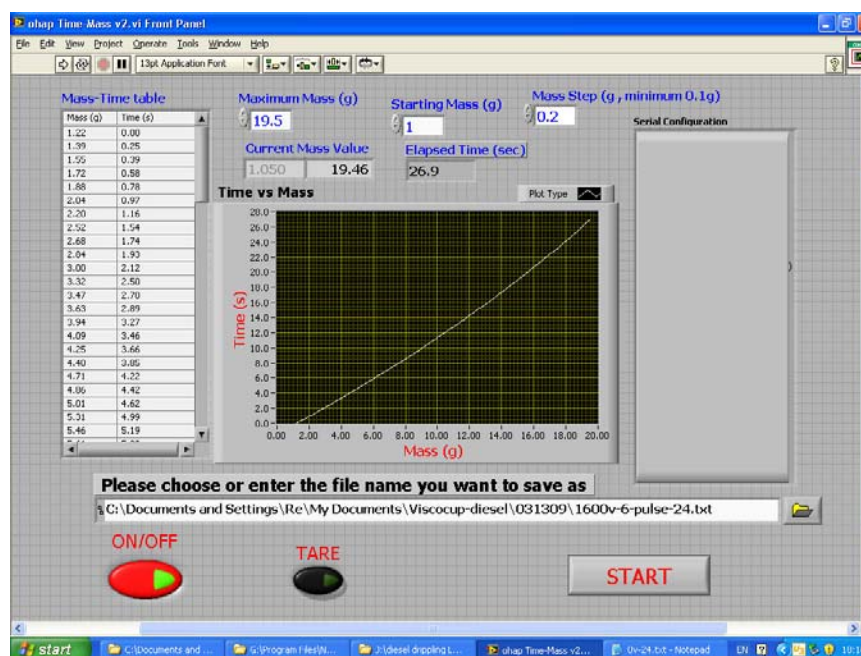


Figure 5.13. Home Made Labview Program Used in Diesel Flow Experiment. Rate of the mass increase of sample in the beaker is measured by the program.

As with crude oil, even after thorough mixing, different samples taken from the same container in two times may still have slightly different viscosity. To eliminate this discrepancy, the same diesel sample was used in the viscosity measurement before and

after the field treatment. In the experiment, the diesel sample flowed through the sample treatment container and capillary tube without any field applied. The mass increase and elapsed time were recorded by the program. Then the same sample was poured back into treatment container and exposed to the electric field before flowing through the capillary tube. The rate of mass increase revealed the change of the viscosity. If the viscosity decreases after the field treatment, the mass increases faster than that before treatment.

5.4.2 Varying Field Strength with Constant Duration Time

Experiments were carried for several different field strength keeping the duration time at 4 s. In different trials, the flow time was normalized with the time before treatment being 100. In this way, data from different trial could be comparable. The results are shown in Table 5.1.

Table 5.1 Flow Experiments for Diesel Fuel with Different Field Strength and Constant Application Time 4 s

Field Strength (V/mm)	Current (uA)	Field Duration		Temperature (°C)	Mass (g)	Flowing Time normalized to 100
		Time (s)				
0	0.0			19.90	89.96	100.00
800	0.8	4.1		19.90	89.94	97.98
0	0.0			19.90	89.95	100.00
1000	1.0	4.0		19.90	89.96	97.86
0	0.0			19.90	89.96	100.00
1200	1.2	4.0		19.90	89.97	92.37
0	0.0			20.05	89.98	100.00
1300	1.2	4.0		20.10	89.94	100.57

As shown in the table, as the field strength increased from 800 V/mm to 1200 V/mm, the flow time of sample decreased, which indicates that the viscosity decreases as field increases. This is due to aggregation of small particles into larger particles in the diesel fuel. As the field strength increases further, the viscosity increases, as indicated by a increasing flowing time. This is because the excessive field treatment produces particle chains, which jam the flow.

The temperatures before and after field treatment normally did not change. Only in the case of 1300 V/mm did the temperature increase slightly by 0.05 °C, but the temperature effect was negligible.

5.4.3 Varying Duration Time with Constant Field Strength

We also performed experiments with constant field strength and variable field duration. Table 5.2 shows the results from experiments with field strength of 1000 V/mm and varying duration.

Table 5.2 Flow Experiments for Diesel Fuel with Different Duration Time and Constant Field Strength at 1000 v/mm

Field Strength (v/mm)	Current (uA)	Field Duration Time (s)	Temperature (°C)	Mass (g)	Flowing Time normalized to 100
0	0.0		19.90	89.97	100.00
1000	1.0	3.1	19.90	89.96	99.96
0	0.0		19.90	89.95	100.00
1000	1.0	4.0	19.90	89.96	97.86
0	0.0		20.15	89.97	100.00
1000	1.0	5.2	20.20	89.97	97.09

As shown in the table, as the duration time increased from 3.1 second to 5.2 second, the flow time decreased. There was no significant temperature difference before and after the treatment.

5.5 Spray Experiment and Results

In order to confirm that reducing the viscosity of fuels increases the fraction of droplets of smaller size in the atomization process in the fuel injector, spray experiments were conducted.

5.5.1 Method and Experiment Setup

The setup spray used in the spray experiment is shown in Figure 5.14. Descriptions of the components can be found in chapter 3.

The fuel was stored in a pressurized fuel container connected to a cylinder of compressed small nitrogen gas. The pressure inside the fuel container was exerted by the compressed nitrogen gas, and the pressure could be adjusted by a valve with a scale.

The pressure pushes fuel inside the container into the field application device through the fuel pipe. There are two meshes in the field application device connected leads to high the voltage power supply. After being treated in the device, fuel is sprayed out through the fuel injector. A trigger opens the injector when a high voltage is received from the control circuit. Thus, by adjusting the duration of the high voltage, the duration of the spray is controlled. If the duration is too short, too few droplets are collected for analysis. If the duration is too long, too many droplets overlap with each other, complicating the data analysis.

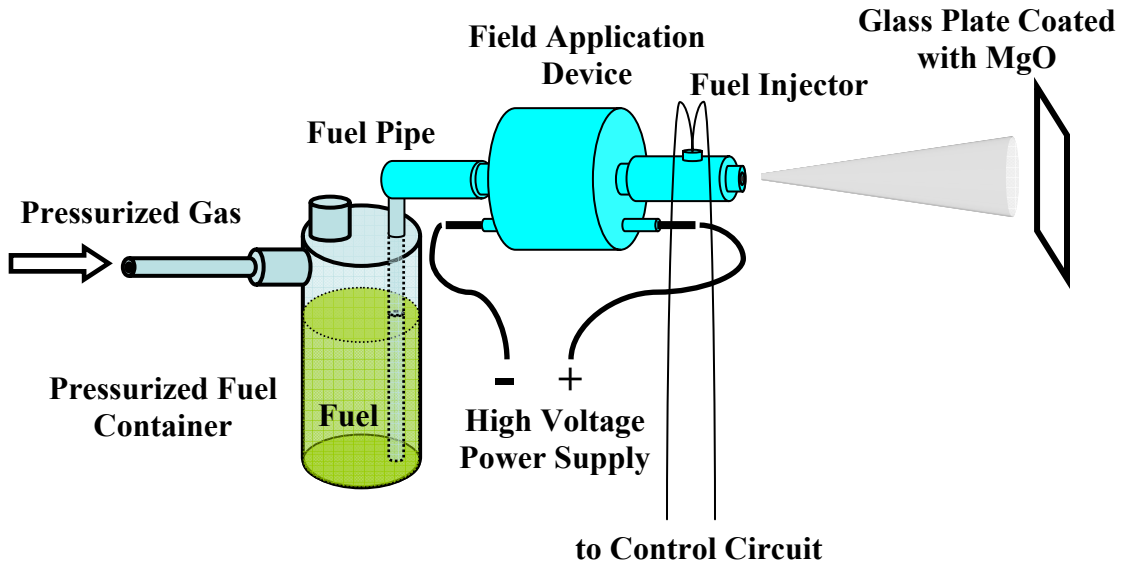
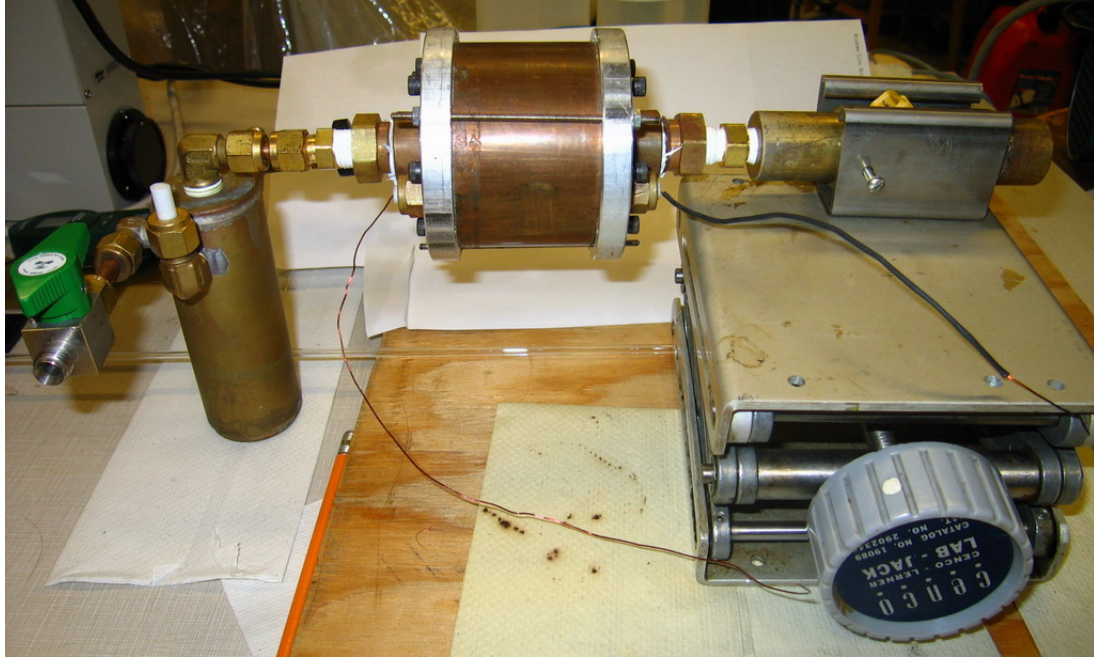


Figure 5.14. Photograph Schematic of Spray Experiment Setup.

A home made control circuit is used to trigger the fuel injector. The main component in the control circuit is a 555 Timer. The pulse duration is modified by

changing the resistors and capacitors in the circuit. The time constant is the product of the resistance and capacitance. For instance, if a 40 k Ω resistor and a 0.1 μ F capacitor are used in the circuit, the time constant is 4 ms. This circuit can be used to open the fuel injector for 4ms fuel.

Fuel droplets sprayed out by the injector are collected on a glass plate coated with magnesium oxide (MgO). Magnesium oxide, also known as magnesia, is a white solid mineral with chemical formula MgO (Magnesium Oxide, n.d.). The molecule is formed by an ionic bond between one magnesium and one oxygen atom. The glass plate is coated with MgO by burning a magnesium ribbon under the glass plate. Magnesium oxidation produces a bright white light so sun glasses are used as eye protection. A white fume of MgO is emitted while the magnesium is burning. If the burning ribbon is held below the glass plate, the plate is coated with MgO. Some practice is required to coat the plate with a uniform layer of MgO.

5.5.2 Image Processing and Data Analysis

Actually, the fumes of Magnesium Oxide are composed of tiny MgO particles with diameter at the micrometer level or less. During the spray, the fuel droplets knock MgO particles off the glass plate and leave small dots on the plate. Then the plate is examined with high definition scanner at a resolution of 9600 dpi. One of the scanned images and a close-up of the upper left corner are shown on in Figure 5.15.

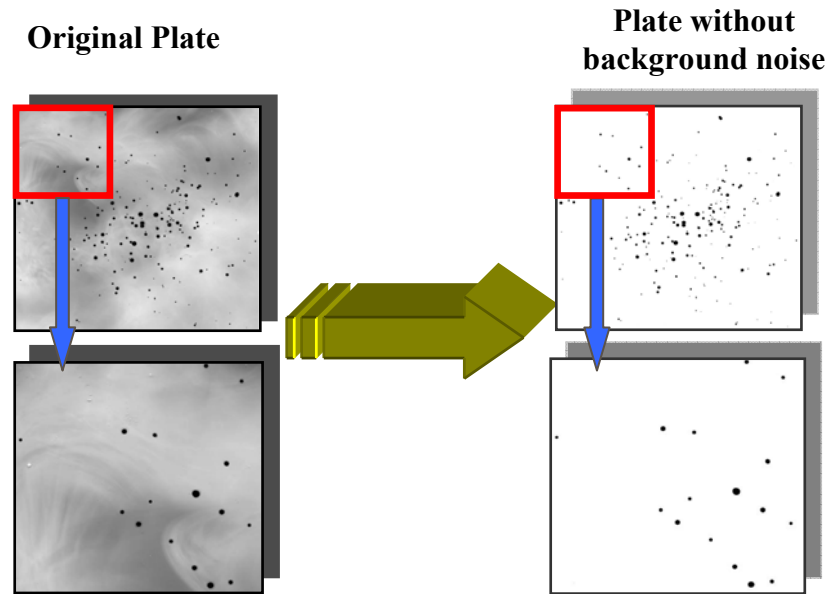


Figure 5.15. Original Scan and Processed Image of Plate in Spray Experiment.

As shown in the picture, fuel droplets sprayed from the fuel injector create the dark dots in the original scanned image. The scanned image has a background with bright and dark regions. This leads to unreliable statistics of the particle distribution if the image is not processed. Adobe Photoshop 7.0 and ImageJ 1.33u were used for the processing. Basically, the image processing removes the uneven background without introducing other noise or changing the size of the droplet dots. The processed images of the original scan and the close-up are shown on the right side of Figure 5.15.

ImageJ is able to analyze the statistics of the number of particles of different sizes. Many plates sprayed with the same experimental settings are analyzed in a data group. One can set the bin size and sort the particles according to their radii.

5.5.3 Experiment Results for Diesel, E20 and E85

Experiments were performed with diesel oil from Sunoco refinery, E20 and E85, respectively. In the experiment, the fuels were first sprayed onto a set of glass plates coated with MgO without any field treatment. Then field treated fuels were sprayed onto another set of glass plates. The results diesel with a field treatment of 1000 V/mm for 15 s and without any filed treatment are shown in Figure 5.16.

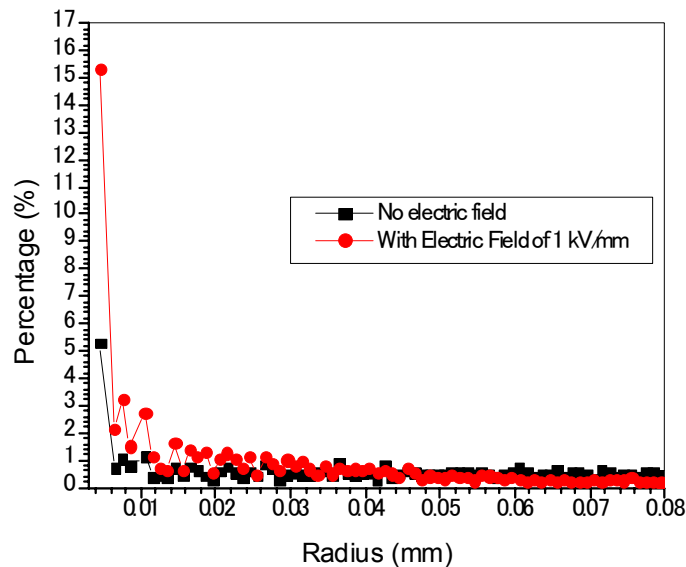


Figure 5.16. Particle Distributions before and after Field Treatment in Diesel Spray Experiment. The applied field was 1000 V/mm for 15 seconds. The number of droplets of radius below 5 μm increased from 5.3% to 15.3%.

The number of droplets of radius below 5 μm increased from 5.3% to 15.3%, a factor of 3. After field treatment, radius of most droplets was below 40 μm . For E20 gasoline, an optimal field treatment was 1200 V/mm for 15 s. The number of droplets with radius of (10 ± 2.5) μm increased from 17.6% to 20.7%, which was an increase of

15%. The results are shown in Figure 5.17. During the experiment, the current through the samples was very low, so the temperature effect was negligible.

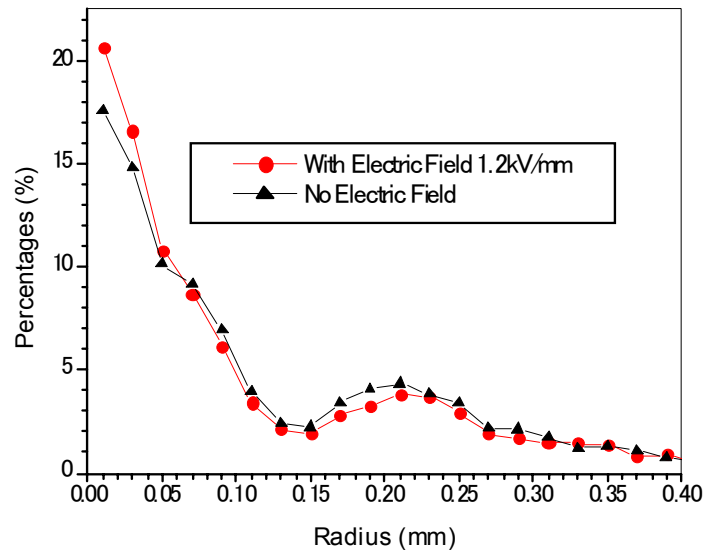


Figure 5.17. Particle Distributions before and after Field Treatment in the E20 Spray Experiment. The applied field was 1200 V/mm for 15 seconds. The number of droplets with radius of (10 ± 2.5) μm was increased from 5.3% to 15.3%.

It should be mentioned that the spray experiment for E85 was carried out close to 0 °C. The reason is that with E85 fuel, diesel engines are difficult to start in winter when the temperature is very low. If atomization of the fuel becomes better and droplets sprayed into the engine is improved and the droplets sprayed into the engine are smaller, then better combustion is achieved. This can help solve the cold start problem for the E85 engine in winter time. The special setup for the E85 spray experiment and a modified schematic from Figure 5.14 are shown in Figure 5.18.

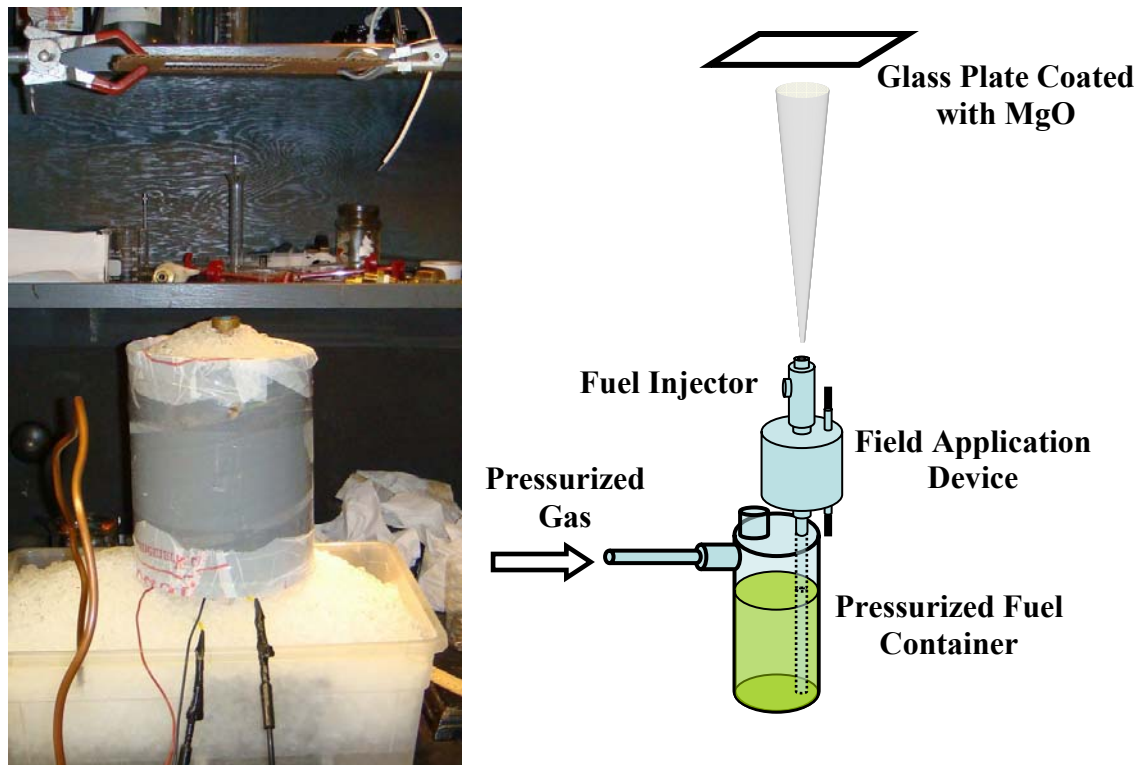


Figure 5.18. Special Setup for E85 Spray Experiment. The whole device was surrounded by ice. The fuel was sprayed vertically upward and collected on the glass plate coated with MgO.

All the components were buried in ice and the fuel injector injected upward onto the glass plate coated with MgO. The particle distributions for the E85 spray before and after a field treatment of 150 V/mm for 20 s are shown in Figure 5.19.

After the field treatment, the number of droplets with radius of $30 \pm 5 \mu\text{m}$ increased from 2.9% to 7.7%, corresponding to a factor or period 2.7 the number of droplets with radius of $(55 \pm 5) \mu\text{m}$ increased from 5.1% to 9.7%, a factor 1.9 times.

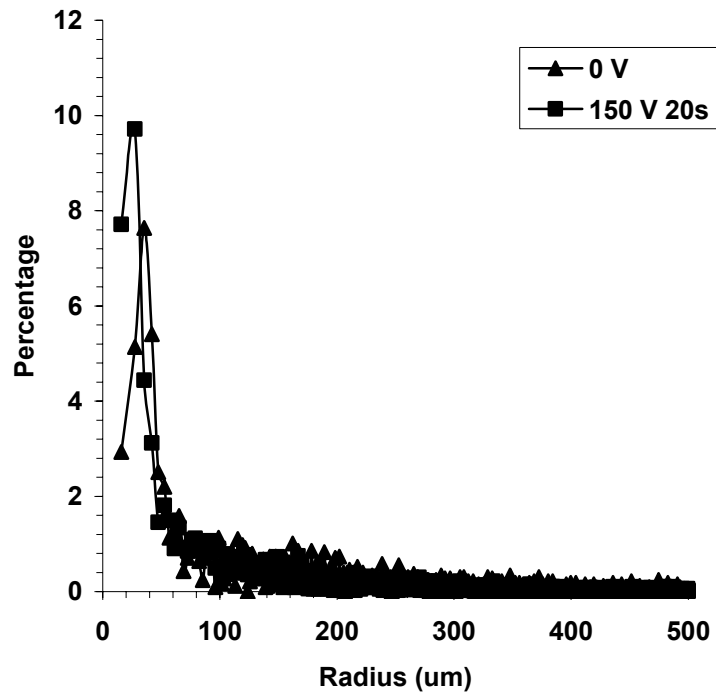


Figure 5.19. Particle Distributions before and after Field Treatment for E85 Spray Experiment. The applied field was 150 V/mm for 15 seconds. The number of droplets with radius of $(10 \pm 5) \mu\text{m}$ increased from 5.3% to 15.3%.

5.6 Improving Fuel Efficiency by Electric Field Treatment

The results from the smalls Spray experiments indicate that electric field is very effective in improving the diesel atomization. Electric field treatment in diesel engines should result in greater fuel efficiency and lower emission pollution. Extensive tests with our field treatment method on diesel engines have been conducted.

5.6.1 Engine Test at Cornaglia Iveco

One engine test was conducted at Cornaglia Iveco, a famous Italian diesel engine manufacturer. In the test, our field application device was installed in the fuel line before it entered the engine. The setup for the experiment is shown in Figure 5.20.

The fuel consumption rate and the power output were measured at constant engine speed. A typical heating value for diesel fuels is between 134,000 and 148,000 Btu/gal, and the density of diesel fuels is between 0.8 to 0.86 kg/l (Song, Hsu and Mochida, 2000). Since $1 \text{ Btu} = 1055.06 \text{ J} = 0.2931 \times 10^{-3} \text{ kW} \cdot \text{h}$, and $1 \text{ gal} = 3.78 \text{ l}$, the heating value for diesel fuels is between 12.08 and 14.34 $\text{kW} \cdot \text{h} \cdot \text{kg}^{-1}$. In calculation of the fuel efficiencies (Equation 5.3), the upper limit of the heating value was used.

Brake specific fuel consumption (BSFC) is a quantity which measures the fuel efficiency in a shaft reciprocating engine and allows the fuel efficiency of different engines to be directly compared (Brake Specific Fuel Consumption, n.d.). The BSFC at a particular speed is defined as the fuel consumption rate of an engine divided by the power produced. The formula is

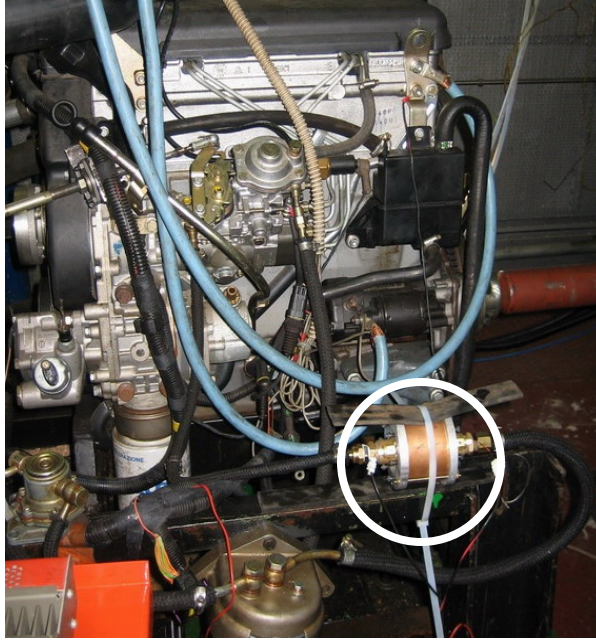


Figure 5.20. Test of Field Application Device on Diesel Engine. The experiment was conducted at Cornaglia Iveco, Italy. The field application device circled in the picture was installed in the fuel line before it entered the engine.

$$BSFC = \frac{r_{FC}}{P}, \quad (5.28)$$

where r_{FC} is the fuel consumption of the engine at a particular speed and P is the output power of the engine. The unit of BSFC is $\text{g}\cdot\text{kW}\cdot\text{h}^{-1}$.

Table 5.3 shows test results with and without a 1300 V/mm electric field in the device with field direction antiparallel to the flow direction of the fuel. The results are averages of measurements for 1 week, with an error bar of 2%.

According to the table, at an engine speed of 1900 RPM, the BSFC was $220.1 \text{ g}\cdot\text{kW}\cdot\text{h}^{-1}$ with no field applied in the device. It dropped to $208.7 \text{ g}\cdot\text{kW}\cdot\text{h}^{-1}$ with a field around 1300 V/mm applied to the diesel fuel, a change of 5.2%. The fuel efficiencies with the field application device off were 28.81%, 31.68%, and 29.95% at engine speeds of 3400 RPM, 1900 RPM and 1500 RPM, respectively. With the device on, these values

Table 5.3 Diesel Engine Test Results with and without Field Treatment

Field V/mm	Engine Speed RPM	Power kW	Fuel Consumption kg·h ⁻¹	BSFC g·kW·h ⁻¹	Fuel Efficiency %	Increase %
0	3400	81.1	19.63	242.0469	28.81	n/a
0	1900	54.7	12.04	220.1097	31.68	n/a
0	1500	41.4	9.77	235.9903	29.55	n/a
1300	3400	80.6	19.14	237.469	29.37	1.93
1300	1900	54.2	11.31	208.6716	33.42	5.48
1300	1500	41.4	8.89	214.734	32.48	9.90

increased by 1.93%, 5.48%, 9.90%, respectively.

The dependence on the field direction was also tested with field strength 1300 V/mm. Besides field direction antiparallel to the flow direction, field directions parallel and perpendicular to the flow direction were tested. The results are listed in Table 5.4.

Table 5.4 Diesel Engine Test Results with Different Field Direction

Field V/mm	Field Direction to Fuel Flow	Engine Speed RPM	Power kW	Fuel Consumption kg·h ⁻¹	BSFC g·kW·h ⁻¹	Fuel Efficiency %	Increase %
0	no field	1900	54.7	12.04	220.11	31.68	n/a
1300	perpendicular	1900	54.9	11.65	212.20	32.86	3.73
1300	parallel	1900	53.9	11.33	210.20	33.17	4.71

According to the results in Table 5.4 and Table 5.3, when the applied electric field direction was parallel to the fuel flow direction, the fuel efficiency was improved by

4.71%, which is 0.77% lower than the improvement when the field direction was antiparallel to the flow direction. This may be due to electrons attaching to the fuel droplets with field direction opposite to the flow direction, which further reduced the droplet size. Greater improvement in fuel efficiencies was achieved when field direction was parallel or antiparallel to the flow direction, compared to a 3.73% increase with the field direction perpendicular to the flow direction.

Emission tests showed that NO_x emissions by the diesel engine decreased with the field application device on. For example, the NO_x emissions decreased from 570 to 550 ppm at an engine speed of 1900 rpm with an error of 1%.

The results of the engine tests at Cornaglia Iveco are promising. However, they were below our expectation from the spray experiments. The main reason may be the short treatment time of the diesel fuel when flowing through the field application device. In the tests, diesel fuel flowed through the electric field in about 1 s at an engine speed of 1900 rpm. If the diesel fuel flows through the electric field for a longer time, better fuel efficiency may be achieved.

5.6.2 Engine Test on Mercedes-Benz 300D

Another field application device was designed for the second engine test, which was conducted on a Mercedes-Benz 300D. The device has two mesh electrodes separated by 1 cm. Diesel fuel takes around 5 s to pass between the two electrodes for field treatment with strength around 1 kV/mm. Figure 5.21 shows the device mounted on a Mercedes-Benz 300D diesel engine.



Figure 5.21. Field Application Device on Mercedes-Benz 300D. Both laboratory test with dynamometer and road test were conducted with the vehicle and device.

A typical result of a laboratory test of the Mercedes-Benz with a dynamometer is shown in Figure 5.22.

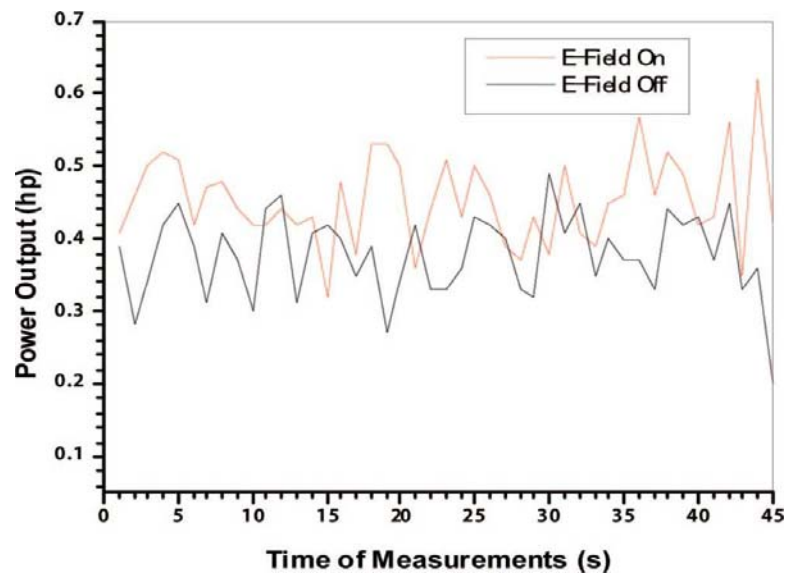


Figure 5.22. Laboratory Test on Mercedes-Benz 300D with Field Application Device. Output powers of the engine with the device on and off were measured by dynamometer. The average power output was originally about 0.368 hp and increased to 0.443 hp after the device was turned on.

The dynamometer measured the engine output at a fixed fuel consumption rate close to 500 g/h. The average power output was 0.3677 hp when the device was off and increased to 0.4428 hp with the device on. This means that the power output was improved by about 20.4% at the same fuel consumption rate. It also indicates that if the engine is on the road under the same condition as our laboratory test, the fuel mileage will be increased by 20.4%.

The laboratory test was repeated for three hours with an error less than 5%. A comparison between the engine test at Cornaglia Iveco and on the Mercedes-Benz sedan confirms that there are optimal values for two parameters, the applied electric field strength and the field application duration. In the test on the Mercedes-Benz, the field strength was 1 kV/mm, and the duration was 5 s. The improvement of engine performance was better than that from the test at Cornaglia Iveco, where the field strength was 1.3 kV/mm and the duration was 1 s. There may still be some room to improve the performance by adjusting these two parameters.

A six-month continuous road test of the vehicle showed that the device increased the fuel mileage significantly. On the highway, the device increased the fuel mileage of the vehicle from 32 miles per gallon (mpg) to 38 mpg. In the city, the improvement of the fuel mileage was not as great as on the highway, but still averaged above 12%.

5.7 Conclusion

As the available crude oil resources become less and less, whereas more and more vehicles come into use, the price of the fuels inevitably becomes higher and higher. On the other hand, more vehicles bring about more air pollution to atmosphere due to the expelled exhaust.

Our technology not only improves the fuel efficiency, but also reduces the hazardous emissions, such as NO_x and other pollutions. Engines using our technology consumes small amount of energy while generates more power output. This significantly improves the fuel efficiency and reduces polluted emissions. Therefore, it has many applications.

We also expect that our technology can be extended to engines using biodiesel and gasoline. The basic physics remains the same. The burning fuel in internal combustion engines releases the heat, expanding the gas and pushing the piston to do the work. The combustion speed and timing is very crucial. If the combustion is slow, some heat released at the time when the piston is near to the bottom-center (BC) crank position will not do the work for the engine; then the combustion cannot be efficient. Therefore, the fuel efficiency of internal combustion engines depends on the combustion speed and timing. With the same engine, even if 100% of the fuel is burned inside the engine chamber, the fast combustion process has much higher fuel efficiency than that of low combustion process. Therefore, with the same engine, injection of small fuel droplets leads to much better performance than that with large fuel droplets.

In summary, our technology is very significant in energy conservation and improves the emission.

REFERENCES CITED

- Aoyagi, Y., Osada, H., Misawa, M., Goto, Y., & Ishii, H., 2006. Advanced diesel combustion using of wide range, high boosted and cooled EGR system by single cylinder engine. *SAE papers*. 2006-01-0077.
- API Gravity* (n.d.). Retrieved June 08, 2009, from http://en.wikipedia.org/wiki/API_gravity.
- Atkins, L. (2009, January). Heavy Crude Oil Outlook. Paper presented at PETROTECH-2009, New Delhi, India.
- Bacon, R. F., & Hamor, W. A. (1916). Refinery Technology. In, *The American Petroleum Industry*. (pp. 447-517). New York: McGRAW-HILL.
- Brake Specific Fuel Consumption* (n.d.). Retrieved July 21, 2009, from http://en.wikipedia.org/wiki/Brake_specific_fuel_consumption.
- Brookfield Engineering Laboratories. (n.d.). Brookfield DV-II+ Pro Programmable Viscometer Operating Instructions. [Brochure]. :Author.
- Brookfield Engineering Laboratories. (n.d.). More Solutions to Sticky Problems. [Brochure]. :Author.
- Collins, C. (2007), Implementing Phytoremediation of Petroleum Hydrocarbons, *Methods in Biotechnology* 23, 99-108.
- Diesel* (n.d.). Retrieved June 11, 2009, from <http://en.wikipedia.org/wiki/Diesel>.
- Einstein, A. (1905). A New Determination of Molecular Dimensions. *Annalen der Physik*, 17(4), 549-560.
- E85* (n.d.). Retrieved June 11, 2009, from <http://en.wikipedia.org/wiki/E85>.
- Ethanol* (n.d.). Retrieved June 11, 2009, from <http://en.wikipedia.org/wiki/Ethanol>.
- Everett, D. H. (1988). Some Important Properties of Colloids. I Kinetic Properties. In, *Basic Principles of Colloid Science* (pp. 76-94). London: The Royal Society of Chemistry.
- Fitch, R. M. (1997). Rheology of Polymer Colloids. In R. H. Ottewill & R. L. Rowell (Eds.), *Polymer Colloids* (pp. 277-313). San Diego, CA: Academic Press.

- Fletcher, J., & Hill, A. (n.d.). *Making the connection - particle size, size distribution and rheology*. Retrieved February 25, 2009, from http://www.chemeurope.com/articles/e/61207/?WT.mc_id=ca0102
- Gasolinel* (n.d.). Retrieved June 11, 2009, from <http://en.wikipedia.org/wiki/Gasoline>.
- Ginder, J. M., & Davis, L. C. (1994). Shear stresses in magnetorheological fluids: Role of magnetic saturation. *Applied Physics Letters*, *65*(26), 3410-3412.
- Graco. (n.d.). *Atomization*. Minneapolis, MN: Author.
- Grant, I. S., & Phillips, W. R. (1975). Electrostatic Calculations. In F. Mandl, R. J. Ellison, & D. J. Sandiford (Eds.), *Electromagnetism* (pp. 83-114). London: John Wiley & Sons.
- Greiner, W. (1998). Simple Dielectrics and the Susceptibility. In *Classical Electrodynamics* (pp. 132-155). New York: Springer.
- Hales, T. C. (1992). The Sphere Packing Problem. *Journal of Computational and Applied Mathematics*, *44*, 41-76.
- Hales, T. C. (1998). The Kepler conjecture. *Mathematics ArXiv*. Retrieved February 22, 2009, from <http://arxiv.org/abs/math.MG/9811078v2>.
- Haw, M. (2005). *Einstein's random walk*. Retrieved March 28, 2009, from <http://physicsworld.com/cws/article/print/21146>.
- Heywood, J. B. (1988). Ideal Models of Engine Cycles. In *Internal Combustion Engine Fundamentals*, (pp. 161-197). New York: McGraw-Hill.
- Hiemenz, P. C. (1986). The Viscosity of Dilute Dispersions. In J. J. Lagowski (Ed.), *Principles of Colloid and Surface Chemistry* (2nd ed.). (pp. 169-222). New York: Marcel Dekker.
- Hiroshi, M., Makoto, K., Yuichi, O., Tetsunori, S., & Shinji, K. (2004, May). The Potential of Lean. Boost Combustion. Paper presented at FISITA World Automotive Congress, Barcelona, Spain.
- Hughes, W. F., & Brington, J. A., (1999). Introduction. In *Fluid Dynamics*. (pp. 1-9). New York: McGraw-Hill.
- Hunter, R. J. (1993). Flow Behaviour. In *Introduction to Modern Colloid Science* (pp. 97-130). New York: Oxford University Press.

- Hyne, N. J. (2001). The Nature of Oil and Gas. In, *Nontechnical Guide to Petroleum Geology, Exploration, Drilling, and Production*. (pp. 1-13). Tulsa, OK: PennWell.
- Jaeger, H. M., & Nagel, S. R. (1992). Physics of Granular States. *Science*, 255, 1523-1531.
- Kelly, A. J. (1999). Electrostatic atomizations Questions and challenges. *Journal of Physics: Conference Series*, 163, 99-107.
- Kelly, A. J.; Avva, R. K. (1998). Electrostatic Atomization Boosts Combustion Efficiency. *AIAA Aerospace America 2*, Reston, VA. pp. 22-23
- Kormann, C., Laun, H. M., & Richter, H. J (1996). MR Fluids with Nano-sized Magnetic Particles. *International Journal of Modern Physics B*. 10 (23-24), 3167-3172.
- Krieger, I. M., & Dougherty, T. J. (1959). A Mechanism for Non-Newtonian Flow in Suspensions of Rigid Spheres. *Transaction of the Society of Rheology*, 3(1), 137-152.
- Landau, L.D. & Lifshitz, E.M. (1959). In, *Fluid mechanics*. New York: Pergamon Press.
- Larson, R. G. (1999). Particulate Suspensions. In, K. E. Gubbins et al. (Eds.), *The Structure and Rheology of Complex Fluids* (pp. 263-323). New York: Oxford University Press.
- Lefebvre, A. H. (1989). Basic Process in Atomization. In, S. Tamburrino & M. Prescott (Eds.), *Atomization and Spray*. (pp. 27-78). New York: Hemisphere Publishing.
- Magnesium Oxide* (n.d.). Retrieved July 14, 2009, from http://en.wikipedia.org/wiki/Magnesium_oxide.
- Masliyah, J. H., & Bhattacharjee S. (2006). Application of Electrostatics. In, *Electrokinetic and Colloid Transport Phenomena*. (pp. 77-104). Hoboken, NJ: John Wiley & Sons.
- Matsumoto, S., & Sherman, P. (1969). The Viscosity of Microemulsions. *Journal of Colloid and Interface Science*, 30(4), 525-536.
- Miller, J. A., Klippenstein, S. J. (2006). Master Equation Methods in Gas Phase Chemical Kinetics. *The Journal of Physical Chemistry A*, 110(36), 10528-10544.
- Mean Free Path* (n.d.). Retrieved February 22, 2009, from http://www.thebestlinks.com/Mean_free_path.html.

- Mooney, M. (1951). The Viscosity of A Concentrated Suspension of Spherical Particles. *Journal of Colloid Science*, 6(2), 162-170.
- Okuda, H., & Kelly, A.J. (1996). Electro- static Atomization – Experiment, Theory and Industrial Applications. *Physics of Plasmas*, 3(5), 2191-2196.
- Parkinson, C., Matsumoto, S., & Sherman, P. (1970). The Influence of Particle-size Distribution on the Apparent Viscosity of Non-newtonian Dispersed Systems. *Journal of Colloid and Interface Science*, 33(1), 150-160.
- Petroleum* (n.d.). Retrieved June 01, 2009, from <http://en.wikipedia.org/wiki/Petroleum>.
- Petroleum Technology Transfer Council. (n.d.). Understanding Paraffin and Asphaltene Problems in Oil and Gas Wells. [Brochure]. :Author.
- Promislow, J. H. E., & Gast, A. P. (1996). Magnetorheological Fluid Structure in a Pulsed Magnetic Field. *Langmuir*, 12(17), 4095-4102.
- Saunders, F. L. (1961). Rheological Properties of Monodisperse Latex Systems I. Concentration Dependence of Relative Viscosity. *Journal of Colloid Science*, 16(1), 13-22.
- Serge, G., & Silberberg, A. (1962). Behavior of macroscopic rigid spheres in Poiseuille flow. Part 2. Experimental results and interpretation, *Journal of Fluid Mechanics* 14 (1962), 136–157.
- Solberg, K. (2006, May). Heavy Oil Challenges: Transport, Blending and Marketing. Paper presented at Offshore Technology Conference, Houston, Texas, USA.
- Song, C., Hsu, C. S., & Mochida, I. (2000). *Chemistry of Diesel Fuels*. Taylor & Francis: New York.
- Speight, James G. (1999). Chemical Composition. In, J. J. McKetta (Ed.), *The Chemistry and Technology of Petroleum*. (pp. 215–216). New York: Marcel Dekker.
- Sweeny, K. H., & Geckler, R. D. (1954). The Rheology of Suspensions. *Journal of Applied Physics*, 25(9), 1135-1144.
- Tao, R. (2001). Super-strong Magnetorheological Fluids. *Journal of Physics: Condensed Matter Physics*, 13, 979-999.
- Tao, R., Huang, K., Tang, H., Bell, D. (2008). Electrorheology Leads to Efficient Combustion. *Energy & Fuels*, 22, 3785-3788.
- Tao, R., & Sun, J. M. (1991). Three-Dimensional Structure of Induced Electrorheological Solid. *Physical Review Letters*, 67(3), 398-401.

- Tao, R., & Xu, X. (2005). Viscosity Reduction in Liquid Suspensions by Electric or Magnetic fields. *International Journal of Modern Physics B*, 19(7/9), 1283-1289.
- Tao, R., & Xu, X. (2006). Reducing the Viscosity of Crude Oil by Pulsed Electric or Magnetic Field. *Energy & Fuels*, 20, 2046-2051.
- Thermal Velocity (2008). Retrieved February 22, 2009, from http://en.wikipedia.org/wiki/Thermal_velocity
- Thomas, D. G. (1965). Transport characteristics of suspension: VIII. A note on the viscosity of Newtonian suspensions of uniform spherical particles. *Journal of Colloid Science*, 20(3), 267-277.
- Vand, V. (1948) Viscosity of Solutions and Suspensions. I. Theory. *Journal of Physical and Colloid Chemistry*, 52, 277-299.
- Wittle, M., & Bullough W. A. (1992). The structure of smart fluids. *Nature*, 358, 373.